Università degli Studi di Pavia
Dottorato di Ricerca in Fisica - xxix Ciclo

Biophysical modelling for cancer ion therapy

Mario Pietro Carante

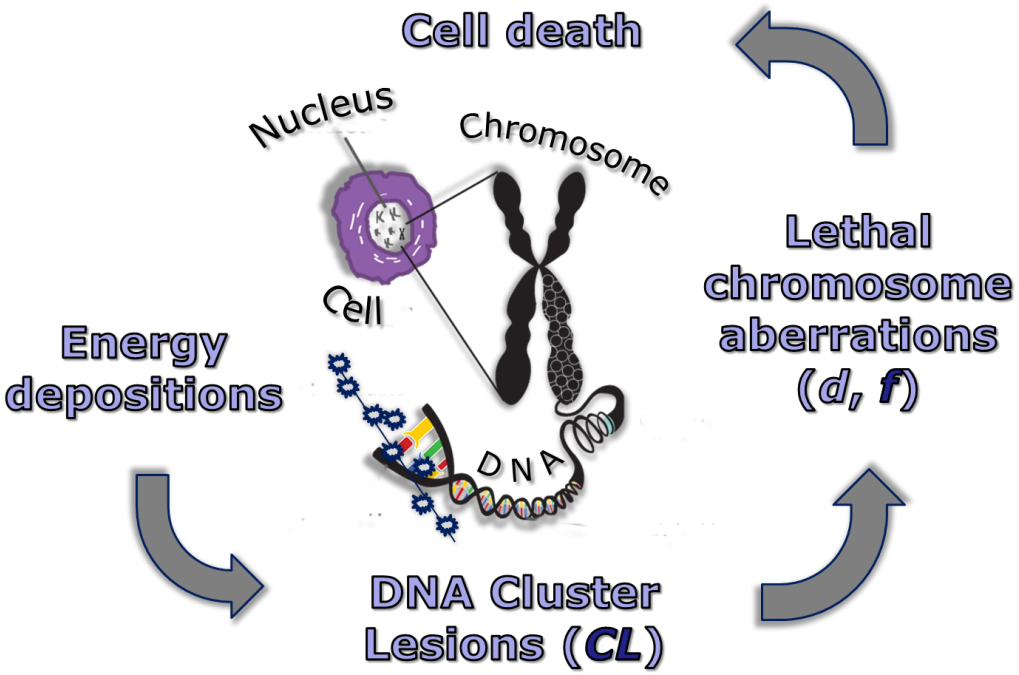

Tesi per il conseguimento del titolo

Full Title:
Biophysical modelling for cancer ion therapy

Mario Pietro Carante

2016

University of Pavia

Department of Physics

Istituto Nazionale di Fisica Nucleare

Dottorato di Ricerca in Fisica - XXIX Ciclo

Biophysical modelling for cancer ion therapy.

dissertation submitted by

Mario Pietro Carante

Submitted to the Graduate School in Physics in partial fulfillment of the requirements for the degree of

DOTTORE DI RICERCA IN FISICA
DOCTOR OF PHILOSOPHY IN PHYSICS

Supervisor: Prof. Francesca Ballarini (University of Pavia)

Referee: Prof. Kevin Prise (Queen's University Belfast)

Referee: Prof. Marco Durante (TIFPA - Trento Institute for Fundamental Physics and Applications)

Cover: Graphical overview of the BIANCA model.

Biophysical modelling for cancer ion therapy.
Mario Pietro Carante
PhD thesis - University of Pavia
Pavia, Italy, November 2016

Contents

We can't all be captains,
we've got to be crew

Introduction

The present thesis work was performed in the framework of the biological effectiveness of ionizing radiation, with particular attention to charged particles in the energy range of interest for tumor therapy. The core of the work, mainly developed within the "ETHICS" INFN project, consisted of the development and application of a biophysical model, implemented as a Monte-Carlo code, for the simulation of cell death and chromosome aberrations directly comparable with *in vitro* experimental data.

Radiobiological experiments are of fundamental importance in this context; however they may not be sufficient in some situations and conditions, for instance where the statistics is low due to technical reasons. The experimental data need therefore to be integrated by theoretical studies and biophysical models, both to reach a better knowledge about the underlying mechanisms and to perform predictions where the experimental information is not available. Moreover this kind of approaches can be of great help in the framework of radiation clinical treatments, in particular hadrontherapy, for which the models can provide predictions on the response of tumor and healty tissues. Indeed a purely experimental approach would require to measure the particle biological effectiveness for a countless number of different irradiation conditions. Furthermore, experimental RBE (Relative Biological Effectiveness) values are generally affected by intrinsic uncertainties, due to the RBE dependence on several factors including not only radiation quality but also dose, dose-rate, cell type and specific endpoint.

Many different models have been developed and are currently used for various purposes, including the LEM approach developed at GSI in Germany and used in various hadrontherapy centers. Some of these models are characterized by a phenomenological approach, whereas others have a more mechanistic nature. Furthermore, many approaches are specific for one particular endpoint, tipically cell death, or one particular particle type.

In this context a biophysical model of cell death and chromosome aberrations, developed at the University of Pavia and the INFN Pavia Section, was refined and further extended within this thesis work. The model, called BIANCA (BIophysical ANalysis of Cell death and chromosome Aberrations),

was developed in order to be suitable for the two aforementioned endpoints and for different ion species, in a wide energy range. Furthermore it is intended to have a mechanistic nature, in order to shed light on some biophysical open questions, but also to be simple enough to be useful in the framework of hadrontherapy, also thanks to the fact that it makes use of only two adjustable parameters and that the computing times are fast.

The model, implemented in the form of a Monte-Carlo simulation code, is based on three main assumptions, linking the initial DNA cluster damage, dependent on both radiation quality and the cell line features, to the production of chromosome aberrations, which in turn can lead to clonogenic cell death. Since the main goal of any tumor therapy is to kill tumor cells while sparing healty tissues, both these endpoints are relevant, considering that the induction of some chromosome aberration types in healty cells may cause cell conversion to malignancy possibly leading to second cancers.

Within this thesis work an already existing model version was first applied to DNA fragmentation, in order to characterize the critical initial DNA damage. A new version, called BIANCA II, was subsequently developed. Following a systematic testing against experimental data taken from the literature, this new version was applied in the framework of hadrontherapy, mainly by evaluating the variation in biological effectiveness along a therapeutic proton beam; an analogous study was then carried out for carbon ions. Applications to cell irradiation with an ion microbeam were also performed. Eventually, a further extension towards a purely predictive model, which does not require parameter adjustments, was developed, deriving a formula to predict ion-induced cell death for a certain cell line starting from the ion-response of a reference cell line and the photon response of the cell line of interest.

In the first Chapter the main physical mechanisms of charged particle interaction with matter (including electronic energy loss and nuclear reactions) will be summarized and some basic concepts like dose, LET and RBE will be recalled. The main aspects of the biological effects of radiation, with particular attention to DNA damage, chromosome aberrations and cell death, will be then illustrated, and some of the main biophysical models available in the literature, especially those relevant for carbon and proton therapy, will be discussed.

Chapter 2 will deal with hadrontherapy, presenting the rationale of this type of treatment, the technical methods of dose delivering to the patient, the main differences between the use of protons and carbon ions and the clinical state of the art, including the number of treated patients and the operating and planned facilities. The integration of biophysical models into treatment planning systems will be then discussed, considering both the case of models currently used in carbon-ion therapy and the possibility of using models for proton therapy. Finally two Italian facilities, CNAO and CATANA, will be briefly described, because some data obtained in these centres were used to test the simulations performed in this work.

In Chapter 3 the results concerning the model development and testing

will be summarized. More specifically, after an introduction on the previous model versions, the BIANCA version will be described, with focus on its basic assumptions and parameters, the target cell modelization and the main steps simulating cell irradiation by different radiation qualities. The testing of BIANCA against dose-response curves, which was partially carried out within this thesis work, will be presented. Afterwards the development of the so-called BIANCA II version, which was entirely performed within this work, will be described, as well as its testing against experimental data for a normal and a radioresistant cell line.

In Chapter 4 the results concerning the model applications will be illustrated, starting from a study aimed to a characterization of the initial critical DNA damage that can lead to the biological endpoints of interest for this work. Afterwards a systematic study on proton effectiveness variation along a therapeutic beam will be described, which allowed characterizing the dependence on depth in tissue, as well as on the biological endpoint, dose level and tissue radiosensitivity. An analogous analysis was also performed for a carbon ion beam. Some other applications will be then presented, namely a study for the evaluation of a microbeam effectiveness and an analysis of the statistical distribution of chromosome aberrations in irradiated cells. Finally, the last important step of this thesis work, concerning the extension towards a purely predictive model, will be discussed.

Chapter 1

Action of charged particles in biological targets

A comprehensive knowledge of both the basic physical interactions of radiation with matter and the biological structures of living tissues is fundamental in order to understand the effects of ionizing radiation on living systems and possibly to prevent the consequent risks for human beings and to exploit the radiation properties in clinical practice. The processes which lead from the initial energy depositions by radiation to the final biological damage is intrinsecally stochastic and can be ideally divided into three main phases: physical, chemical and biological.

The first one, which can last about 10^{-15}s, is strictly dependent on the quality of the incident radiation and mainly consists of excitations and ionizations of the biological target molecules. The chemical stage takes place from 10^{-12} to 10^{-6}s and it is mainly characterized by the production of free radicals, i.e. reactive molecules containing an unpaired electron in the outer shell, which can directly damage the biological structures. The biological phase is finally comprehensive of the initial DNA breaks, the damage at cell level and even the damage at tissue, organ and organism level, and it is thus the more complex stage, whose effects can show up even several months, years or generations after irradiation [1].

In this first Chapter the physical interaction of radiation, in particular of charged particles, with matter will be discussed, as well as the principal biological damage types at cellular and subcellular level. Finally a brief overview of representative models of radiation-induced biological damage (in particular chromosome aberrations and cell death) will be provided.

1.1 Interaction of radiation with matter

Different radiation qualities interact with matter in different ways. This section will be devoted to the description of energy loss by heavy charged particles,

since the behaviour of photons, neutrons and electrons, is somewhat beyond the purposes of the present work. Charged particles can interact with the atoms of a medium mainly through the following processes:

- inelastic collisions with atomic electrons
- elastic scattering from nuclei
- nuclear reactions
- emission of Cherenkov radiation
- Bremsstrahlung

The first three processes are illustrated in figure 1.1 for the case of a proton [2]. For particles like protons and carbon ions, in the energy range for tumor therapy, the loss of energy via Bremsstrahlung and Cherenkov radiation emission is negligible [3]. Moreover, since the masses of the involved nuclei are usually large compared to the mass of the incident particle, elastic interactions with nuclei transfer a small amount of energy compared to atomic electron collisions [4]. The latter is thus the prevalent mechanism of energy loss for these type of particles, and it will be the subject of the following paragraph. On the other hand, elastic scattering from nuclei will not be discussed, while specific attention will be payed to non-elastic nuclear reactions, which are surely less frequent but can have important consequences for living tissues.

1.1.1 Electronic energy loss

Heavy charged particles mainly release energy in matter by exciting or ionizing the atoms of the target material. Since the maximum possible energy transferred in a single collision is small, the deflection of the particle in the collision is negligible, and the path travelled through matter is almost straight [3]. Inelastic collisions are stochastic in nature but, being their number per macroscopic path length generally large, the fluctuations in the total energy loss are small. A useful and meaningful quantity is thus the average energy loss per unit path length, usually called *stopping power* or even *dE/dx*.

A mathematical expression for this quantity was deduced with semiclassical arguments by Bohr [5], but a more accurate formula, taking into account quantum mechanical effects and attributed to Bethe and Bloch [6] [7], is given by

$$-\frac{dE}{dx} = 2\pi N_A r_e^2 m_e c^2 \rho \frac{Z}{A}\frac{z^2}{\beta^2}\left[\ln\left(\frac{2m_e\gamma^2 v^2 W_{max}}{I^2}\right) - 2\beta^2 - \delta - 2\frac{C}{Z}\right] \quad (1.1)$$

where N_A is Avogadro's number, r_e is the classical electron radius, m_e is the mass of an electron, c is the speed of light in vacuum, ρ is the density of the

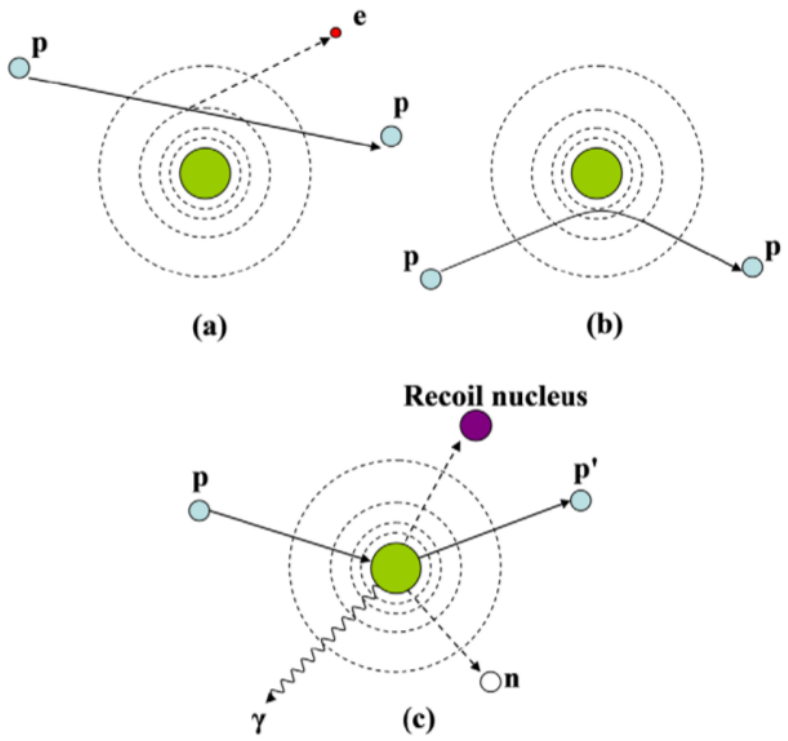

Figure 1.1: Proton interaction mechanisms: (a) inelastic collision with atomic electrons; (b) elastic scattering with nucleus; (c) production of secondary particles via non-elastic nuclear reaction.

absorbing material, Z and A are its atomic number and its atomic weight respectively, z is the charge of the projectile, β represents the ratio v/c where v is the velocity of the projectile, $\gamma = 1/(1\text{-}\beta^2)$, W_{max} is the maximum energy transfer in a single collision, I is the mean excitation potential of the absorbing material, δ is the density effect correction and C is the shell correction. An exaustive description of the various terms and their meaning can be found for example in [4]. For the purposes of this work it is sufficient to outline the dependence of energy loss on the inverse square of the velocity of the incident particle and on the square of the ion charge. On the contrary there is no dependence on the projectile mass. The dependence of energy loss on the energy of the projectile in the range relevant for radiation therapy, as shown in figure 1.2 for several particle types, is of great importance for hadrontherapy, as discussed in Chapter 2.1.1. At non-relativistic energies the stopping power is dominated by the $1/\beta^2$ term and decreases with increasing velocity, until a minimum is reached around $v = 0.96c$. As the energy further increases, dE/dx increases again due to the logarithmic term of Equation 1.1.

It is frequently convenient, expecially in the context of particle therapy, to express the energy loss rate in a way that is independent of the mass density,

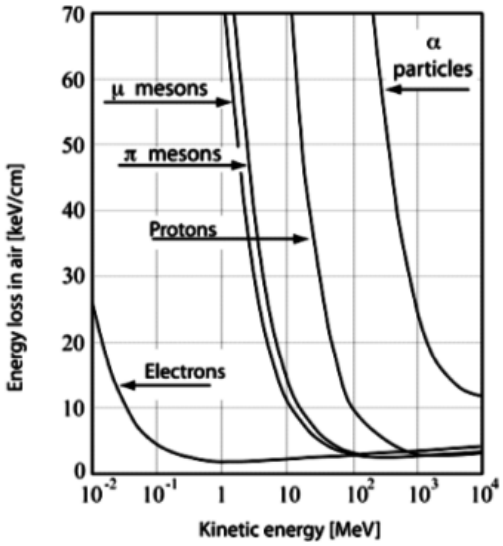

Figure 1.2: Computed energy loss in air vs. kinetic energy for some charged particles [8].

as follows

$$-\frac{dE}{dX} = \frac{1}{\rho}\left(-\frac{dE}{dx}\right) \tag{1.2}$$

This quantity is usually known as *mass stopping power* and it is often expressed in practical units like MeV/(g/cm^2).

Finally, the average distance travelled by a particle in a medium, usually called *range*, can be computed by integrating the inverse of the stopping power over the full energy spectrum of the incident particle, as follows

$$R(T_0) = \int_0^{T_0} \left(\frac{dE}{dx}\right)^{-1} dE \tag{1.3}$$

where T_0 is the initial particle energy. The energy loss however is not continuous, but stochastic in nature. Particles with identical initial energy, therefore, in general will not suffer the same number of collisions and thus will not travel the same distance. This phenomenon is known as *range straggling*. The distribution of the range values about a *mean range* is Gaussian, as shown in figure 1.3.

1.1.2 Nuclear interactions

Protons can also interact with the atomic nuclei via non-elastic nuclear reactions, in which the nuclei are modified in nature and new particles can be produced. The secondary products tend to have much lower energies and much

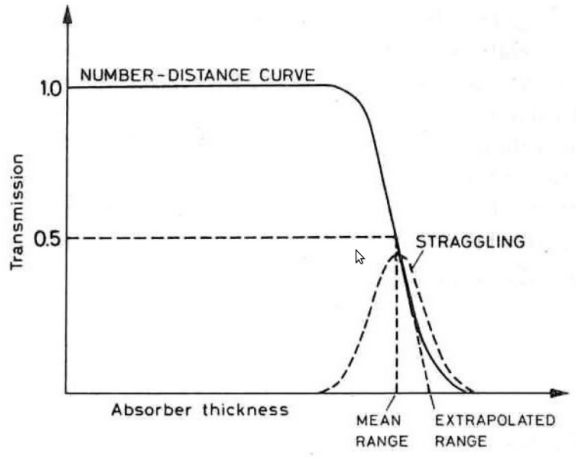

Figure 1.3: Typical range number-distance curve.

larger angles with respect to the primary particle. Although nuclear stopping power is negligible with respect to the electronic one (at least for particles and energies of interest for particle cancer therapy), the consequences of nuclear reactions for biological tissues can be significant.

According to ICRU63 [9], nuclear reactions can be classified as follows

- *elastic* nuclear reactions: the incident projectile scatters off the target nucleus, with the total kinetic energy being conserved (the internal state of the target nucleus and the projectile remain unchanged)

- *nonlastic* nuclear reactions: kinetic energy is not conserved (for instance, the target nucleus may undergo breakup, it may be excited into a higher quantum state, or a particle transfer reaction may occur)

- *inelastic* nuclear reactions: specific type of nonelastic reaction in which the kinetic energy is not conserved, but the final nucleus is the same as the bombarded nucleus.

While for inelastic scattering with atomic electrons the Bethe-Bloch formula 1.1 holds for a wide variety of particles, concerning nuclear reactions it is worth making a distinction according to the quality of the incident radiation. The specific cases of protons and carbon ions, i.e. the two main particles of interest for hadrontherapy, will be briefly discussed.

For proton beams only target fragmentation is possible. Examples of the above mentioned reaction types for protons are

$$p + {}^{16}O \rightarrow p + {}^{16}O \tag{1.4}$$

for elastic nuclear reactions,

$$p + {}^{16}O \rightarrow p + {}^{16}O^{*} \tag{1.5}$$

for inelastic nuclear reactions, and

$$p + {}^{16}O \rightarrow p + p + {}^{15}N \tag{1.6}$$

for nonelastic nuclear reacion [10]. The most probable nuclear interactions of protons at therapeutic energies in biological tissues are those with Oxygen, which can give rise to the production of secondary protons, neutrons, γ rays, alpha particles and recoiling nuclei, which can in turn undergo β or γ decay. The probability of a nuclear interaction obviously depends on the projectile energy and the target nucleus species, but in general secondary protons contribute up to 10% to the total dose deposition (as defined in Section 1.1.3) of a proton beam in water. On the other hand, all other heavier charged particles together contribute less than 0.1% to the total dose [11]. For example, according to a Monte-Carlo simulation reported in [12], the fraction of energy carried away by secondary particles in the interactions of 150 MeV protons with ^{16}O nuclei is distributed as follows

p	d	t	^{3}He	α	recoils	n	photons
0.57	0.016	0.002	0.002	0.029	0.016	0.20	0.16

Most of the final energy is carried away by secondary protons, followed by neutrons and photons. Aroud 64% of the total energy is imparted to charged particles.

In contrast to the proton case, the fragmentation of the primary particle is a fundamental process for carbon ion nuclear reactions. For example ^{12}C can break up into three alpha particles. In general the most frequently produced fragments are H and He nuclei, while the production of heavier fragments, such as B, Be and Li, is less frequent [13] [14]. It is worth mentioning that the produced fragments have the same velocity as the primary ions at the collision [15] [16]. Their range is given by

$$R_{fr} = R_{pr} \frac{Z_{pr}^2}{Z_{fr}^2} \frac{M_{fr}}{M_{pr}} \tag{1.7}$$

where R is the range, Z is the atomic number and M is the mass of the projctile (pr) or of the fragments (fr). The produced fragments, characterized by a lower atomic number, have thus a longer range [17]. The mean range of a particle beam produced by carbon ions is therefore greater than the range of the primary particles. This result has fundamental implications for carbon therapy, as shown in Section 2.1.3.

1.1.3 Dose and LET

Two important concepts in this context are the energy deposited by radiation in a certain volume, and the spatial distribution of the energy deposition events.

In particular the *absorbed dose* is defined as the total absorbed energy per unit target mass, and its unit is the $Gray$, defined as

$$1Gy = 1\frac{J}{kg} \tag{1.8}$$

Usually, the energy lost by a particle beam exceeds the energy absorbed locally by the mass element (or by the patient in a treatment). Ionizing particles in fact may give rise both to electromagnetic radiation and to secondary particles, which can carry a fraction of the transferred energy away from the reference volume. However even the exact knowledge of the absorbed dose might not be sufficient to predict the effects of radiation on tissues. In general, equal doses of different types of radiation do not produce equal biologic effects.

Another quantity, related to the spatial distribution of energy depositions, needs to be introduced: the $Linear\ Energy\ Transfer$ (LET). It is defined for charged particles as the mean energy loss per unit path lenght. It is also possible to refer only to energy loss due to collisions with energy transfer smaller than a threshold Δ, introducing the *restricted* LET

$$L_\Delta = \left(\frac{dE}{dx}\right)_\Delta \tag{1.9}$$

The concept of L_∞, meaning that every energy transfer is included, is often used, and this quantity has the same meaning of the stopping power of Equation 1.1. The unit generally used for LET is $keV/\mu m$ [18]. Some typical values of LET for different radiation qualities (including photons, which are important for radiobiological experiments) are reported in table 1.1.

Radiation	LET (keV/μm)
^{60}Co γ-rays	0.2
250 kV X-rays	2.0
10 MeV protons	4.7
150 MeV protons	0.5
2.5 MeV α-particles	166
2 GeV Fe ions	1000

Table 1.1: Typical Linear Energy Transfer values [19].

It is useful to make a qualitative distinction between the so-called $sparsely$ and $densely$ ionizing radiations. The first type produces an almost uniform spatial distribution of ionizations. On the other side, densely ionizing radiation produces a condensed number of ionizations in a smaller region. X-rays and low-LET particles are sparsely ionizing radiations, while heavy ions and in general high-LET particles are densely ionizing radiations.

A fundamental relationship for the purposes of the present work is the one that connects the two concepts of dose and LET. By defining the fluence Φ as

the number of particles N traversing a unite surface A perpendicular to the propagation direction, it is possible to define the relation

$$D = \frac{N}{A}\frac{dE/dx}{\rho} = \Phi\frac{dE}{dX} \tag{1.10}$$

where we made use of Equation 1.2. By defining the unrestrected LET as the mass stopping power of a particle in water [2] (which is a good approximation for biological systems) and by expressing A in μm^2 and the LET in $keV/\mu m$, it is possible to calculate the dose value in Gy through the following fundamental formula

$$D = 0.16\,\frac{N \times LET}{A} \tag{1.11}$$

where the factor 0.16 derives from the relationship: 1 keV = 0.16 $\times$ 10^{-15} J [10]. This formula will be extensively used in Chapters 3 and 4.

1.1.4 Dose depositions at cellular level

The most important difference between photons and ions concerns the microscopic spatial energy distribution. For photons, the number of ionization events per incident photon in the volume of a cell is small. Many photons are thus required in order to deposit a relevant dose and, since these photons are randomly distributed, ionizations are homogeneously distributed over the entire cell volume. For ions the situation is different. Secondary electrons, originated from Coulomb interactions, are mostly responsible for dose deposition. Most of these electrons receive a small energy transfer or are scattered in the forward direction, leading to a dose deposition concentrated along the core of the primary track, at least for light ions (protons) of therapeutic energies or for heavier ions of small energy (carbon ions around 1 MeV/u). For higher energy heavy ions (e.g. carbon ions of 250 MeV/u), the contribution of fast secondary electrons leaving the track core is no longer negligible and gives rise to a deposition of dose outside the core, which approximately follows a $1/r^2$ dependence on the distance r from the center of the track. Thus, decreasing the LET (or increasing the energy) of the primary particle leads to a more uniform dose distribution, due to the overlap of the *penumbra* contributions of the different tracks [20]. The various situations are illustrated in figure 1.4. The maximum range of the emitted electrons can be parametrized as a function of the ion energy (E, expressed in MeV/u) by the empirical formula [21]

$$r_{max} = \gamma \times E^{\delta} \tag{1.12}$$

where

$$\gamma = 0.062\frac{\mu m}{MeV/u} \qquad \delta = 1.7 \tag{1.13}$$

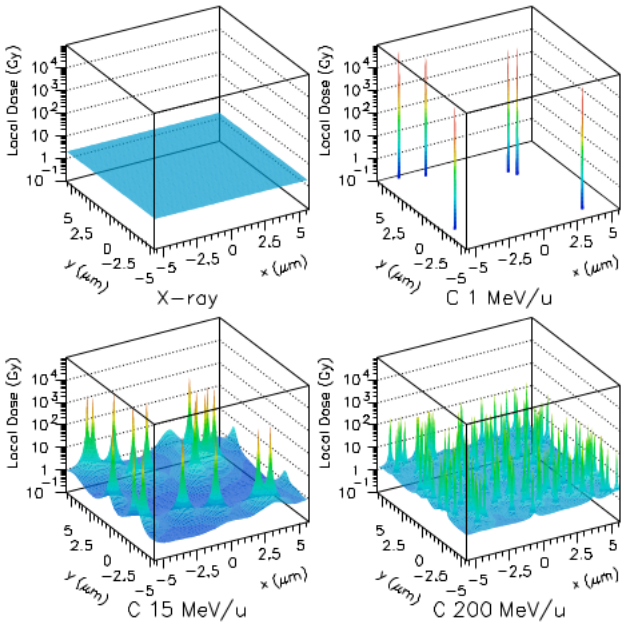

Figure 1.4: Illustration of the different microscopic dose distribution by X-rays and carbon ions with different specific energies. The average macroscopic dose is 2 Gy in all cases [22].

1.2 Biological effects

The knowledge of the *track structure* of the particles, that is the spatial distribution of energy depositions, and in general of the physical processes previously discussed, is necessary in the context of this work but by no means sufficient. We are in fact interested in the biological consequences relevant for radiobiology and for cancer therapy, such as cell death and DNA/chromosome damage. There are several steps connecting the initial energy depositions to these *endpoints*, characterized by complex mechanisms and by different interactions with the biological structures. The process in particular involves the interaction of the primary and secondary particles with the DNA molecule and the damage of chromosomes, with the consequent loss of part of the genetic content and production of chromosome aberrations. The final outcome can be the death of the hit cell, which is the desirable effect in case of tumor cells, or the development of non-lethal damage, which can in turn lead to secondary malignancies if induced in healty cells. The importance of all these processes, which will be analyzed in more detail in the following sections, in thus clear.

1.2.1 DNA damage

Deoxyribonucleic acid (DNA) is a large molecule (polymere) typically organized in a double helical structure. It is composed of many fundamental units,

called nucleotides, each one consisting of a monosaccharide sugar called deoxyribose, a phosphate group and a nitrogen-containing nucleobase (there are four types of bases). The backbones of the double helix strands consist of alternating posphate and sugar groups, bound together by colavent bonds. The two strands are instead bound together by hydrogen bonds between the bases: adenine (A) pairs with thymine (T), while cytosine (C) pairs with guanine (G). The diameter of the molecule, that is the distance between the two strands, is about 2 nm. The distance between two subsequent bases is about 0.34 nm and the helix pitch is about 3.4 nm, since there are 10 basepairs (bp) per turn. The weight of a bp is about 660 daltons (Da, equivalent to 1.67×10^{-24} g). There are 6.349×10^9 bp in a human cell [23], for a total weight of 0.42×10^{13} Da. The DNA macromolecule, which occupies only a few percents (around 2%) of the total nuclear volume, has a complex structure and gives rise to the so-called chromatin fibre, which is organized at many different levels. In particular the DNA is bound to stable proteins (*histones*) to form the *nucleosomes*, consisting of approximately 150 bp making more than one complete turn around a histone and of a portion of 10-90 bp of *linker* DNA, which connect two nucleosome cores [24]. Moreover nucleosomes are "packed" togheter to form a 30 nm diameter chromatin fibre, which structure is not yet known in detail [25].

DNA is commonly identified as the principal target for the biologic effects of radiation, including cell killing, carcinogenesis and mutation. When radiation passes through biologic material, it can interact directly with the DNA molecule, by exciting or ionizing its atoms, or alternatively it may interact with other molecules in the cell (typically water, which constitutes 80% of the cell), giving rise to free radicals that can diffuse far enough to reach and damage the DNA. In the latter case the water molecule is ionized

$$H_2O \rightarrow H_2O^+ + e^- \tag{1.14}$$

and the H_2O^+ ion, with a lifetime of the order of 10^{-10} s, reacts with another water molecule

$$H_2O^+ + H_2O \rightarrow H_3O^+ + {}^{\cdot}OH \tag{1.15}$$

${}^{\cdot}$OH is a highly reactive free radical which, having a lifetime of about 10^{-9} s, can diffuse for a distance of about 4 nm, that is twice the diameter of the double helix, to interact with the DNA. A schematic representation of direct and indirect action of radiation is shown in figure 1.5. The indirect action is dominant for low LET radiation, such as X-rays, while the direct action is dominant for high LET radiation.

Both direct and indirect DNA damages can be classified in several different categories. For example, the bases can be damaged, destroyed or chemically modified. Base damages tend to show a linear increase with dose, they are mainly due to the action of free radicals and they have low probability to evolve to worse cellular damage. More significant are the damages to the strands of

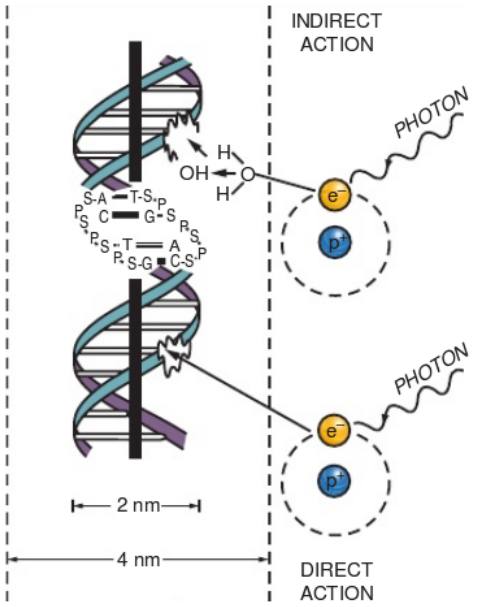

Figure 1.5: Schematic view of direct and indirect action of radiation on DNA.

the double helix. In particular a Single-Strand Break (SSB) occurs when a single bond between a sugar and a phosphate group or between the base and the sugar is broken. SSBs are induced by energy depositions of at least 10-20 eV [26] [27] [28] and their yield is proportional to the absorbed dose in a wide dose range. Their repair mechanism, the Homologous Recombination Repair (HRR) [29], which makes use of the complementary strand as a template for the synthesis of a new chain, is very efficient. This type of damage alone is thus of little biological consequence. Double-Strand Breaks (DSBs), generally defined as two SSBs occurring on opposite strands at a distance smaller than about 10 bps, are on the contrary more difficult to repair, because they can cause the rupture of the double helix. An alternative repair mechanism, called Non-Homologous End Joining (NHEJ) [30], may play a role; this mechanism is error-prone and may cause the recombination of a DNA broken end with a wrong partner. The DSB yield in irradiated cells is about 0.04 times that of SSBs, it is linear with dose, except for high doses [31], and it is about 20-40 DSBs per Gy. Some authors introduced also other DSB categories, such as DSB^{+}, defined as a DSB associated to one or more additional strand breaks on one strand within 10 bp, and the DSB^{++}, involving at least two DSBs in the hit region [32] [33]. A schematic view of this classification is reported in figure 1.6.

A particular classification of Double-Strand Breaks, based on their level of complexity, was proposed by Schipler and Iliakis [25]. "Type 1" DSBs are those generated by *restriction endonuclease* (not by ionizing radiation), which disrupt the continuity of the two DNA strands (breaking the phosphodiester

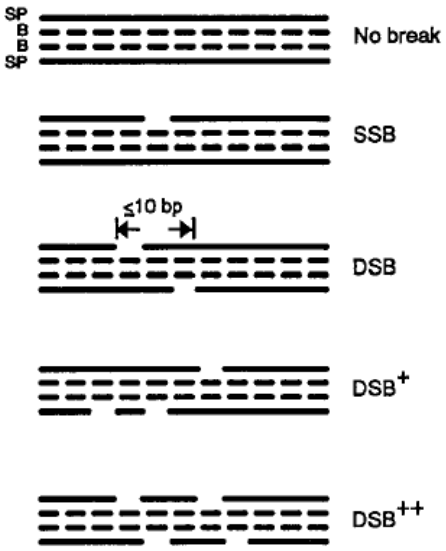

Figure 1.6: Sketch of some different types of DNA damage [32].

bonds) without chemically altering their basic constituents. "Type 2" DSBs are induced by ionizing radiation, mainly through oxidation, and may include sugar and base damages. "Type 3" DSBs involve, in addition to the two typical strand lesions, also other damages, such as base damages, within one or two turns of the DNA helix (10-20 bp). "Type 4" DSBs are indirectly generated DSBs, which are formed through the processing of a base lesion opposite to an unrepaired SSB, or through the parallel processing on both DNA strands of base damage. "Type 5" DSBs are delayed lesions occurring after temperature-dependent chemical processing, including different forms of sugar damage and base damage affecting sugar stability. Finally, "type 6" DSBs are multiple DSBs "in close proximity", in which every single lesion can belong to any of the aforementioned types. This type of damage, which is extremely difficult to repair, can severely undermine local chromatin stability and play a fundamental role in subsequent biological effects at cellular and subcellular level. A representation of the six different levels of DNA damage complexity is shown in figure 1.7. Although the meaning of "close proximity" still needs to be elucidated, indications exist that not only the scale of the previously defined DSB or DSB^{++}, but also a larger scale, may play an important role in this context. For example Monte Carlo simulations performed by Holley and Chatterjee [34], showed an anomalous abundance of DNA fragments at 85 bp and at multiples of 1000 bp, following irradiation with different LET radiations. These two different scales of damage may reflect the organization of chromatine structure: the revolution period of the DNA around the histones (which is in the order of hundred base pairs) and the typical nucleosome packing (which is in the order of kilo-base pair).

Due to the spatial distribution of the events at micoscopic level (as illus-

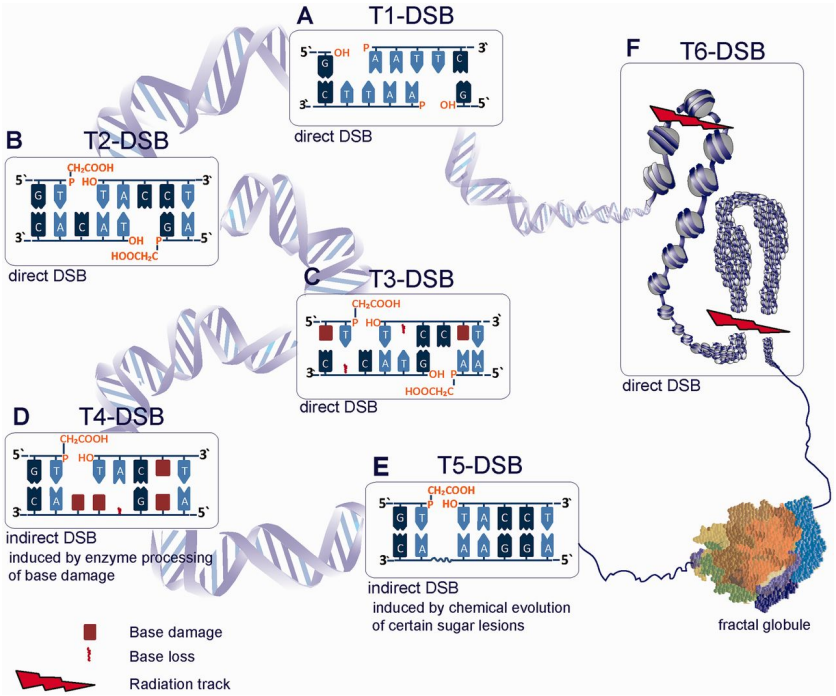

Figure 1.7: Representation of the different DSB types according to Schipler and Iliakis [25].

trated in Section 1.1.4), heavy ions, and in general high LET particles, are more likely to induce clusters of DNA damages, complex and difficult to repair, with respect to X-rays and low-LET radiation. Heavy ions are thus far more effective at inducing biological damage. However, according to both experimental and theoretical results the increase in the number of DNA fragments produced by radiation as a function of LET is highly dependent on the fragment size. In particular, as shown in [35] for the case of Carbon ions in the range 13.8-442 $keV/\mu m$, for fragments of the scale of DSB^{++} the increase with LET is steep (ranging from a few fragments per cell to about 220 fragments per cell), while for fragments in the range 1-9 kbp the increase is much smoother (ranging from less than 10 fragments per cell to about 30 fragments per cell). Finally for fragments in the range 1-5.7 Mbp, the number of fragments per cell is always around 50, with the exception of the last considered LET value, for which there is a reduction in the number of fragments to about 10 per cell. More details can be found in Section 4.1.

1.2.2 Chromosome aberrations

The highest order of organization of the chromatin fibre is that of chromosomes, which consist of one DNA macromolecule organized in the form of chromatin fibre, with a particularly dense region called *centromere*. During most cell cycle chromosomes occupy large regions of the nucleus having linear

dimensions of the order of μm, called chromosome territories. During cell division chromatin becomes more and more condensed, forming a well defined structure called chromatid, composed by two arms and a centromere. During mitosis two sister chromatids are attached to each other at the centromere, giving rise to the typical X-shaped structure of metaphase chromosomes, visible with optical microscopes.

If the DNA double helix is severely damaged by radiation, the chromatin itself can be "cut" and the chromosome can split into two fragments. The broken ends of the two fragments may rejoin togheter, without macroscopical consequences, or alternatively they can fail to rejoin and remain unpaired. As a last possibility, a broken end may join with another end belonging to a different break, giving rise to chromosomes with macroscopic modifications in their original structures. The results of incorrect chromosome fragment rejoining (or un-rejoining) are known as *aberrations* and they can be classified as *chromosome* or *chromatid* aberrations. The first type occurs during early interphase, before the duplication of DNA. A single chromatid is broken and the break is replicated during the S phase. On the other hand, if the damage occurs later in interphase, when the chromosomes consist of two chromatids, and only one chromatid is broken, the outcome is called chromatid aberration. Moreover the various aberrations can be classified as *simple exchanges*, if only two breaks in one or two chromosomes are involved, or *complex exchanges*, if three or more breaks occur in at least two chromosomes [19].

If two breaks occur in two different chromosomes, three possibilities of rejoining are given: *a*) the free ends may correctly rejoin with their original partners; *b*) the two fragments with the centromere may rejoin togheter, producing a *dicentric* (chromosome with two centromeres) and (at least) one acentric fragment, which in general will be lost during metaphase; *c*) each fragment containing a centromere may rejoin with the "incorrect" acentric fragment, producing a *reciprocal translocation*, that is two apparently normal chromosomes with altered genomic content. As a parallel situation, if two breaks occur in the different arms of a single chromosome, the possible outcomes are the following ones: *a*) the free ends may correctly rejoin with the original partners; *b*) the two free-ends of the centric fragment may rejoin togheter, giving rise to a *centric ring* (an *acentric ring* is produced if the original breaks were on the same arm of the chromosome); *c*) each free-end of the centric fragment may join with the incorrect acentric fragment, producing an *inversion*, that is an apparently normal chromosome with altered genomic content. These configurations are illustrated in figure 1.8. Dicentrics and rings are expected to have similar consequences and to play a pivotal role at inducing cell death, while translocations and inversions can be considered as non-lethal aberrations and may take part in the process of carcinogenesis [36] [37] [38]. Another important type of aberration is the so-called *deletion*, that is the loss of an acentric chromosome fragment, due to two breaks on the same arm of a chromosome (interstital deletion) or to a single unrejoined break (terminal deletion). Some

types of complex exchanges were observed to be directly related to cell death [39].

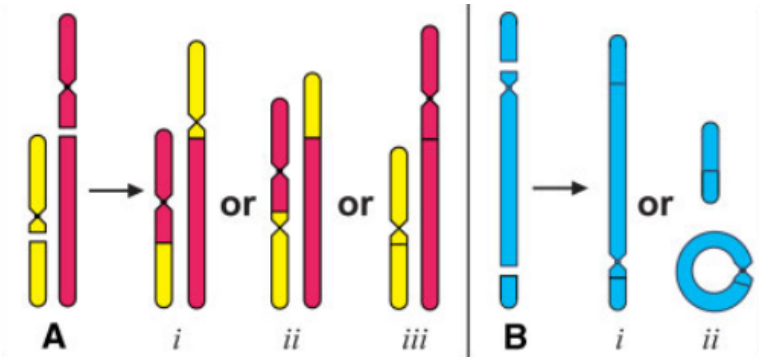

Figure 1.8: Representation of the possible outcomes of two breaks in two different chromosomes (case A), which consist in symmetrical translocations (*i*), dicentrics (*ii*) or correct rejoining (*iii*), and of the possible outcomes of two breaks in one single chromosome (case B), which consist in inversions (*i*) and centric rings (*ii*) [36].

Several *in vitro* experiments proved that the number of aberrations induced in a cell increases with the imparted dose. In particular for low LET radiation, especially X-rays, the yield of dicentrics and rings is approximately a linear-quadratic function of the dose [40] [41] (many experiments were performed in particular for human lymphocytes and fibroblasts). By decreasing the incident radiation energy instead, the quadratic component becomes less and less important and for high LET the aberration yield is basically linear with the dose [42] [19] [43]. The yield of chromosome aberrations against dose is thus in general well described by the formula

$$Y = Y_0 + \alpha D + \beta D^2 \tag{1.16}$$

where Y_0 is the mean number of background aberrations per cell, D is the dose and α and β are two parameters related to the quality of radiation and to the considered cell line.

1.2.3 Cell death

The step leading from the production of chromosome aberrations to the induction of cell death is fundamental for the present work, since radiation-induced cell death is the fundamental *endpoint* for tumour therapy. Here the attention is focused on clonogenic cell death, which is the loss of the capability of proliferation. In the context of radiation therapy the goal is to stop the reproductive power of tumour cells. The first steps for the evaluation of the efficiency of radiation at inducing cell death are *in vitro* experiments, in which a cell colture is irradiated at several dose levels and macroscopical cell colonies

are counted, deducing the fraction of surviving cells by a comparison with a control situation. A detailed description of the procedure can be found in [19].

Several experimental studies [39] [40] [44] showed a close relationship between the mean number of "lethal aberrations" (Y) per cell (usually dicentrics plus centric and acentric rings plus deletions large enough to be visible with the Giemsa technique) and the cell surviving fraction. In particular, for X-irradiated normal human fibroblasts, a one to one correspondence was found between the mean number of lethal aberrations per cell and -lnS, where S is the fraction of surviving cells, as shown in figure 1.9. It is thus possible to write

$$\bar{Y} = -\ln S \tag{1.17}$$

and thus

$$S = e^{-\bar{Y}} \tag{1.18}$$

Moreover, by using Equation 1.16 and by normalizing in order to have no aberrations at zero dose, the following equation can be obtained

$$S = e^{-(\alpha D + \beta D^2)} \tag{1.19}$$

which describes the general dependence of the cell surviving fraction as a function of the absorbed dose. The interpretation of Equation 1.19 and some refinements which lead to a better agreement with experimental data will be discussed in Section 1.3.

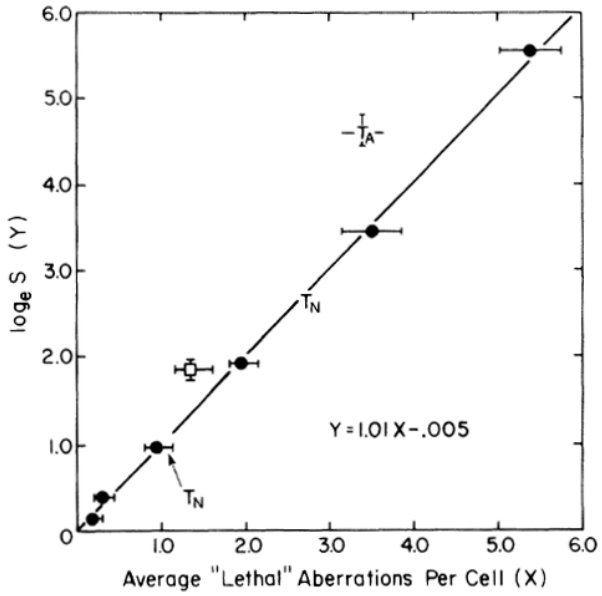

Figure 1.9: Relationship between the average number of "lethal aberrations" per cell and the natural logarithm of the fraction of surviving cells [40].

In a typical experiment the fraction of surviving cells is plotted against the level of absorbed dose in a lin-log scale, as shown in figure 1.10, thus qualitatively obtaining a linear-quadratic curve (at least till doses of a few Gy). In agreement with the discussion on chromosome aberrations, some of which represent the exponent of Equation 1.19, the quadratic term is important for low-LET radiation, like X-rays, but becomes negligible for high-LET (around 100 $keV/\mu m$), for which the curve is basically linear. The shape of survival curves clearly depends not only on the quality of incident radiation but also on the target cell line. By fixing a reference radiation (usually photons), radioresistant cell lines, for which the repair mechanisms are more efficient, are characterized by a higher shoulder, while radiosensitive cell lines are basically linear. A way to quantify the radiosensitivity of a cell line is through the α/β ratio for photons. High ratios (around 9 Gy for AG01522 [45]) and low ratios (around 3 Gy for V79 [46]) are typical of radiosensitive and radioresistant cells, respectively.

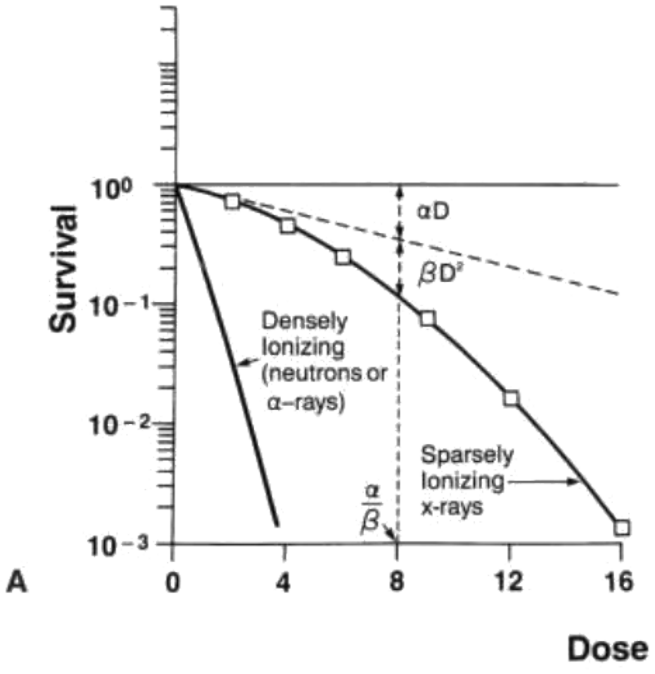

Figure 1.10: Qualitative representation of the survival curve shapes for low and high LET irradiation, and graphical meaning of the α/β ratio [19].

At the end of this brief overview on the biological effects of radiation, it is worth mentioning that the various damages are induced with highly different probabilities. In particular, a cell nucleus irradiatd by 1 Gy of γ-rays is, on average, affected by about 10^5 ionizations (2000 in the DNA), 10^3 SSBs, 40 DSBs, 1 chromosome aberrations and 10^{-5} specific gene mutations, with a probability of cell conversion to malignancy smaller than 10^{-5}.

1.2.4 RBE

In order to quantify the ability of the different types of radiation at inducing damages in biological targets, the so-called Relative Biological Effectiveness (RBE) [47] needs to be introduced. This quantity is defined as the ratio between the dose D_x of a reference radiation (typically X-rays) and the dose D_r of a particular radiation of interest in order to obtain the same biological effect

$$RBE = \left(\frac{D_x}{D_r}\right)_{isoeffect} \tag{1.20}$$

The concept of RBE can be applied to many different types of biological effects. Even with the same incident radiation on the same target, the RBE value may be different if different endpoints are considered. In the case of cell survival experiments, RBE can be referred to different levels of survival (typically, 50% or 10%). As shown in figure 1.11, the RBE is in general higher if the considered survival level is higher. Moreover this quantity also depends on the biological target, since it is higher for cell lines with a higher quadratic component in the photon response, that is for radioresistant cell lines. There are also other "physical" dependencies of RBE, such as on dose (RBE in general decreases with increasing dose), dose-rate and dose fractionation, or "biophysical" dependencies, such as on cell oxygenation.

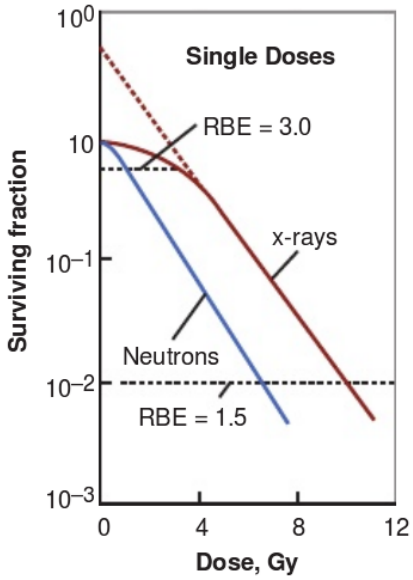

Figure 1.11: Qualitative representation of the concept of RBE for a single dose of neutrons (with X-rays as reference radiation) and its dependence on survival level [19].

For this thesis (see Section 4.1), a special role is played by the RBE dependence on the quality of radiation, in particular on the energy, or equivalently

the LET [48] [49], of the incident particles. As shown in figure 1.12, where RBE data at 10% survival level for cell lines with α/β ratio ranging between 1 and 30 Gy are plotted against LET, the RBE typically increases till LET values around 100 $keV/\mu m$ (where the mean free path between two ionization events is about 2 nm, that is the dimensions of the DNA double helix). The increase is smooth before 10-20 $keV/\mu m$, while it becomes steeper afterwards. Heavier particles reach the maximum at higher LET values (having consequences for the choice of the "best" particles to use in hadrontherapy, as explained in Chapter 2). After the maximum there is a decrease in RBE due to a "waste" of energy by radiation (a phenomenon known as *overkilling*). The RBE dependence on LET also appears as a dependence on depth if the particles are traversing a tissue, like in the case of tumor treatment (see Chapter 2). Even at a fixed LET value however, different particles tend to have a different effectiveness. In particular lighter particles show higher RBE values, since they have smaller energy as well as smaller energy imparted to secondary particles, which will travel shorter paths and will thus have a higher probability of causing cluster damages to DNA.

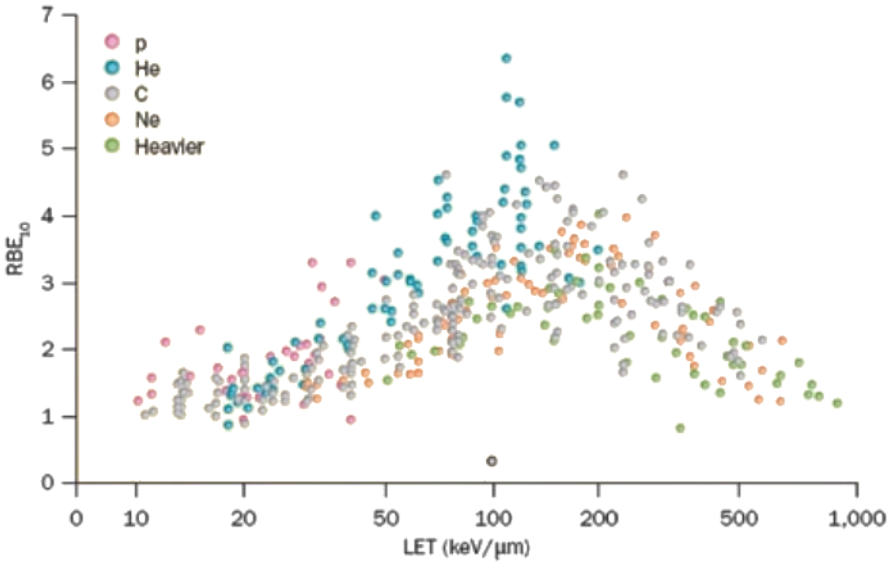

Figure 1.12: RBE vs LET for in vitro experiments on cell lines with α/β ratio in the range 1-30 Gy at 10% survival [50].

A still controversial topic is the role of the variation of proton RBE with LET (and thus with depth in a protontherapy treatment). Proton RBE is generally considered constant in clinical practice, although it can vary depending on particle energy, dose (or cell survival level) and cell or tissue (α/β ratio) type [51]. This topic will be treated in detail in Chapter 2 and the issue will be addressed as part of the original research of this work, as presented in Section 1.1.2.

1.3 Biophysical models

In order to reach a better comprehension of the biophysical mechanisms leading from the initial energy depositions by ionizing radiation to biological damages, a fundamental role is played by biophysical models. These models can have in addition a predictive role, providing important information on the response of cells and tissues in situations in which few experimental data are available. Finally, they are essential in order to take advantage of radiation in clinical practice. In that context, the knowledge of the physics of the irradiation is by no means sufficient, and models predicting the biological effectiveness of radiation need to be included in hadrontherapy treatment plannings, especially for treatments using ions heavier than protons. In this section a brief overview on chromosome aberration models will be presented, followed by a description of the main "historical" models of cell death and of cell death models currently used in hadrontherapy. Eventually particular attention will be paid to cell death models specific for protons.

1.3.1 Chromosome aberration models

One of the first models for the description of chromosome aberration production was proposed by Lea in 1946 [52], with the name of "breakage-and-reunion theory". According to this model, the initial induction of chromosome breaks (producing two free-ends for each break) is followed by pair-wise interaction of independent chromosome free-ends. Such free-ends may undergo *eurejoining* (*i.e.* rejoining with the original partner), *misrejoining* (*i.e.* rejoining with a "wrong" partner) or *unrejoining* (failure of both the previous processes). The second and third processes give rise to exchange-type chromosome aberrations and deletions, respectively. The fate of each single free-end is assumed to be governed by the distance between the various breaks: only free-ends sufficiently close in space and time can interact. According to Lea's model, dose-response curves for exchange-type aberrations can be described by a linear-quadratic relationship (in agreement with the results cited in Section 1.2.2), whereas terminal deletions should increase linearly with dose.

After that, Revel proposed [53], as an alternative, the "exchange hypothesis", based on the idea the all aberrations, including deletions, are exchanges. All linear excess acentric fragments are in fact assumed to derive from incomplete exchanges. As a consequence, even terminal deletions are in this case expected to have a linear-quadratic dependence on dose. However, *ad hoc* experiments [54] showed that only a small fraction of deletions is due to incomplete exchanges.

Some questions however are still open: the first one concerns the characterization of the initial DNA damage that is relevant for aberration production, while the second one is related to the so-called "proximity effect", according to which the probability of interaction for two free ends is a (decreasing?) function of their distance. Concerning the initial DNA damage, only a small fraction

of the initially-induced DSBs (which, on average, are 30-40 per Gy and per cell) leads to aberrations (on average, less than 1 per Gy and per cell). This suggests that there may exist a subclass of clustered and severe DNA damages that are responsible for the formation of chromosome aberrations. Concerning proximity, a consensus has non been reached yet on the relationship linking the initial distance between two breaks and their interaction probability [55]. Some investigators think that a major role is played by DSB proximity (only close DSBs lead to chromosome aberrations), whereas others think that DSB complexity plays a fundamental role (only complex DSBs lead to aberrations).

An example of model based on the proximity assumption is that proposed by Edwards and co-workers [56], which does not discriminate DSBs according to the break complexity and assumes for the DSB rejoining probability P an inverse power law of the form

$$P(d) = \frac{k}{d^n} \tag{1.21}$$

where d is the initial distance between the breaks, and k and n are free parameters to be adjusted *a posteriori* following comparison with experimental data. A good agreement was found with γ-ray experimental data, but the model overestimates dicentric induction by alpha particles. The reason probably relies on the choice of a "fast" decreasing function, which emphasizes the rejoining between close DSBs, which are more frequent in the case of high-LET radiation. A similar incongruence was found with the "Spherical Chromatin Domain"(SCD) model [57], in which a yield of 8.07 DSBs per Gy and per Gbp was assumed, and the breaks were uniformly distributed in the cell nucleus to reproduce the action of sparsely ionizing radiation. After this step, two main assumptions were adopted: 1) only DSBs with distance smaller than a certain "proximity value" can undergo rejoining; 2) the interaction probaility P for two DSBs decreases with increasing their distance d according to the function

$$P(d) = \frac{r}{d}^a \tag{1.22}$$

where r is a constant characteristic of the geometry of the model and a is a free parameter. Because of the steepness of the function, like in the case of Edward's model, the SCD model leads to an overestimation of the yield of centric rings and in general intra-chromosome exchanges, even for photons. This is reported in figure 1.13.

On the other hand, an example of model based on DSB complexity is one of the models developed by Sachs, Brenner and co-workers [58], in which either the initial DSBs are repaired or they become "reactive". The number of reactive DSBs follows a Poisson distribution (the mean value per cell is an adjustable parameter) and the various DSBs are distributed on the 92 chromosome arms wth a probability proportional to their size. The rejoining between chromosome fragments is a completely random process, in which no proximity effect is taken into account. A comparison with *in vitro* data on human lumphocytes

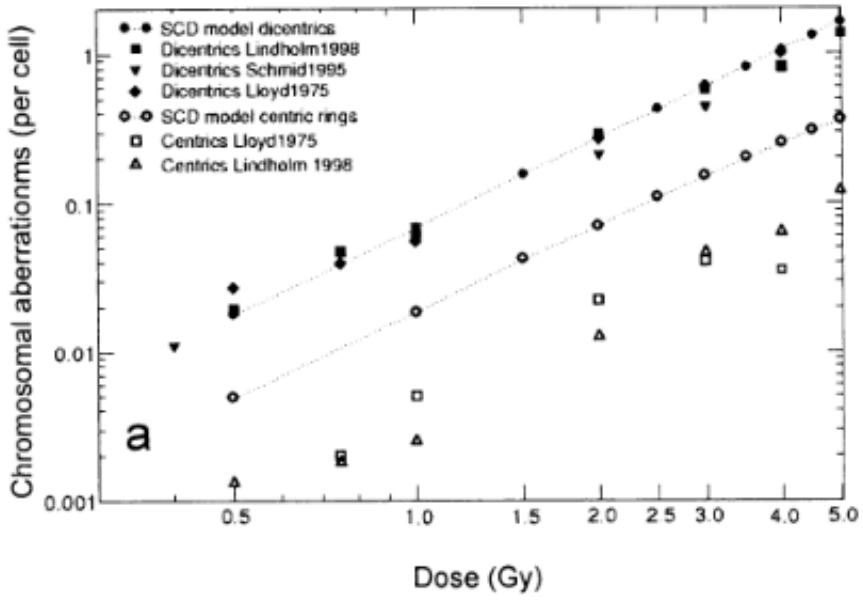

Figure 1.13: Comparison of exprimental data and SCD model predictions for inter-arm and intra-arm chromosome aberration frequencies [57].

irradiated with 1.89 Gy ^{60}Co γ-rays showed a good agreement with dicentrics and translocations, but an overestimation of some types of complex exchanges. This is probably due to the possibility for chromosome free-ends to interact with any other free-end in the nucleus, without any modulation by the initial distance. In subsequent works thus, the same authors took into account both damage complexity and damage proximity [59] [60]. Also the model presented in this thesis adopts this type of approach, giving relevance to the role of both complexity and proximity, as explained in Chapter 3.

1.3.2 Cell death models

Historical approaches

The modelization of cell death RBE as a function of the incident radiation energy, and thus of the depth along the tissues of interest, is of fundamental importance for hadrontherapy treatment planning, especially when using heavy ions. One of the first historical approaches was Lea's "target theory", first developed in 1946 [52] and then refined in 1955 [61]. According to this model, specific for low LET radiation, a cell contains one or more sensitive targets, which can receive one or more radiation "hits"; a hit is an energy deposition event able to induce biological damage. The first version of the theory proposed that just one hit by radiation on a single sensitive target would lead to cell death (STSH, for Single-Target Single-Hit). This version leads to purely negative exponential survival curves (without quadratic term). On the con-

trary the Multi-Target Single-Hit (MTSH) version assumed that one radiation hit on each of n sensitive targets in the cell is required to lead to cell death. By applying Poisson statistics, the probability of having 0 hits on a specific target is given by

$$P_0 = e^{-\frac{D}{D_0}} \tag{1.23}$$

where D_0 is the dose that gives an average of one hit per target and $\frac{D}{D_0}$ is thus the average number of hits per target. The probability of inactivation for 1 specific target is

$$P_1 = 1 - e^{-\frac{D}{D_0}} \tag{1.24}$$

while the probability of inactivation of all targets is

$$P_n = \left(1 - e^{-\frac{D}{D_0}}\right)^n \tag{1.25}$$

The final expression for the surviving probability is thus

$$S = 1 - \left(1 - e^{-\frac{D}{D_0}}\right)^n \tag{1.26}$$

The main limitation of this model is that at zero dose the slope of the dose-survival curve is zero.

The Linear-Quadratic (LQ) model by Chadwick and Leenhouts [62] tried to improve the mechanistic aspects and to provide a biophysical interpretation to the widely used Equation 1.19. The authors identified the critical target with the DNA molecule, and the critical damage with the DSBs. Basically, after assuming Poisson statistics for the distribution of lethal lesions, they attributed the term linear with dose to events in which both DNA strands are broken by the same radiation track; similarly, the term proportional to D^2 was attributed to events in which each strand is broken independently, but close enough in time and space to lead to a DSB. However the hypothesis that the yield of DSBs is proportional to the yield of lethal lesions is not consistent with most experimental data. DSBs indeed tend to increase linearly with dose, whereas lethal lesions present a linear-quadratic behaviour.

Another historical model of cell death is the Theory of Dual Radiation Action (TDRA) proposed by Kellerer and Rossi in 1972 [63], which incorporates the basic microdosimetric concepts. The two main model assumptions are: i) ionizing radiation induces a number of cellular "sublesions" proportional to the absorbed dose; ii) two sublesions induced in a "sensitive site" with linear dimensions of the order of μm can interact and produce a "lesion", which has a certain probability to lead to cell death. By defining the specific energy z as the energy imparted per event and per unit mass, the mean number of lesions after a dose D can be expressed as

$$L(D) = \int L(z) f(z, D) dz \tag{1.27}$$

where $f(z, D)dz$ is the probability that, at fixed dose D, the specific energy is between z and $z + dz$ and $L(z)$ is the average number of lesions within a sensitive site. Moreover $L(z) = kz^2$ (where k is a biological property of the system), since sublesions interact in pairs. Thus

$$L(D) = \int kz^2 f(z, D)dz = k \left\langle z^2 \right\rangle \tag{1.28}$$

Basing on microdosimetric experiments, the term $\langle z^2 \rangle$ was assumed to have a linear-quadratic dependence on dose of the form

$$\left\langle z^2 \right\rangle = \zeta D + D^2 \tag{1.29}$$

By using Equation 1.28, the expression for the average number of lesions becomes

$$L(D) = k \left(\zeta D + D^2\right) \tag{1.30}$$

and consequently the survival probability is given by

$$S(D) = e^{-k\left(\zeta D + D^2\right)} \tag{1.31}$$

If the interplay among *sublesions* is interpreted as the interaction of different DNA breaks to form a complex DNA lesion, this should occur at the *nm* level, in contrast with the hypotesis that *sensitive sites* have linear dimensions of the order of μm. However, if *sublesions* are thought as (severe) DNA damages and *lesions* as the results of their interaction at chromosomal level, *sensitive sites* would have consistent dimensions [64]. This idea will be important for other models, such as the MKM (presented in next session) and the model developed and applied in this work, which will be described in Chapter 3.

LEM and MKM

Two more recent approaches are the Local Effect Model (LEM) and the Microdosimetric Kinetic Model (MKM), currently used for the radiobiological optimization of carbon-ion treatment planning, in Germany and in Japan respectively. LEM was initially proposed by Scholz and Kraft at GSI, Germany, in 1994 [65]. The basic assumption is that the *local* biological effect, that is the damage in a small cellular subvolume, is determined by the expectation value of energy deposition in that subvolume and is independent of the radiation type. Thus, for a fixed biological target, the only difference relies on the different radiation track structures. In the model, particle tracks are assumed to have a radial dose distribution given by

$$D(r) = \begin{cases} \lambda LET_\infty \dfrac{1}{r_{min}^2} & r < r_{min} \\ \lambda LET_\infty \dfrac{1}{r^2} & r_{min} \leq r \leq r_{max} \\ 0 & r > r_{max} \end{cases} \tag{1.32}$$

where λ is a normalization constant and LET_∞ is the unrestricted LET in water. The track core with radius r_{min} represents the region where dose is constant and r_{min}, in the first model version, had a fixed value of 10 nm, taking into account also the diffusion of free radicals. In the third version of the model [66], taking into account the increase of the maximum distance of primary events from the core with the primary particle velocity, an expression of the form

$$r_{min} = \beta \cdot r_c \tag{1.33}$$

was proposed, where β=v/c and r_c is the largest extension of the track core in the limit $v = c$. On the other hand r_{max} represents the maximum radial distance determined by the δ-electrons with the highest energy. It is parametrized following Equation 1.12. Once the dose deposition is known, it is possible to compute the surviving probability for ion irradiation if the response of the same cell line to photons is known. The phenomenological modelization assumed for X-rays survival curves is linear-quadratic, with an exponential tail for doses exceeding a threshold D_t, as follows

$$S_X(D) = \begin{cases} e^{-(\alpha_X D + \beta_X D^2)} & D \leq D_t \\ e^{-(\alpha_X D_t + \beta_X D_t^2 + s_{max}(D - D_t))} & D > D_t \end{cases} \tag{1.34}$$

where s_{max}=α_X+2$\beta_X D_t$ is the slope of the exponential tail. D_t is a semi-free parameter; it is difficult to measure but, from experimental data, it is known to lie between 10 and 40 Gy.

The first step in order to calculate the survival probability for ion irradiation is the poissonian assumption for lethal events (see Chapter 1.2.3), leading to the following surviving probability for X-rays

$$S_X(D) = e^{-N_X(D)} \tag{1.35}$$

where $N_X(D)$ is the average number of lethal events in a cell. Therefore

$$N_X(D) = -\ln S_X(D) \tag{1.36}$$

Since ions and photons are assumed to interact locally with the cell in the same way and the only difference relies in the dose distribution within the cell nucleus, the local effect in each sub-volume of the nucleus can be calculated by

the only knowledge of the dose deposited within it and of the X-ray survival probability for that dose level. The total dose will then be given by the sum of the contributions of all the ion tracks. The average number of lethal events induced per cell by ion irradiation can be obtained by integration of the local density $v(d(x,y,z))$ for the production of lethal events (assumed identical for ions and photons)

$$\overline{N}_{Ion} = \int v(d(x,y,z))dV_{Nucleus} = \int \frac{-\log(S_X(d(x,y,z)))}{V_{Nucleus}} dV_{Nucleus} \quad (1.37)$$

where $S_X(d)$ denotes the X-ray dose-response curve. It is thus sufficient to know $S_X(d)$ and the ion dose distribution in order to calculate the ion surviving fraction through the relationship

$$S_{Ion} = e^{-\overline{N}_{Ion}} \quad (1.38)$$

Simulations over a large number of cells are usually performed in order to obtain a reliable value for S_{Ion}. Finally, in 2010 the approach was generalized by relating the biological response directly to DSB patterns (LEM IV). Cell damage is assumed to depend on the local DSB density, regardless of the primary particle type. Two types of damage are distinguished: isolated DSBs (iDSBs) and clustered DSBs (cDSBs). The latter are formed by at least 2 DSBs occurring in the same *giant DNA loop* (approximatly 2 Mbp). A complexity index can be defined as follows

$$C = \frac{N_{cDSB}}{N_{cDSB} + N_{iDSB}} \quad (1.39)$$

where N denotes the number of a specific damage type. The ion-induced effect is then calculated on the basis of the equivalent photon dose that corresponds to the same complexity index. More details can be found in [67].

The other model currently integrated into treatment planning (in Japan) is the MKM, initially proposed in 1994 by Hawkins [68]. This model is linked to the Theory of Dual Radiation Action (see Section 1.3.2) but assumes that lethal (non-repairable) lesions are due not only to the association of two sub-lethal lesions, but also to some sub-lethal lesions not being repaired after a certain amount of time. The number of lethal lesions of Equation 1.28 will thus have also a linear dependence on the specific energy, leading to the following expression

$$L(z) = A\langle z \rangle + B\left\langle z^2 \right\rangle \quad (1.40)$$

By recalling Equation 1.29 and assuming that the effect of a single track is proportional to dose, the yield of lethal lesions as a function of dose assumes the following functional shape

$$L(D) = (a+b)\,D + cD^2 \quad (1.41)$$

In particular, according to [69], the average number of lethal lesions in the nucleus can be calculated as

$$\langle L \rangle = (\alpha_0 + \beta z_{1D})\, D + \beta D^2 \tag{1.42}$$

where β is assumed to be independent of the radiation type (and thus equal to that for photons), α_0 represents the initial slope of the survival curve in the limit of LET = 0 and z_{1D} denotes the dose mean specific energy by single energy deposition events in a domain. Like in the TDRA model the nucleus, modelled as a cylinder of radius R_n, is composed by n domains of radius r_d. The expression for z_{1D} results to be

$$z_{1D} = \frac{l}{m} y_D = \frac{y_D}{\rho \pi r_d^2} \tag{1.43}$$

where m, ρ and l are the mass, density and mean chord lenght of the domain, respectively, and y_D is the *lineal energy* in the domain, defined as the quotient of energy imparted for a single energy deposition event by the mean chord length of the site. In order to account for the overkilling effect (see section 1.2.4), a saturation correction was introduced, changing Equation 1.42 into

$$\langle L \rangle = (\alpha_0 + \beta z_{1D}^*)\, D + \beta D^2 \tag{1.44}$$

where z_{1D}^* is a saturation correction for the specific energy, depending on a coefficient y_0 which can be calculated by

$$y_0 = \frac{\rho \pi r_d R_n^2}{\sqrt{\beta\,(r_d^2 + R_n^2)}} \tag{1.45}$$

Apart from β, which is detemined by the photon response, the parameters of the model are thus α_0, r_d and R_n. Through comparison with *in vitro* data for Human Salivary Gland (HSG) cells irradiated with ^{3}He-, ^{12}C- and ^{20}Ne-ion beams [70], values of 3.9 μm for R_n, 0.32 μm for r_d and 0.172 Gy^{-1} for α_0 were found thanks to a best fit procedure. Finally, by assuming as usual Poisson statistics, the surviving fraction can be calculated as

$$S = e^{-\langle N \rangle} \tag{1.46}$$

By using this assumption in addition to Equation 1.44 and to the definition of RBE (see Section 1.2.4), the radiobiological RBE can be calculated by the formula

$$RBE = \frac{D_{st}(S)}{\dfrac{-\alpha_{MKM} + \sqrt{\alpha_{MKM}^2 - 4\ln(S)\beta}}{2\beta}} \tag{1.47}$$

The model is integrated into tratment planning, but it is used in connection with experimental data on fast neutron treatments. Radiobiological RBE values are thus rescaled to clinical RBE values. The validity of the procedure was

evaluated by tumor control probability curves for non-small cell lung cancer [71].

Specific approaches for protons

Although RBE variations with LET and thus with depth are generally neglected for protons in clinical practice, as illustrated in Chapter 2, some phenomenological models for the prediction of proton RBE have been developed, especially during the last few years. A first example is represented by the model proposed by Carabe-Fernanez and collaborators [72]. No assumptions about the nature of the interaction between particles and cells are made and the goal is to find a relationship between the α and β parameters for proton irradiation and those for X-rays. Basing on Equation 1.16, the isoeffectiveness of the two radiation types can be expressed as

$$\alpha D + \beta D^2 = \alpha_X D_X + \beta_X D_X^2 \tag{1.48}$$

Dividing this expression by D_x^2 and using the definition of RBE, it is possible to obtain

$$\frac{\alpha}{D_X RBE} + \frac{\beta}{RBE^2} = \frac{\alpha_X}{D_X} + \beta_X \tag{1.49}$$

and consequently

$$(\alpha_X + \beta_X D_X)\, RBE^2 - \alpha RBE - \beta D_X = 0 \tag{1.50}$$

By solving this equation, RBE can be expressed as

$$RBE = \frac{\alpha \pm \sqrt{\alpha^2 + 4\beta D_X\,(\alpha_X + \beta_X D_X)}}{2\,(\alpha_X + \beta_X D_X)} \tag{1.51}$$

Two new quantities, which may be experimentally determined, are then introduced

$$RBE_{max} \equiv \frac{\alpha}{\alpha_X} \tag{1.52}$$

$$RBE_{min} \equiv \sqrt{\frac{\beta}{\beta_X}} \tag{1.53}$$

By using Equation 1.19, these quantities can be easily interpreted as the asymptotic values of RBE at D = 0 and D = ∞, respectively. Dividing both the numerator and the denominator of Expression 1.51 by β_X and using these two definitions, an expression for RBE depending only on X-ray parameters and X-ray dose is obtained:

$$RBE = \frac{\frac{\alpha_X}{\beta_X} RBE_{max} + \sqrt{\left(\frac{\alpha_X}{\beta_X}\right)^2 RBE_{max}^2 + 4D_X \left(\frac{\alpha_X}{\beta_X} + D_X\right) RBE_{min}^2}}{2\left(\frac{\alpha_X}{\beta_X} + D_X\right)} \tag{1.54}$$

Both RBE_{max} and RBE_{min} are assumed to have a linear dependence on dose-average LET (LET_d) and to be inversely proportional to the α/β ratio for X-rays. Thus for a $(\alpha/\beta)_X$ value of 2.686, like that obtained in [73] for V79 cells, the following expressions may be formulated

$$RBE_{max}[LET_d, (\alpha/\beta)_X] = 0.834 + 0.154 \frac{2.686}{(\alpha/\beta)_X} LET_d \tag{1.55}$$

$$RBE_{min}[LET_d, (\alpha/\beta)_X] = 1.09 + 0.006 \frac{2.686}{(\alpha/\beta)_X} LET_d \tag{1.56}$$

where the numerical values were obtained by fitting experimental data. These two expressions can be used in combination with Equation 1.51 in order to have only dependencies on X-ray irradiation parameters. The model still needs to be verified experimentally.

Another example of pheomenological analytical model specific for protons is that proposed by Wedenberg and collaborators in 2013 [74]. The first assumption of the model is that α depends linearly on LET, approaching α_X when the LET decreases

$$\frac{\alpha}{\alpha_X} = 1 + k \cdot LET \tag{1.57}$$

This relationship holds only till LET values around 30 $keV/\mu m$. Concerning the dependence on the cell line, the second assumption is that the slope k is inversely proportional to the α/β ratio of X-rays, as follows

$$\frac{\alpha}{\alpha_X} = 1 + \frac{q}{(\alpha/\beta)_X} \cdot LET \tag{1.58}$$

where q is a free parameter. Finally, β is assumed to be independent of LET, at least in the LET range of interest. Thus

$$\beta = \beta_X \tag{1.59}$$

Again in the framework of the Linear Quadratic model, but dividing Equation 1.48 by D^2 instead of D_X^2, the following expression for RBE can be obtained

$$RBE = \frac{-\alpha_X \pm \sqrt{\alpha_X^2 + 4\beta_X D\,(\alpha + \beta D)}}{2\,(\beta_X D)} \tag{1.60}$$

Thanks to the three main assumptions of the model, the final expression for RBE becomes

$$RBE = \frac{(\alpha/\beta)_X}{2D} + \frac{1}{D}\sqrt{\frac{1}{4}(\alpha/\beta)_X^2 + (qLET + (\alpha/\beta)_X)D + D^2} \qquad (1.61)$$

Through a comparison with experimental RBE data, the best fit for q parameter resulted to be 0.434 $Gy/(keV/\mu m)$. Proton RBE thus depends, according to this model, on dose, LET and tissue type (α/β ratio for X-ray irradiation). The results of this type of models however strongly depend on the assumptions on the parameter dependencies on LET and radiosensitivity, which are based on comparisons with experimental data. For example another approach, presented by McNamara et al. [75], is almost identical to that by Carabe-Fernandez, with the only difference of assuming for RBE_{min} a linear dependence with $\sqrt{(\alpha/\beta)_X}$, instead of the one in Equation 1.56. Therefore a different initial choice of the experimental data set on which establishing the parameter dependences may lead to different results.

In Chapter 3 a model will be presented, which has the aim to deal both with protons and with heavier ions (and with photons as a reference radiation), and to link chromosome aberrations to cell death. The model is sufficiently mechanistic to give information about the main biophysical mechanisms governing radiation damage, but at the same time is also simple enough to provide information on hadron irradiations, and, as a last step, to have a predictive capability.

Chapter 2

Hadrontherapy

Chapter 1 treated the effects of charged particles on biological targets and their modelization. In Chapter 2 the attention will be focused on the use of these particles in tumor therapy. In particular in the first part the basic physical motivations for hadrontherapy will be illustrated, as well as the techniques used to perform a treatment, the advantages and the possible drawbacks of this type of therapy and the clinical state of the art. In the second part the integration of the radiobiological models introduced in Chapter 1 within modern treatment planning will be treated, differentiating the cases of carbon ion therapy and of protontherapy. Finally, specific attention will be given to the description of two italian hadrontherapy centers, the data of which will be used for comparison with the simulation results obtained in this work, as presented in Chapters 3 and 4.

2.1 Why and How

Cancer is one of the leading causes of death worldwide and hadrontherapy, which mainly makes use of protons and carbon ions, may represent a positive evolution with respect to traditional radiotherapy, which is administered to a large portion of cancer patients, often in combination with other therapies. The number of patients treated with charged particles is still small if compared to the total, but the rationale of hadrontherapy is solid as well as the potential improvements with respect to standard treatment, at least in a specific range of cases. This will be the topic of this Section.

2.1.1 Rationale

Radiation treatment, mainly using X-rays, is one of the main treatment options in oncology and is administered to about 50% of the patients with localized malignant tumors [76]. The improvements of this type of treatment during the last decades were mainly addressed to enhance the dose delivered to the

tumour with respect to the dose delivered to the surrounding healty tissues, as in the case of Intensity Modulated Radiation Therapy (IMRT) [77]. The main goal of every tumor treatment consists in fact of maximizing the tumor control probability while sparing normal tissues, thus limiting toxicity and side effects. The idea of using charged particles instead of photons is maily addressed to this aim.

X-rays are absorbed by tissues depositing an esponentially decreasing energy with increasing depth, even if the initial dose buildup, mainly caused by forward scattered Compton electrons, shifts the dose peak a few centimeters away from the surface of the patient's body. Charged particles on the contrary, according to the typical behaviour illustrated in Figure 1.2, deposit most of their energy just before the end of their path. The plot of the released energy (or deposited dose) as a function of depth in tissue shows a peculiar shape, known as Bragg peak, as shown in figure 2.1. The depth of the peak can be modulated by changing the initial beam energy. For instance, for protons, an initial energy of 60 MeV corresponds to a depth of about 3 cm in water, 105 MeV correspond to less then 10 cm and 160 MeV to almost 20 cm. In order to reach the same depth, the initial energy for carbon ions needs to be much higher. For a depth of 25 cm, the energies are around 200 MeV for protons and 4800 MeV for carbon ions. Thus, for a fixed range, carbon ions release on average an energy about 20 times higher than protons.

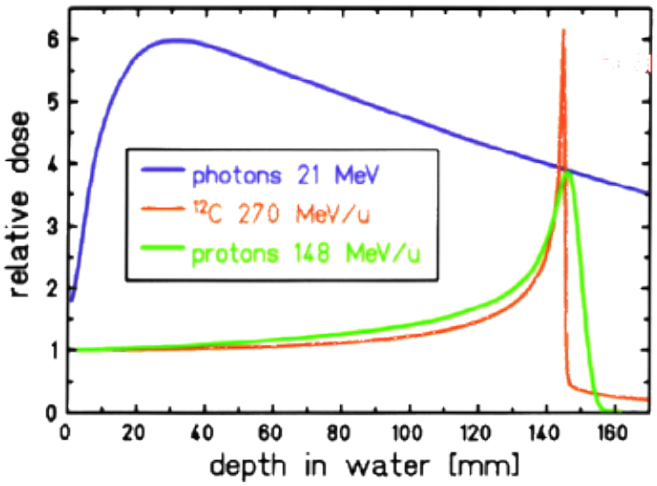

Figure 2.1: Comparison of the depth-dose profile for photons, protons and carbon ions in water [78]

The first proposal of using charged particles for treating (deep) tumors, exploiting the physics of the Bragg peak, was introduced in 1946 by R. Wilson [79]. About 10 years later the first clinical treatments were performed thanks to particle accelerators used in research, while starting from the 1980s the first structures dedicated to protontherapy were planned, the first one being the on-

cological center of Clatterbridge, UK. The use of particles heavier than protons was first proposed in the 1970s in Berkeley by C.A. Tobias [80], who pointed out their advantages: in particular the reduced lateral scattering compared to protons and their higher RBE, especially in the tumor region [76], as shown in the next Sections. The first heavy ions used in clinical trials were Helium and Neon ions, while since the 1990s Carbon ions have been used starting from the Heavy Ion Medial Accelerator in Chiba (HIMAC) in Japan and the GSI in Germany.

2.1.2 SOBP: active and passive scanning

The physical advantage in the use of ion Bragg peak for the treatment of deep tumors is evident. The width of a Bragg peak produced by a monoenergetic ion beam however is clearly too small (tipically few mm) to cover the whole extension of a tumor in most cases. The objective of the treatment is instead to deliver the same amount of dose to every tissue element in the target volume [81], or the right amount of dose to have the same effectiveness. The basic idea is thus to sum up several monoenergetic (pristine) Bragg peaks of different energies at the entrance but with the same beam direction, in order to reach several depths and to obtain a flat biological effectiveness (that is a flat deposited dose if the RBE is constant) as a function of depth, covering the whole extension of the tumor. The depth-dose profile thus obtained is called Spread-Out Bragg Peak (SOBP) and it is shown in figure 2.2 in the case of protons in a homogeneus medium. The total dose D deposited at a fixed depth z is the weighted sum of the various dose contributions d_i of the N pristine Bragg peaks:

$$D(z) = \sum_{i=1}^{N} w_i d_i(z) \tag{2.1}$$

Where w_i are the weighting factors introduced in order to obtain a flat SOBP [82]. It is important to notice from figure 2.2 that the dose level at the entrance is about 20% of that along the SOBP and that the distal fall-off of a typical single peak is still preserved in this configuration. A way to obtain an even higher conformity to the tumor and to increase the ratio between dose to the tumor and dose to normal tissues is to use more than one field direction, as shown in figure 2.3, where a schematic depth-dose profile for two parallel and opposite proton fields is shown. Moreover, since the lateral spread of a beam is small (few mm for protons), the clinical use of particles also requires a spread of the beam in the lateral direction in order to cover a uniform area, both longitudinally and laterally.

After the acceleration of the ions, either by cyclotrons or synchrotrons, the two main methods to obtain a SOBP are inserting materials in the beam path to modify the beam energy (passive scanning), or directly changing the energy from the particle accelerator (active scanning). Concerning passive scanning,

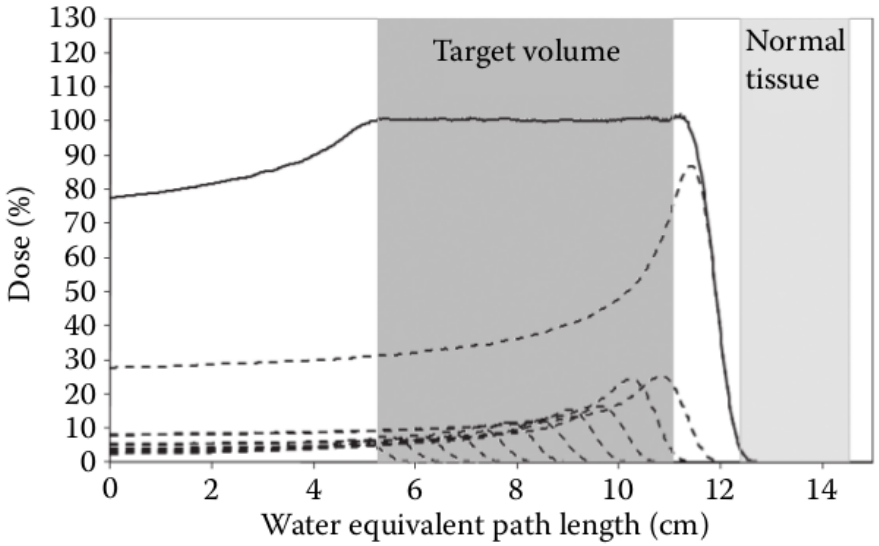

Figure 2.2: Schematic view of a superposition of monoenergetic proton Bragg peaks (dashed lines) giving rise to a typical Spread Out Bragg Peak (solid line) [10]

range modulators are used to spread the pristine peaks into a SOBP, while field-specific apertures are used to conform the beam laterally, and range compensators to conform the beam to the distal end of the target [83]. Range modulators are absorbers of variable thickness. The most used in protontherapy is for example a rotating wheel of variable thickness, positioned between the source and the patient, first proposed by Wilson [79]. Each step of varying thickness of the wheel corresponds to a pristine peak, and the various portions are sequentially irradiated. The thickness of a step determines the range shift of that pristine peak; the angular width of the step determines the weight of the pristine peak. Low-Z materials are preferred as constituents of the wheels to limit scattering [10]. Another example of range modulator is the ridge filter [84]. As regards the lateral enlargement, a scatterer is normally used to widen the beam and a collimator is used to block the beam outside the central high dose region. In figure 2.4 the simplest situation is shown, with a single flat scatterer giving rise to a Gaussian-like profile, and an aperture. However there are many other possible configurations, such as those making use of multiple scatterers or of contoured scatterers, thick in the center and thin on the outside, which mostly scatter the central protons to the outside and create a flat profile. For heavy ions, such as carbon, magnetic deflection systems are also used in order to limit the beam nuclear fragmentation. Finally, concerning conforming techniques, range compensators conform the dose to the distal end of the target, adding more absorbing material in areas where the depth needs to be small and less material where it needs to be large. The depth of the distal end thus varies with lateral position. The main problem of passive techniques

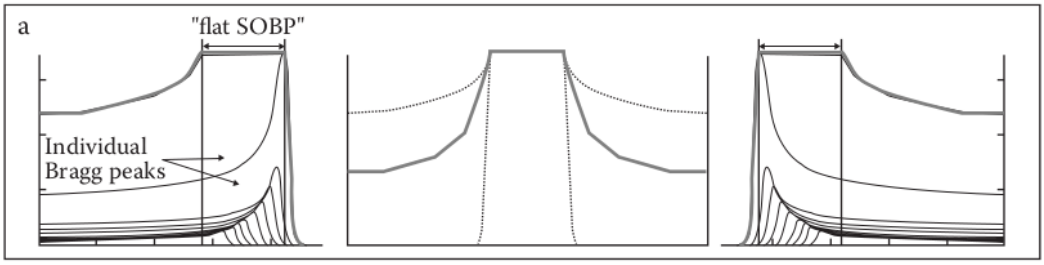

Figure 2.3: Schematic view of the depth-dose profile obtained by the superposition of two SOBPs from parallel opposed beams [10]

is the increased lateral penumbra and the presence of unwanted secondary particles like neutrons due to the presence of scattering systems. Moreover apertures and range compensators need to be shaped *ad hoc* for every patient, according to the tumor shape.

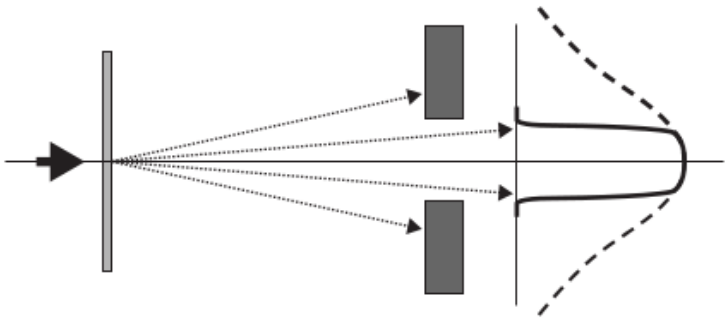

Figure 2.4: Schematic representation of the single-scattering technique using a flat scatterer and an aperture [10]

Active scanning systems allow for a better dose conformity, reducing the integral dose to normal tissues. They consist of the combined use of a synchrotron, which may modulate the initial beam energy, and of a system of magnets perpendicular to the beam axis, which deflect the ion beam. The basic idea is to move along a defined pattern a *pencil beam* (unmodified beam, usually on the order of a few millimeters) to cover the whole target. The target volume is dissected into layers of equal particle range, and thanks to two deflecting magnets [85] the pencil beam is scanned layer-by-layer, starting with the most distal one and then reducing the energy, and thus the range, step by step [17]. The target is divided into many voxels (tipically 30000 per treatment volume), each one receiving a well defined amount of dose. The beam diameter is larger than the voxel dimension, so that it overlaps many positions, yielding a homogeneus dose distribution. Therefore the shape of the target volume can be covered with high precision. The different layers can have high complexity, as shown in figure 2.5, where the different slices

of a carbon ion treatment plan at GSI are reported. In conclusion, for small proton fields, like those for the treatment of eye tumors, passive scanning are still a good solution, mainly because in passive systems the final dose distribution is basically independent from the accelerator performances and from its intensity fluctuations. However, with active scanning it is possible to reach a better conformity compared to passive beam shaping and even to X-ray-IMRT (Intensity-Modulated Radiation Therapy) [17].

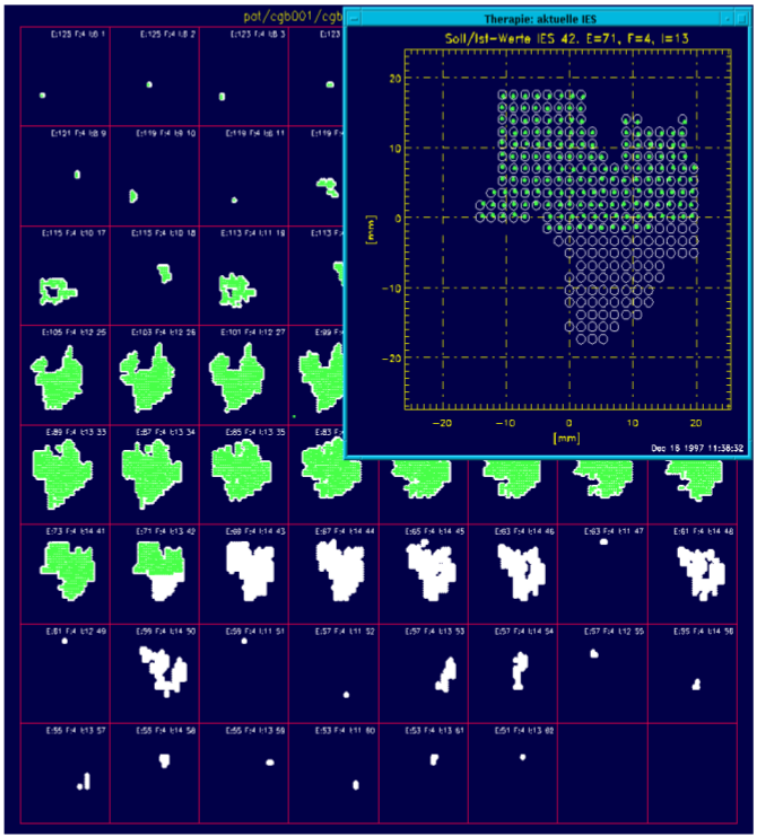

Figure 2.5: Different range slices (one for each panel) of a treatment volume at GSI [86]

2.1.3 Protons and carbon ions

The main advantage of hadrontherapy is the high conformity to the tumor that can be reached with charged particles, thanks to their depth dose profile, culminating with a sharp decrease beyond the Bragg peak, and thus beyond the tumor (especially for protons), and also thanks to the high collimation that ions maintain in their path through tissues. However the most used particles, protons and carbon ions, present some differences and have specifical advantages and drawbacks.

In figure 2.6 the Bragg peak shapes for different ion species are shown [87]. The width of the peak is due to multiple scattering processes, which strongly depend on the atomic number of the projectile. Therefore the resulting range straggling is more pronounced for lighter particles (protons) than for carbon ions. Moreover the lateral scattering, which mainly depends on the Coulomb interaction of the projectiles with the target nuclei and which is decribed in the theory of Molière [88], increases with depth and is more pronounced for protons than for carbon ions, as shown again in figure 2.6. However the possibly higher precision and conformity of carbon ions is reduced by the typical fragmentation tail beyond the Bragg peak, due to nuclear reactions that lead to projectile fragmentation. As discussed in Section 1.1.2 in fact, secondary particles have the same velocity as primary carbon ions and, according to Equations 1.1 and 1.7, on average they travel a longer path, causing a non-negligible dose deposition beyond the tumor. Carbon ions thus are not particularly suitable for monodirectional treatments, especially when organs at risk are present beyond the tumor.

While protons have a similar biological effectiveness compared to photons, except for those in the distal part of the SOBP, carbon ions have a highly non constant depth profile of RBE. In the entrance channel, where the energies are high, they have low RBE values, while in the last 2–3 cm of the range the RBE significantly increases to values between 2 and 5, depending on different factors, including the type of tumour. Moreover very radio-resistant tumours show the largest increase in RBE [89]. This is the main advantage of carbon ions with respect to protons. In particular, it is fundamental to notice that the maximum value of RBE for carbon is in general localized in correspondance of the Bragg peak. In the case of a SOBP, along the *entrance channel* the LET values are lower than 20 $keV/\mu m$ and the RBE is around 1, while only in the last few cm (about 4 in the case of a 26 cm range beam) the LET reaches values around 100 $keV/\mu m$ and the RBE becomes higher and higher in the tumor region. On the contrary, in agreement with figure 1.12, for heavier ions like Neon the RBE is relatively high even at the entrance and its maximum is before the physical peak and thus non optimal. In conclusion, although the effectiveness of other particles, such as ^{4}He and ^{16}O, is currently under investigation [90], the best ions for tumor treatment at the moment are protons and carbon ions. Protons are in general more suitable for tumors next to the so-called organs at risk, while carbon ions are widely used for radioresistant tumors [89], due to their higher effectiveness at the same dose level.

2.1.4 Clinics

As mentioned before, the first treatments with protons and carbon ions date back to the 1950s and the 1990s respectively. The cumulative numbers of treated patients till the end of 2014 were about 120000 for protons and about 16000 for C-ions. More than sixty particle therapy facilities were in clinical operation at July 2016. Only less than ten centers were using C-ions (alone or

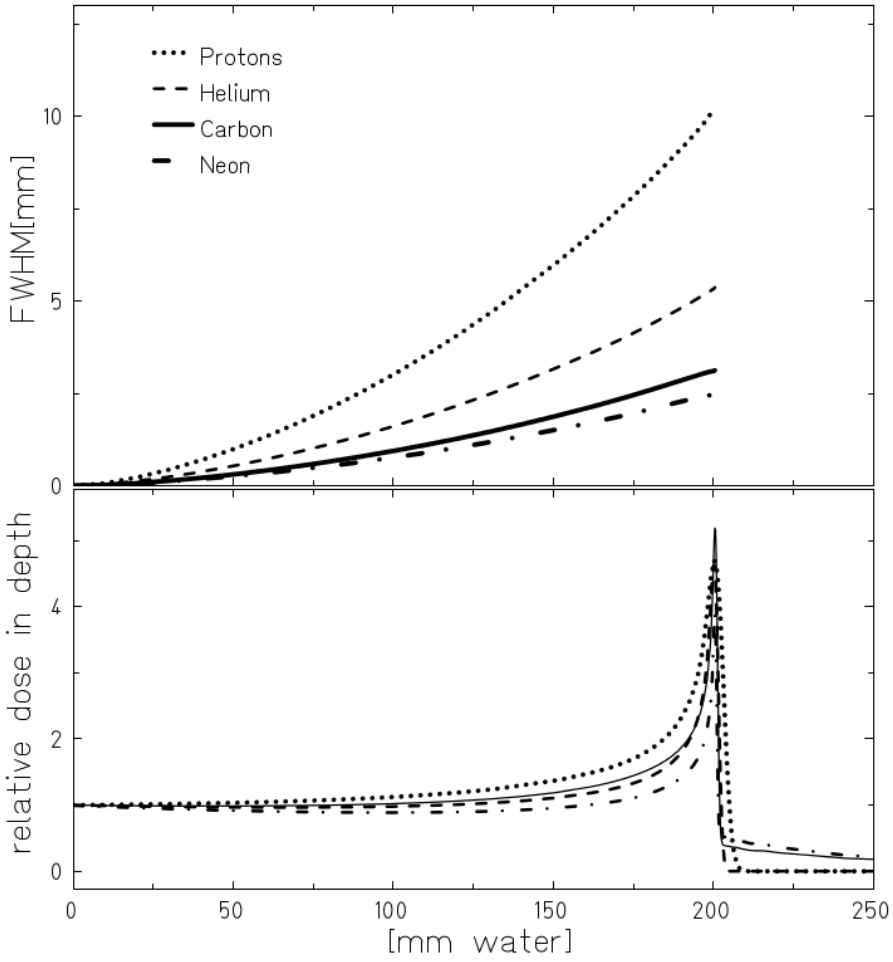

Figure 2.6: Comparison of the lateral scattering for different particles (top) and depth-dose distributions for equal particle range (bottom) [87]

in addition to protons), in Germany, Italy, China and especially in Japan. At July 2016, about 30 particle therapy centers were under construction worldwide, most of which in the United States and in Asia. The increase in the number of facilities in clinical operation and in the number of patients treated is shown in figure 2.7 [91].

The maximum energies available nowadays range between 60 MeV and 250 MeV for protons (with the exception of 1000 MeV in St. Petersburg [92]) and between 320 MeV/u and 800 MeV/u for Carbon ions [93]. The highest energies are necessary for the treatment of deep, solid tumors, while more superficial tumors require lower energies: for example protons of about 60-70 MeV are suitable for the treatment of choroidal melanoma of the eye. Uveal melanomas and tumors at the skull base can be treated with protons, as well as head and neck, liver and lung cancers, and tumors in the vicinity of the spinal cord [76]. Moreover protons are particularly suitable for pediatric patients, since the high

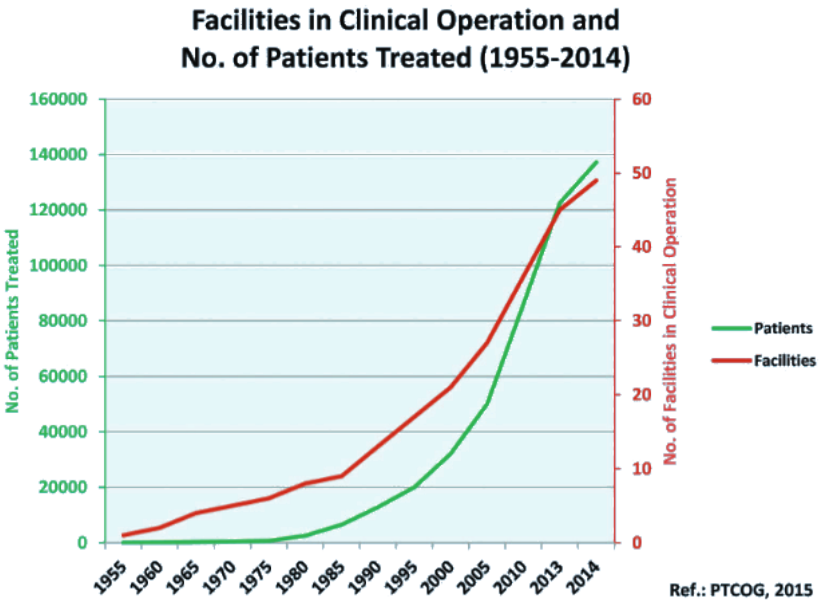

Figure 2.7: Facilities in clinical operation and number of patients treated from 1955 to 2014 [91]

conformity to the tumor allows to reduce the toxicity in the highly sensitive healty tissues. On the other hand, carbon ions are particularly suitable for tumors unresponsive to conventional radiotherapy, such as chordomas, chondrosarcomas and osteosarcomas. A case of particular interest for the present work is that of eye tumors treated with protons, for which the eye preservation rate is generally over 90 percent at 5 years [94]. In general, about 10% of the X-ray patients would profit from a proton treatment, while a few percent of the X-ray patients would profit from carbon ion therapy [89].

Another issue, which will be addressed in Chapter 4, is the tendency to reduce the number of fractions and increase the dose per fraction, that is hypofractionation [95]. For a "standard" treatment 2 Gy are tipically delivered to the patient in about 20-30 fractions while, especially for C-ions, less than 10 fractions may be used (the limit of a single fraction was reached at NIRS in Japan). This represents a great advantage for the patient but also for the cost of the treatment. Moreover, while for conventional therapy fractionation is a way to obtain tumor re-oxygenation and thus to contrast hypoxia, the lower Oxygen Enhancement Ratio (OER, i.e. the ratio of doses administered under hypoxic to aerated conditions needed to achieve the same biological effect), typical of high LET radiation, allows hypofractionation for ion therapy without serious disadvantages due to tumor hypoxia. An important issue that will be investigated in Chapter 4 (especially for protons) is the dependence of RBE on the dose level, and thus on the number of fractions per treatment.

2.2 Integration of radiobiological models within treatment planning

Beam delivery and dose distribution into the patient are established through a process called treatment planning, which has the aim of "balancing" high dose conformation to the target while sparing healthy tissues. Thanks to imaging techniques the Clinical Target Volume (CTV) and Organs At Risk (OAR) are delineated, and in a second moment the maximum doses to the tumor and to healty tissues are established. Moreover a Planning Treatment Volume (PTV) is defined in order to take into account any geometrical variation during the therapy and all possible physical uncertainties. Then the beam directions are selected and the dose optimization is performed. The absorbed dose is calculated by the Treatment Planning System (TPS) on the basis of CT data, which provide the X-ray absorption coefficient at each location in the patient. The total dose is then calculated as a superposition of several Bragg Peaks [96]. Thus the main requirements for a ion treatment planning are [97]:

- a physical beam model to describe the ion interaction with tissues, depending of the primary radiation quality
- algorithms to derive the particle energies and fluences from a prescribed dose distribution (process known as *inverse planning*)
- algorithms to translate the CT information into a water-equivalent path length, relevant for heavy ions

However the purpose is not just to deliver a high dose in the tumor and a low dose in healty tissues (and thus to produce a constant dose level along the SOBP) but more generally to have a conformity regarding the biological effectiveness, which is quantified by the product of physical Dose and RBE, which is measured in GyE. The integration of an RBE model into treatment planning, especially for heavy ions, is therefore essential. This topic will be the subject of the present Section.

2.2.1 Carbon ion therapy: LEM and MKM

In order to deliver a uniform biological dose to the target volume, and minimizing the dose received by healty tissues, RBE variations with LET (that is with depth), dose and tissue type need to be taken into account, at least for Carbon ions. Moreover the RBE strongly depends on the type of irradiated tissue, as well as on the biological endpoint and on the ion beam characteristics. RBE distributions are thus expected to be tissue and patient plan specific [98]. A Treatment Planning System (in the case of clinical applications) or a radiation transport code like FLUKA, PHITS or GEANT4 (maily in the context of reasearch or plan validation), providing the dose distribution in the patient,

needs therefore to be coupled with a biophysical model, like those presented in Section 1.3. For C-ions the two main models currently implemented in clinical treatment plannings are LEM and MKM.

Concerning LEM, it has been coupled with the first treatment planning system used at GSI, called TRiP98 [99] (the results are also used for the new TPS Syngo), and also with the FLUKA Monte Carlo code [98]. The basic idea is to provide, according to LEM calculations and predictions, a RBE table containing all relevant data to calculate the biological effective dose for a certain tissue type, as a function of energy and particle species, even for mixed radiation fields. First of all the α and β parameters as a funtion of energy and particle type are derived, and then dose-averaged on the different radiation types hitting a certain material (tissue). This is the input for the TPS or radiation transport code. The main LEM parameters necessary for the calculations are: the cell nucleus dimensions, the mean number of X-ray-induced DSB per cell per unit dose, the size of a DNA giant loop (for version LEM IV) and the number of base pairs (around 15) within which two SSBs are counted as an additional DSB. Finally, according to Equation 1.38, the surviving level is computed, as well as the RBE.

For the case of LEM IV coupled with the TRiP98 treatment planning system, a prediction for a realistic two-port irradiation plan is illustrated in figure 2.8. The considered cells are hamster ovary cells, irradiated with both protons and Carbon ions. The depth-dose profile (panel *a*) of carbon ions shows a typical convex shape in the target region, because the irradiation was optimized to achieve a homogeneous biological effect. The dose required for Carbon ions in the target region is much lower than that for protons. However the cell survival level (panel *b*) is significantly higher for the latter, due to the higher LET (and consequently RBE) of C-ions. On the contrary in the entrance channel, where LET and RBE are small for both ion species, almost identical effects are observed. It can be noticed that the predictions of the biophysical model are consistent with the experimental data. Finally the RBE profiles for protons and Carbon ions are shown in panel *c*. In the middle of the target region it reaches values of almost 2 for C-ions, while for protons it is only slightly increased with respect to the value close to 1 shown in the entrance channel.

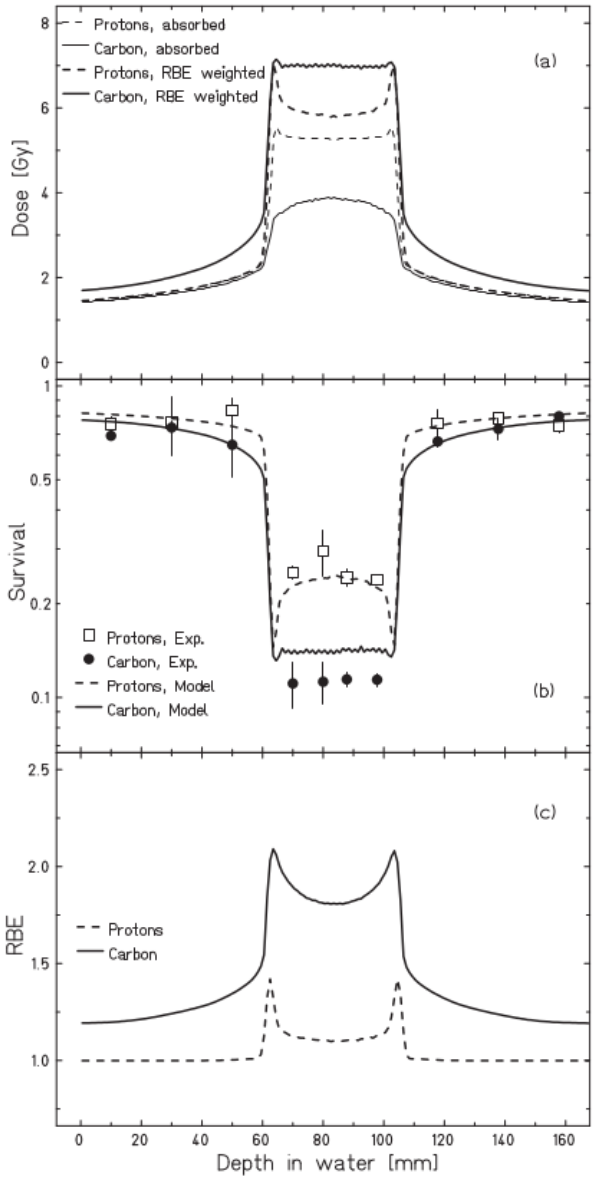

Figure 2.8: Experimental data and model predictions for a two-port irradiation of hamster ovary cells with protons and carbon ions: (a) physical depth-dose distribution and RBE weighted dose; (b) measured (symbols) and calculated (lines) cell survival level; (c) Calculated RBE values [67]

Concerning another important biophysical model used in clinical practice, that is the MKM, it was fully integrated into the research version of the treatment planning system [100] [101] by using the 290 MeV/u carbon beam to irradiate aerobic Human Salivary Gland (HSG) cells. In this case, in addition to the physical and biological dose (as defined previously), the so-called clinical dose is also calculated, since radiobiological RBE values are rescaled to clinical RBE values on the basis of data on fast neutron treatments, as reported in

section 1.3.2. Figure 2.9 (panel *a*) illustrates the physical, biological and clinical dose distributions along the central beam axis in a single-field irradiation, in which the prescribed clinical dose was set to 5.79 GyE within the target volume, corresponding to 3.99 GyE in biological dose. Apart from the difference in the number of fields used for irradiation, the situation is similar to that depicted in Figure 2.8 and the considerations are similar. The predicted and experimental cell survival fraction as a function of depth is shown in figure 2.9 (panel *b*). The shape is flat along the SOBP, although with a value of 13.4%, slightly higher than the planned clinical one of 10%. The characteristic fragmentation tail of carbon ions beyond the target volume is visible, unlike the case of a two-port irradiation.

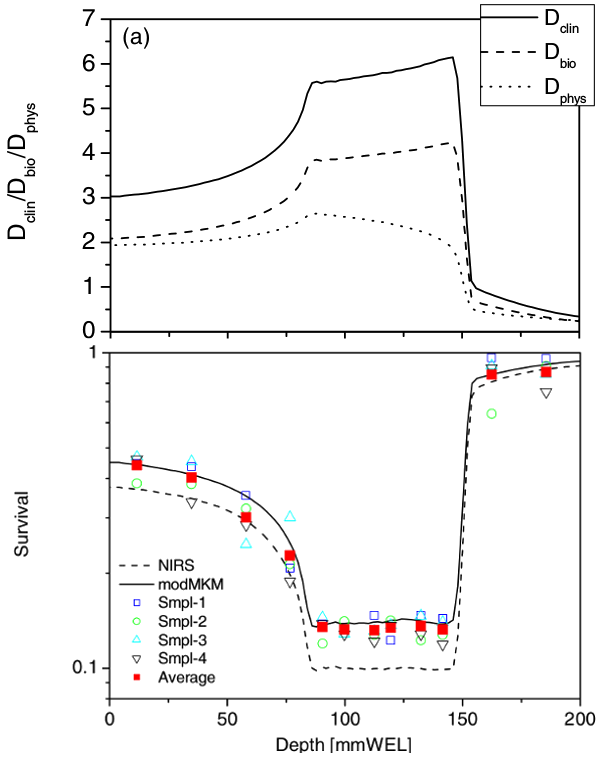

Figure 2.9: (a) Clinical, biological and physical dose distributions along the central beam axis of a single-field carbon ion irradiation; (b) Measured survival values (symbols) compared with the planned survival curve (dashed curve) based on the NIRS radio-biological model and the recalculated survival curve (solid curve) based on the modified MKM [101]

2.2.2 Protontherapy

Unlike the case of carbon ion therapy, for protontherapy no biophysical model is currently implemented into any treatment planning system worldwide. In

clinical practice in fact proton RBE is considered constant and equal to 1.1 along the whole SOBP for every tumor type. There are however many experimental evidences, basing on both *in vitro* and *in vivo* irradiations, that this is only an approximation, since proton RBE depends on several factors, such as the considered dose level [102] and the irradiated tissue type or cell line [51]. Moreover many experimental data show that proton RBE is not constant with depth along a SOBP, but it is characterized by a significative increase in the distal region, due to an excess of low energy (and higher LET) protons [103] [104] [45]. Nevertheless the currently available results are affected by uncertainties, and it is fundamental to integrate the experimental data with theoretical approaches, in order to have information in a wide range of conditions and values of dose, LET and radiosensitivity.

Even if they are not currently integrated into treatment planning systems, there are several models investigating RBE deviations from the 1.1 value used in clinics. All the phenomenological models presented in Section 1.3.2, that is the Carabe-Fernandes, Wedenberg and McNamara models, predict a clear, almost linear, increase of RBE as a function of dose-average LET. In figure 2.10 the specific case of a $(\alpha/\beta)_X$ ratio of the irradiated cells equal to 1.22 is shown for a 2 Gy dose level. Experimental data from [105] are reported togheter with the predictions of the three models. Ranging from less than 1 $keV/\mu m$ to about 20 $keV/\mu m$, the increase in RBE is larger in the case of experimental data, but it is still high (around 2 times) compared to 1.1, for model predictions. All models predict a steeper slope with decreasing $(\alpha/\beta)_X$. The predicted dependence of RBE on LET is almost linear, especially for large $(\alpha/\beta)_X$ ratios, while the experimental data seem to describe a steeper increase at the highest considered LET values.

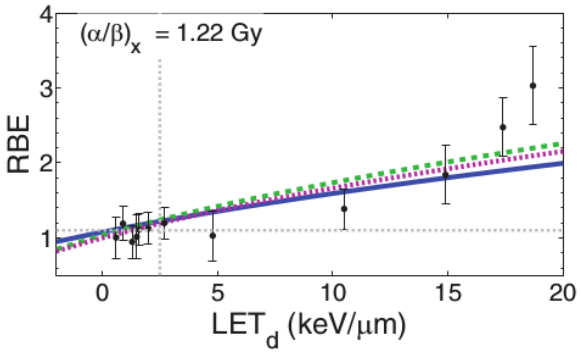

Figure 2.10: RBE for cell survival as a function of LET a $(\alpha/\beta)_X$ value of 1.22 Gy and a dose of 2 Gy. Three different models predict the RBE: McNamara et al model (blue solid line), Carabe et al model (green dashed line) and Wedenberg et al model (pink dotted line). Experimental data from [105] are also included [75]

From the analysis performed in [75] it is also clear that the RBE decreases

with increasing $(\alpha/\beta)_X$ for all three models. The decrease in RBE with increasing $(\alpha/\beta)_X$ is more significant at low $(\alpha/\beta)_X$ values, especially at higher LET values. Finally for a fixed LET value of 2.5 $keV/\mu m$, the RBE decreases with increasing dose at low $(\alpha/\beta)_X$ (1-2 Gy), in agreement with all three models. For high $(\alpha/\beta)_X$ (10-15 Gy), the Carabe model predicts an increase in RBE with increasing dose, the Wedenberg model predicts a slight decrease and the McNamara model shows a rough invariance.

Concerning the prediction of RBE variations with depth along a SOBP, figure 2.11 shows the shape of the biological dose according to these three phnomenological models, togheter with the physical and clinical dose (i.e. physical dose rescaled for the constant value of 1.1). The simulated SOBP had a modulation width of 10 cm and range of 25 cm. The dose-average LET in the middle of the plateau region of the SOBP (depth: ∼160–220 cm) ranges from 1.4 to 3.1 $keV/\mu m$, and from ∼1.4 to ∼10 $keV/\mu m$ over the entire plateau region. The cases of both a radioresistant ($(\alpha/\beta)_X = 1$ Gy) and a radiosensitive $(\alpha/\beta)_X = 10$ Gy) tissue are shown. Each of the considered RBE models, with only slight differences, predicts an increase in biological dose at the distal edge of the SOBP. It is important to notice that, for the case of low $(\alpha/\beta)_X$ ratio, this increase is of about 30% compared to the dose used in clinics, that is a much higher value than for the case of high $(\alpha/\beta)_X$ (about 4%). As a final consideration, a study performed in 2016 [106] showed that, at least in the case of a SOBP with a range of 25 cm and for a tissue with $(\alpha/\beta)_X = 2$ Gy, the biological dose predicted by LEM IV is even higher than that predicted by the Carabe-Fernandes and Wedenberg models.

2.3 Two Italian facilities

As a conclusion for Chapter 2, two Italian hadrontherapy facilities will be briefly presented, with their dosimetric and radiobiological characterizations:

- CNAO (Centro Nazionale di Adroterapia Oncologica, Pavia, Italy), since in this work some data on cell survival by carbon ions at therapeutic energies were used
- CATANA (Centro di AdroTerapia e Applicazioni Nucleari Avanzate, at INFN-LNS in Catania, Italy), since we exploited a proton depth-dose profile used in that center for ocular melanoma treatment and some data on human fibroblast survival, as illustrated in Chapter 4.

Experimental data obtained in these centers were used for model testing in this work. It is also worth mentioning that in Italy another facility, located in Trento, has recently started operating; more than 150 patients (including about 20 paediatric patients) have been treated with protons, mainly for tumors in the following regions: brain, head and neck, spine-skull base or pelvis-sacrum.

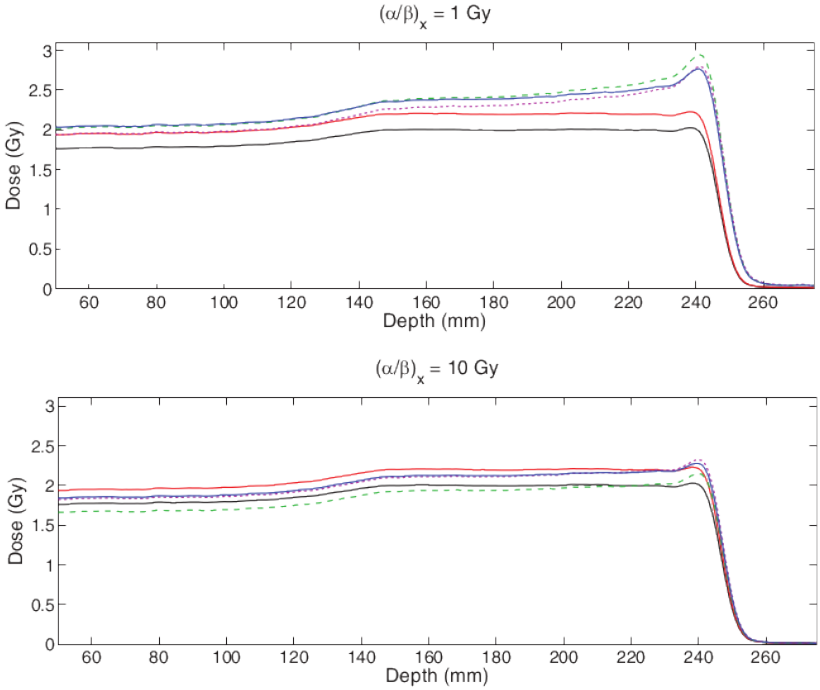

Figure 2.11: Predicted biological doses for Carabe model (green dashed curve), Wedenberg model (pink dotted curve) and McNamara model (blue solid curve) for a simulated SOBP with a modulation width of 10 cm and a range of 25 cm. The physical dose is shown by the black solid curve while the red curve shows the physical dose scaled by a constant value of 1.1 [75]

2.3.1 CNAO

CNAO is one of the four hadrontherapy centers in the world providing both protons and carbon ions [107]. The first idea for the project of this facility dates back to 1991 [108]. The evolution of the center can be divided into three main periods: 1) realization phase, from 2001 to 2010, when design, construction and commissioning were performed; 2) clinical trial phase, from 2010 to 2013, ranging from tests to patient treatments; 3) running phase, from January 2014 when the clinical activity started. Till 2015 about 300 patients were treated, most of them with carbon ions. The main treated tumors are chordomas and chondrosarcomas of the spine and of the skull base, meningiomas, salivary gland tumors, bone and soft-tissue sarcomas, several types of recurrent tumors, prostate and pancreatic cancers and orbital tumors.

Concerning CNAO accelerators and beam lines, the core is a synchrotron of about 25 m diameter, inside which the sources, the lines of injection and the linear accelerator are placed. Outside the main ring there are four extraction lines, about 50 m each, leading the extracted beam into three treatment rooms. In two rooms only a horizontal beam is driven, while the central hall is reached by both a horizontal and a vertical beam. Dose delivering at CNAO is based

on an active scanning system.

Ion acceleration and delivery is divided into several steps. The beam originates from one of the two Electron Cyclotron Resonance (ECR) sources, it then travels along the Low Energy Beam Transfer (LEBT) line, the LINAC and the Medium Energy Beam Transfer (MEBT) line. After being accelerated by the synchrotron, it is extracted into the High Energy Beam Transfer (HEBT) line, finally reaching one of the three treatment rooms. As regards the LEBT, the particles are emitted by the sources with an energy of 8 keV/u; downstream the sources there is a tool to select the ion species. The two possible beams are then reunited in a common line thanks to a switching dipole magnet and brought to the radiofrequency quadrupole (RFQ) and to the Interdigital-H (IH) linac (3 m long tank). With an energy of 7 MeV/u, the particles are injected with the required current into the synchrotron through the MEBT. In the synchrotron there are 16 dipoles and 24 quadrupoles and the beam acceleration is provided by a single RF cavity, tuned to the revolution frequency of the beam. The beam is accelerated to energies between 60 MeV, corresponding to the minimum energy for protons, and 400 MeV/u, which is the maximum energy for carbon ion beams. Finally the particles are extracted through the HEBT, both for the three horizontal irradiation lines and for the vertical line [109].

The beam is capable of achieving, in water, depths between 3 and 27 g/cm^2 and it has an intensity such to provide an average dose rate of 2 Gy/min on treatment volumes of 1000 cm^3. As mentioned before, CNAO is designed for an active dose delivering system; the ion energy is thus varied, as well as the beam direction, in order to reach every spot of the tumor. To obtain an optimized dose distribution into the target volume the Siemens Syngo treatment planning system (based on TRiP98 and the Local Effect Model) is used.

Concerning the radiobiological characterization of the therapeutic beams, both *in vitro* (for protons and C-ions) and *in vivo* (only for C-ions) experiments have been performed. Clonogenic survival following irradiation with hadron beams have been analyzed for three cell lines:

- HSG (human salivary gland tumour)
- T98G (human glioblastoma)
- V79 (Chinese hamster lung fibroblast)

V79 cells represent a reference cell line in radiobiology on which there is a large amount of data in the literature [107]; for this reason it was used also for the present work. The Carbon SOBP shown in figure 2.12 was used for this radiobiological beam characterization; the cells were irradiated at 5 different depths: one at the entrance plateau (4 cm depth), one in the proximal part (12.5 cm), one at the centre (14 cm) and two in the distal part of the SOBP (16 and 17.5 cm). The cells were irradiated with several dose values: 0, 0.5, 1, 2, 3, 4, 5 Gy. The ranges of RBE values found for these irradiations were in

agreement with those found at NIRS, in Japan. The dose-survival curves obtained for V79 cells were used for comparison with simulation results obtained in the context of this thesis work, as illustrated in Section 4.2.3.

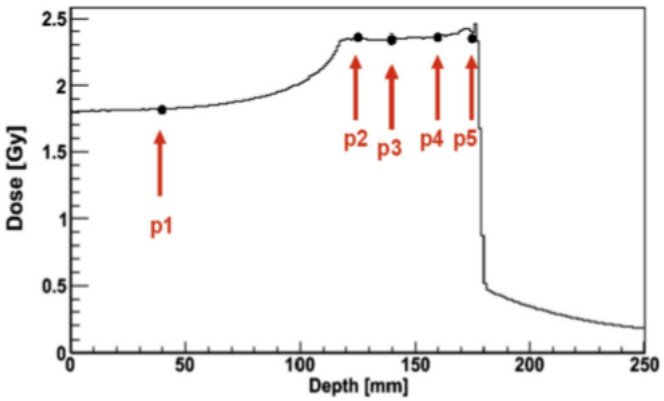

Figure 2.12: Location of the irradiation positions along the spread-out Bragg peak used for *in vitro* experiments at CNAO [107]

Moreover, in order to complete the characterization of the therapeutic carbon ion beams, the RBE along the same SOBP was also measured through the simultaneous irradiation of multiple targets (41 points) placed along the beam axis and the evaluation of cell survival levels. The physical dose in the SOBP was uniformly set to 2 Gy. In addition to the *in vitro* tests, *in vivo* experiments were also performed for the evaluation of RBE values along the therapeutic carbon ion beams on a reference biological system, i.e. the intestinal crypt regeneration in mice. Irradiations were made at three different positions along the SOBP: proximal (13 cm depth), middle (15 cm) and distal (17 cm). Although a deeper analysis of the *in vivo* procedure is beyond the aim of this work, it is worth mentioning that the carbon-ion beam at CNAO was found to be biologically equivalent to the ones of NIRS and GSI.

2.3.2 CATANA

In 1995 scientists from the LNS-INFN laboratories decided to project a protontherapy facility based on a super-conducting cyclotron, with a chosen fixed energy of 62 MeV, suitable for the irradiation of ocular and iris melanomas. Officially started in 1996, CATANA was the first italian protontherapy center. In 2002 the first Italian patient, affected by ocular melanoma, was treated [110]. With a regimen of about 40 patients per year, the total number of treated patients till now is more than 400. Most of treated tumors are uveal melanoma, but even other patologies can be treated, such as: conjunctival melanoma, conjunctival rhabdomyosarcoma, conjunctival lymphoma, conjunctival papilloma, eyelid carcinoma, lachrymal gland carcinoma and choroideal metastases. A

local tumor control was obtained in 95% of treated patients. Since an important endpoint of protontherapy is the maintenance of the eye, it is important to highlight that this goal was achieved in about 90% of the cases. Moreover, some radiation-induced damages appeared, such as retinal detachments of various degree in about 35% of patients and radiation retinopathy of various degree in about 22% of patients [111]. The problem of the presence of an organ at risk like retina just beyond the tumor region will be addressed in Section 4.2.2.

Concerning the CATANA accelerators and beam lines, protons are produced by one ECR source and they are accelerated by the LNS Superconducting Cyclotron (CS), a compact strong focusing machine. The pole radius is 90 cm and the magnetic field at the center ranges from 2.2 to 4.8 T. The operational radio frequency system ranges between 15 and 48 MHz, allowing for proton energies between 45 and 100 MeV [112]. For the purposes of clinical treatments the energy is fixed at 62 MeV, confining the maximal proton beam range to about 30 mm, sufficient for the irradiation of intraocular tumours. Since the energy is not varied during irradiation, the shaping of the SOBP is obtained by passive methods (like those illustrated in Section 2.1.2), and the required maximum range for a specific treatment is set by a simple Perspex absorber, variable in thickness in steps of 0.2 mm.

When extracted from the cyclotron, the proton beam exits in air through a 50 μm kapton window placed at about 3 meters from the isocenter. A double foil scattering system is used, optimised to obtain a good homogeneity in terms of lateral off-axis dose distribution, minimizing the energy loss. The traversal dose distribution of the beam has a width of about 25 mm. A range shifter and range modulator are placed downstream of the scattering system.

As regards proton dosimetry, for mono-energetic and modulated proton beams, depth-dose distributions are measured in a home-made motorized computer controlled water phantom. An Advanced Markus chamber is used and the experimental depth-dose profiles are compared with a Monte Carlo simulation application, based on the Geant4 toolkit. Figure 2.13 (panel *a*) shows the depth-dose distribution obtained with the Markus chamber for the unmodulated full energy (62–MeV) beam [113]. The Full Width at Half Maximum of the Bragg Peak is 2.76 mm. In order to obtain therapeutic SOBPs, wheel modulators have been developed and proton beam energies lower than 62 MeV are obtained inserting PolyMethylMethAcrylate (PMMA) range shifters of different thickness along the beam path. Figure 2.13 (panel *b*) shows the SOBP obtained with the first prototype of the modulator wheel.

Finally, concerning treatments, 60 Gy (RBE) are delivered to uveal melanoma in 4 fractions on 4 consecutive days. As usual for protontherapy, no radiobiological model is implemented into the treatment planning system, and proton RBE is assumed to have the constant value of 1.1. However, characterizations of proton effectiveness along a therapeutic CATANA SOBP were made, such as that by Chaudary and collaborators [45]. In that case the AG01522 cell line

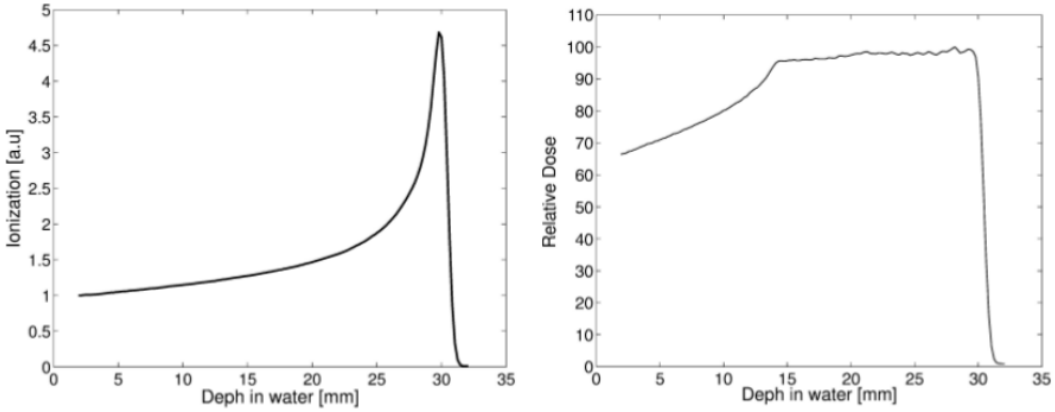

Figure 2.13: (a) Bragg peak of 62-MeV proton beam acquired in a water-tank with the Markus ionization chamber at CATANA facility; (b) SOBP obtained with a modulator wheel [113]

and the U87 glioma cell line were irradiated in six positions at different depths: before, along and just beyond the SOBP. For AG cells, an increase of RBE till values of almost 3 (for a 10% survival level) was found, in contrast with the clinical assumption. More details however can be found in Section 4.2.2, where a systematic study on this issue is presented. Comparisons between experimental data and simulations will be shown, with predictions on proton effectiveness variations as a function not only of depth and LET but also of target radiosensitivity, biological endpoint and considered dose level.

Chapter 3

Results - Part I: model development

In the context of the modelization of radiation effects in biological targets, a model has been developed since 1999 by Francesca Ballarini et al. at the University of Milano, the University of Pavia and the National Institute of Nuclear Physics (INFN), Italy. The model, basing on few mechanistic assumptions and making use of a small number of adjustable parameters, has the main aim of shedding light on some radiobiological open questions. Implemented in the form of a (home-made) Monte-Carlo (MC) code, the model has been originally developed for chromosome aberrations and subsequently extended to cell death. Different versions have been developed during the past years. In Section 3.1 the first model versions, preceding the present thesis work, will be briefly illustrated. In Section 3.2 the extension to cell death, partially performed within this thesis, will be described. Finally in Section 3.3 the current version, entirely developed in the framework of this thesis, will be introduced.

3.1 The first model versions, specific for chromosome aberrations

Since the first model version [114], a pivotal role in biological radiation-induced damage has been attributed to chromosome aberrations, assumed to arise from mis-rejoining or unrejoining of chromosome fragments. Originally, chromosome aberrations were assumed to arise from severe DNA damage types called "Complex Lesions" (CLs), operationally defined as "at least two SSBs on each DNA strand within 30 base-pairs", that is the aforementioned DSB^{++} [33]. The model has been applied to normal human lymphocytes exposed to alpha particles. The mean number of CLs per Gy and per Dalton induced by alpha particles of different LET has been taken from [115] and converted into CLs per unit track length. The CLs were then distributed along the tracks

of the primary particles and the probability for a chromosome territory to be crossed by a given track was dependent on its volume, which was assumed to be proportional to its DNA content; interphase chromosome localization was not described explicitly. The number of CLs induced by a given primary particle in each traversed chromosome was extracted from a Poisson distribution and each CL was then assigned to one of the two chromosome arms proportionally to the arm DNA content. Each CL was assumed to cause a break in the chromosome, thus leading to the production of two independent chromosome fragments. The possible outcomes of chromosome fragments interaction were: mis-rejoining, (accidental) eu-rejoining, or un-rejoining (as illustrated in Section 1.3.1). Each fragment was assumed to have the same probability to interact with every other possible partner, without any distance dependence. The subsequent steps consisted of simulating the scoring of aberrations, repeating the procedure for a number of code runs sufficiently high to obtain statistically significant results, and repeating the entire process for different doses, to obtain simulated dose-response curves following acute irradiation. Good agreement was found with experimental data taken from the literature; however there was a tendency to overestimate the so-called "complex exchanges", which by definition involve at least three chromosome breaks in at least two chromosomes. This tendency suggested that proximity effects needed to be introduced.

In a subsequent version [116] [117] [118], interphase chromosome localization in chromosome territories was modelled explicitly, and proximity effects were taken into account. To define the 46 interphase chromosome territories within a 3 μm radius sphere (representing a human lymphocyte nucleus), a 3D lattice of 27000 cubic voxels (each one with 0.2 μm side) was superimposed to the sphere, and a number of voxels proportional to the DNA content was assigned to each chromosome territory. The step-by-step construction of the territories will be described in detail in Section 3.2. In that version the voxels - and thus the chromosomes - hit by each CL were identified, and each CL was assigned to one of the two chromosome arms according to the arm DNA content. Exchange-type aberrations were assumed to be originated only by close fragments, that is by chromosome free-ends originating from two CLs induced either in the same chromosome territory (intra-changes), or in distinct but adjacent territories (inter-changes). This assumption was implemented in the simulation code introducing a cut-off distance d: two chromosome free-ends were allowed to undergo end-joining only if their (initial) distance was smaller than d, and within d each pair of fragments had the same end-joining probability. The value of d was set to 1.5 μm. While for light ions the CL yields were taken from [115], for gamma rays irradiation the CL yields were adjusted *a posteriori* following comparison with experimental data. Both calculated dicentric yields for 5 keV/μm protons and 86 keV/μm alpha particles (as shown in Figure 3.1), as well as calculated "F-ratios" (i.e. ratios of dicentrics to centric rings) for gamma rays, 5 keV/μm protons and 121 keV/μm alpha particles,

were in good agreement with experimental data.

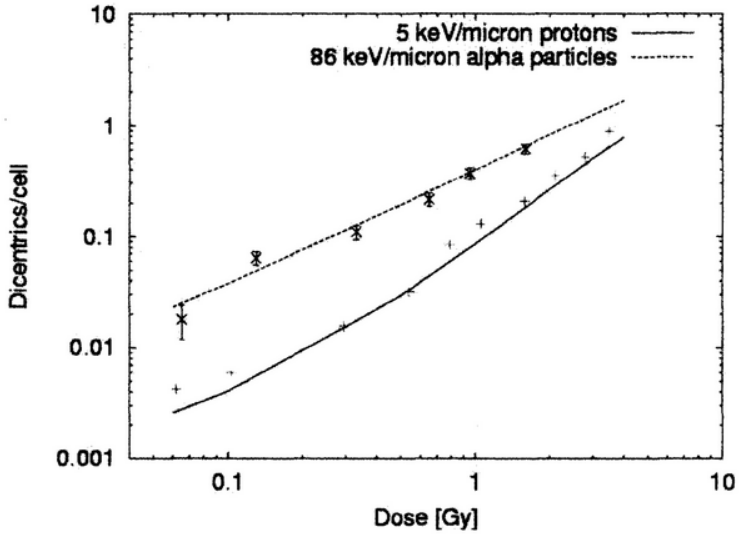

Figure 3.1: Results obtained by one of the first model versions: calculated yields of dicentric chromosomes induced by different doses of 5 keV/μm protons (solid line) and 86 keV/μm alpha particles (dashed line). The experimental data for comparison were taken from [119] (5 keV/μm protons) and [120] (86 keV/μn alpha particles) [118]

Calculated dose-responses curves for non-lethal aberrations, in particular reciprocal translocations, in human lymphocytes exposed to gamma rays were also compared to FISH experimental data, especially for low-dose *in vitro* irradiation [121] [122]. As an application in the field of space research, the model was applied to predict aberration yields in lymphocytes of astronauts involved in long-term missions onboard the MIR space station or the International Space Station. The calculated dicentric dose-response curves were in good agreement with astronauts' data [122]. Since 2007 the model has been extended to the case of heavy ions irradiation [123] [124]. To take into account the action of "delta rays" (i.e. high energy electrons produced by primary ions), some CLs were radially "shifted" from the primary track core. A detailed description of how this process is currently performed will be provided in Section 3.2. Good agreement was found with PCC (Premature Chromosome Condensation) experimental data [125], measuring "simple exchanges" (dicentrics plus translocations) in human lymphocytes exposed to 1 GeV/u Fe-ions and 290 Mev/u C ions. A more comprehensive review on this first model versions can be found in [126].

3.2 The BIANCA model

In this section, a more recent version of the model, which has been called BIANCA (BIophysical ANalysis of Cell death and chromosome Aberrations), will be described. This version, mainly characterized by the extention to cell death and by the application to other cell lines, represented the starting point for the present thesis work. Within the original work carried out for this thesis, some "technical" improvements (such as the behaviour of heavy ions) were introduced, as well as the extention to some specific ion types for hamster cells and the extention to normal human fibroblasts (see Section 3.2.3).

3.2.1 Assumptions and parameters

Starting from 2010 [64] the model has been extended to cell death. Since very few data are available on the survival of lymphocytes, which are generally grown as cell suspensions, fibroblast nuclei were implemented in the code. The extended model, called BIANCA, is based on the following assumptions:

1. radiation induces clusters of DNA lesions called "cluster lesions" (CL), and each CL produces two independent chromosome free-ends

2. only free-ends having initial distance below a threshold d participate in the process of end-joining, which leads to chromosome aberrations in case of mis-rejoining

3. dicentrics, rings, and large deletions (visible in Giemsa staining) lead to clonogenic inactivation. We will refer to these aberration types as Lethal Aberrations (LA).

Assumptions 1 and 2 arise from the evidence that, on average, 1 Gy of radiation induces a DSB yield in the order of ∼30–40 DSBs per cell, but only ∼1 chromosome aberration per cell or even less (as mentioned in Section 1.2.3). According to Schipler and Iliakis [25] DSB complexity is considered as a key determinant of the risk for repair errors, which lead to adverse biological effects such as chromosome aberrations and cell death. It is therefore very likely that among the many initially induced DSBs, only those that are complex enough (assumption 1) and close enough (assumption 2) are involved in the formation of chromosome aberrations. Since a characterization of the critical DNA cluster damage is still an open question, an *a priori* definition of cluster lesions is not provided in the model, leaving the yield of CLs (i.e. average number of CLs per Gy and per cell) as a first adjustable model parameter.

Concerning the rejoining probability between chromosome free-ends, a step-like distance dependence was chosen (rather than other relationships, such as those discussed in Section 1.3.1). This choice is due to experimental evidences suggesting that DNA repair takes place within the channels separating the various interphase chromosome domains [127], possibly due to the presence of

repair centers where chromatin breaks initially induced 1–2 μm apart can interact, thanks to the action of DNA damage-sensing proteins such as 53BP1 [128]. This was implemented in the model, assuming that every free-end will undergo rejoining with one of the possible "partners" (randomly choosen) within the threshold distance d with 100% probability, whereas free-ends with larger initial distance will never join; the rejoining probability dependence is thus a step-like function of the initial distance. d is the second, and last, model parameter. The fact that d is the initial distance implies that, after the induction of CL by radiation, the various free-ends can move in the cell nucleus, reflecting the evidence that DNA repair is a dynamic process [95].

Assumption 3 is based on an experimental study on AG1522 cells exposed to different doses of X-rays [40], in which a one-to-one relationship was found between the average number of LA per cell and the logarithm of the cell surviving fraction (see Section 1.2.3). This experimental result is illustrated in Figure 1.9. While the study by Cornforth and Bedford was specific for photons, with the BIANCA model the approach was extended to other radiation types including protons, alpha particles and heavier ions, applying the idea that after the initial damage has been induced, the target cell "forgets" about radiation quality. Of course, caution is needed in generalizing this relationship, since other aberration types (typically, non-transmissible complex exchanges) and/or other damage types (e.g., mutations) can also be involved in cell killing.

3.2.2 Modelization of target cells and irradiation

With the BIANCA model version, the cell nucleus could be represented by different geometrical shapes (e.g. a sphere or a cylinder with circular or elliptical base), according to the considered cell line and the irradiation conditions. Each interphase chromosome territory was modelled as an (irregular) intra-nuclear region, consisting of the union of adjacent cubic voxels of 0.2 μm side. The number of voxels constituting a given chromosome territory should be proportional to the DNA content of that chromosome. The first step for the construction of chromosome territories consisted of randomly-selecting a "starting voxel" (*seed*) for each chromosome territory. A new voxel, randomly-selected among the six closest neighbours of the *seed*, was then chosen. In each subsequent step, new voxels were assigned to every territory; ideally for each chromosome the procedure should stop only after the territory had reached the established dimension. In practice this is unfeasible, and in some cases one or more chromosome territories might have a smaller dimension than expected (i.e. some voxels might be "empty"). Finally, each of the voxels assigned to a given chromosome territory was associated to one of the two chromosome arms, applying a probability proportional to the arm DNA content. In figure 3.2 a top view of a simulated cell nucleus in interphase modeled as a cylinder with elliptical base is represented. The two axes of the elliptical base are 20 μm and 10 μm respectively, and the 46 human chromosome territories are represented in different colors.

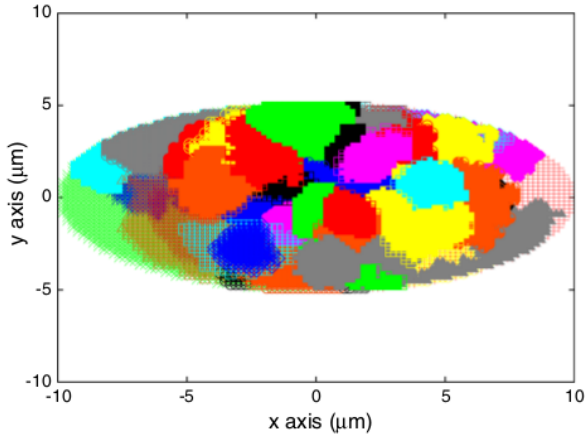

Figure 3.2: Simulated human fibroblast cell nucleus (*top view*), with the 46 interphase chromosome territories represented in different symbols [129]

Concerning the simulation of irradiation, for each cell line and radiation quality an average number of CLs per Gy and per cell was fixed as an input parameter. For X-rays the CL yield was multiplied by the dose D; for each cell, an actual number of CLs was then extracted from a Poisson distribution (the mean is the yield of CLs per cell), and those lesions were uniformly distributed within the nucleus volume. On the contrary, for protons (and He ions) the CLs were assumed to be distributed along the core of the primary tracks. The starting point was the average number of CLs per micrometre induced by a particle track. It is possible to write the average number of CLs per cell as

$$\left\langle \frac{CL}{Gy \cdot cell} \right\rangle \cdot D = N \cdot \left\langle \frac{CL}{\mu m} \right\rangle \cdot l \tag{3.1}$$

where D is the dose in Gy, N the number of traversing particles and l is the length of the nucleus traversals in μm. By using Equation 1.11, the mean number of CLs per micrometre therefore can be calculated as follows

$$\left\langle \frac{CL}{\mu m} \right\rangle = \left\langle \frac{CL}{Gy \cdot cell} \right\rangle \cdot \frac{0.16 \cdot LET}{V} \tag{3.2}$$

where V is the cell nucleus volume in μm^3 and the LET is expressed in keV/μm. The average number of CLs per nucleus traversal was obtained multiplying CL/μm by the traversal length; in the case of cylindrical geometry, this lenght corresponds to the axis of the cylinder when the irradiation is perpendicular to the cylinder base. For each traversal, an actual number of CLs was then extracted from a Poisson distribution, and those lesions were uniformly distributed along a segment representing the particle track. The average number of particles traversing the cell nucleus following a dose D was calculated according to Equation 1.11, and an actual number of traversals was extracted from a Poisson distribution.

Finally for heavier ions, like Carbon or Iron, the contribution of "delta rays" emitted by the primary ions was also taken into account. More specifically, each CL induced by a heavy ion was assumed to have a 0.5 probability to be located along the primary track and a 0.5 probability to be radially shifted. The 0.5 value is an application of the idea that half of the total energy deposition derives by excitations and electron plasma oscillations, which mainly occur in the track core, whereas the remaining half derives from ionizations induced by secondary electrons, which mainly occur in the so-called "penumbra" [130]. For a radially shifted CL, the probability to fall at a distance r from the primary track core was taken as proportional to r^{-2}. Starting from this thesis work, this probability has been taken as proportional to r^{-1}; according to Equation 1.32 in fact the dose is proportional to r^{-2} (outside the track core) and the energy is thus proportional to r^{-1}. Since the number of CLs per unit volume is proportional to the dose (according to the model), the number of CLs in a specific region is proportional to the product between dose and volume, i.e. the energy. The probability for a CL to fall at a distance r from the center of the track, as shown in Figure 3.3, is thus given by

$$P(r) = \begin{cases} h & r < r_{min} \\ k\dfrac{1}{r} & r_{min} \leq r \leq r_{max} \\ 0 & r > r_{max} \end{cases} \tag{3.3}$$

where h and k are two parameters to be determined, r_{min} is the radius of the track core (set to 2 nm) and r_{max} is the maximum radial distance for δ-electrons (calculated by Equation 1.12 and depending on the projectile energy). By integrating, applying the boundary conditions and normalizing the whole probability to 1, it is possible to obtain a system of two equations

$$\begin{cases} \displaystyle\int_0^{r_{min}} h\mathrm{d}r = h \cdot r_{min} = k \\ \displaystyle\int_0^{r_{min}} h\mathrm{d}r + \int_{r_{min}}^{r_{max}} k\frac{1}{r}\mathrm{d}r = h \cdot r_{min} + k\ln r_{max} - k\ln r_{min} = 1 \end{cases} \tag{3.4}$$

The two parameters can thus be calculated as follows

$$\begin{aligned} k &= \frac{1}{1 + \ln\dfrac{r_{max}}{r_{min}}} \\ h &= \frac{k}{r_{min}} \end{aligned} \tag{3.5}$$

These parameters only depend on the primary ion energy (typically expressed in MeV/u). All ions heavier than He are treated in the same way; the only

difference relies on their initial energy (depending on their mass) and thus on the value of r_{max}. The possible contribution of high-energy secondary electrons emitted by primary ions not traversing the cell nucleus was also taken into account, making the ions start from a larger region with respect to the nucleus cross-sectional area. Some outer tracks may thus give a contribution to dose deposition inside the cell nucleus, while some inner tracks may deposit part of their energy outside the nucleus.

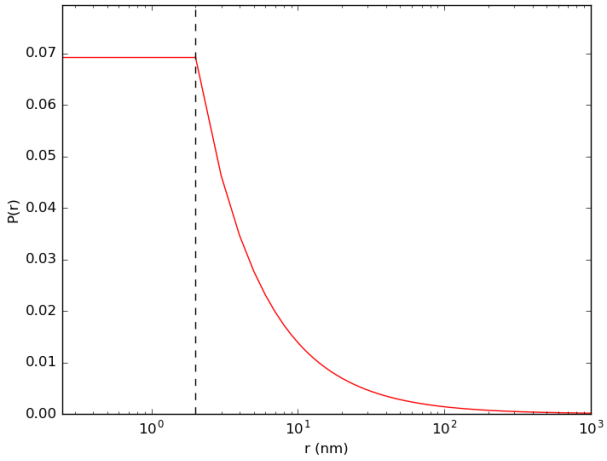

Figure 3.3: CL radial distribution probability in the case of $r_{min} = 2$ nm and $r_{max} = 1$ μm (the linear-logarithmic scale is used just for practical reasons)

After assigning a position to each CL, the subsequent steps consisted of: 1) identification of the chromosome and the chromosome arm that was hit by each CL; 2) end-joining between randomly selected pairs of chromosome free-ends within a threshold distance d; 3) scoring of dicentrics, rings, and deletions visible in Giemsa, basing on the number of centromeres, the shape (linear or circular) and the possible association with acentric fragments; 4) repetition for a statistically significant number of runs and calculation of the average number of LAs per cell and the corresponding surviving fraction as S(D) = $e^{-<LA(D)>}$; 5) repetition for different doses to obtain simulated dose-response curves directly comparable with experimental data. Specific background aberration yields can be included. To reproduce the experimental Giemsa scoring, fragments smaller than 3 Mbp were considered not visible, according to what reported in [40]. When a CL falls in an "empty" voxel, its position is randomly re-extracted (in the case of X-rays) or the whole track is "re-launched" in another random position (in the case of ions); this solution may lead to small biases related to the non-perfect geometry of the simulated cells, and in this thesis work it was changed, as illustrated in Section 3.3.1.

In conclusion, in order to simulate an *in vitro* experiment, several input data are necessary: the particle type, that is photons, protons, He ions or

heavier ions; the particle LET and the irradiation dose (which is essential to determine the number of tracks; more dose levels are necessary to obtain a dose-response curve); the particle energy (essential only in the case of heavy ions, to calculate r_{max}); the target characteristics, i.e. its shape, dimensions and chromosomal content; the number of runs (chosen in order to obtain a significative statistical level); the CL yield and the value of the threshold distance d. While all other data are simply determined by the physical and biological experimental features, the two last values are the only adjustable parameters of the BIANCA model, to be tuned through the comparison with experimental data, as described in the two following Sections.

3.2.3 Testing against experimental data

A fundamental step for the validation of the BIANCA model consisted of a systematic comparison between simulation results and experimental data on the irradiation of V79 normal hamster fibroblasts and of AG1522 (or AG01522) normal human fibroblasts with different radiation qualities. As a general guide, for each data set making use of a single cell line the comparison with a reference radiation curve (tipically photons) allowed deriving a value for the rejoining threshold-distance d, which was maintained unchanged for the ion simulations. The parameter d in fact represents a typical characteristic of the target, and should be independent of radiation quality. After fixing d, the comparison with a survival point (that is, survival after a certain dose) relative to a given ion type and energy allowed deriving a CL yield (average number of CLs per Gy and per cell) for that ion type and energy, which was then used as code input to predict cell killing at the other doses. The yield of CLs is expected to mainly depend on the projectile properties; therefore each particle type and energy should be characterized by its own CL yield. Some modulation is also expected by the considered cell line, depending on the specific features of the cell repair mechanisms.

V79 cell nuclei were modeled as cylinders with circular base, with height and radius of 6 μm. Also smaller values are reported in the literature for the thickness of these cell nuclei, but such values in general refer to electron microscopy measurements; more recent measurements based on confocal microscopy, especially in living cells, provide larger values. For instance, both Belli et al. [46] and Bettega et al. [131] report about 6 μm for the average thickness of V79 cell monolayers (which implies a nucleus thickness of about 5 μm if one considers a cytoplasm thickness of about 1 μm [132]) whereas according to Hill et al. [133], the thickness of V79 nuclei is about 7 μm. This led us to choose 6 μm as an intermediate value.

In a work preceding this thesis [134] simulated survival curves were compared with survival data on V79 cells exposed to different mono-energetic beams of protons or Carbon ions, as well as a reference radiation (X-rays). The proton data set consisted of five proton beams having LET values of 7.7, 11.0, 20.0, 30.5 and 34.6 keV/μm, corresponding to energy values of 5.01, 3.20,

1.41, 0.76 and 0.64 MeV, respectively [46]; the irradiated cell line was V79-753B cell monolayers. A good agreement with the X-ray experimental curve was found with d=5 μm and a CL yield of 1.8 CLs·Gy^{-1}·cell^{-1}. For protons, d was maintained fixed at 5 μm, whereas for each of the five proton energies a CL yield was derived comparing the simulation results with the experimental data relative to that energy; the derived CL yields were in the range 2-4 CLs·Gy^{-1}·cell^{-1}.

Concerning the carbon-ion data set, four carbon beams were considered, with LET values of 339.1, 153.5, 32.4 and 13.7 keV/μm, corresponding to energies of 4.2, 11.0, 76.9 and 266.4 MeV/u, respectively. A smaller d was expected, because the cells used in the experiment were smaller. A good agreement with the X-ray experimental curve was found with d=4 μm and a CL yield of 1.3 CLs·Gy^{-1}·cell^{-1}. The difference in the CLs yields for the two experiments may reflect the differences in radiosensitivity between the two cell lines. As in the case of protons, for carbon ions d was maintained fixed at 4 μm and the CL yield was adjusted for each energy; the derived CL yields were in the range 2–6 CLs·Gy^{-1}·cell^{-1}. The simulated survival curves and the corresponding experimental data are shown in Figure 3.4. The agreement between simulated and experimental survival curves, both for protons and carbon ions, supported the assumptions on the mechanisms.

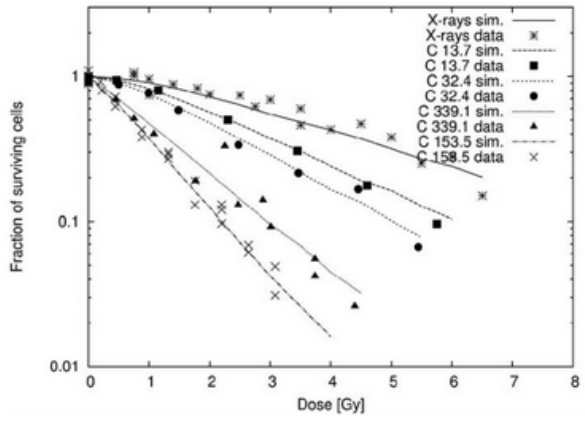

Figure 3.4: Survival curves for V79 cells exposed to X-rays and to four carbon-ion beams of different energy. The lines are simulation results, whereas the points are experimental data taken from [134]

A further step, performed within this thesis work, consisted of the extension to AG1522 normal human fibroblasts exposed to several ion types. The cell nuclei were modeled as cylinders with elliptical base (height: 4 μm; major axis: 20 μm; minor axis: 10 μm). This is consistent with Bolzer et al. [135], who represented the nuclei of these cells by an ellipsoidal shape with average axes of 20 μm (major axis), 10 μm (minor axis) and 5 μm (height), determined from light-optical stacks. To have a similar nucleus volume by a cylindrical shape

rather than an ellipsoidal shape, the cylinder height must be smaller; for this reason, in our simulations we chose a nucleus thickness of 4 μm.

First of all the action of X-rays as a reference radiation was studied. Figure 3.5 (panel *a*) shows the simulated cell surviving fraction for doses up to 12 Gy, togheter with experimental data points taken from the literature [40]. On the contrary, in Figure 3.5 (panel *b*) the total yields of lethal aberrations (dicentrics plus rings plus large deletions), following X-rays exposure, are plotted. Moreover in the same panel the calculated yields of lethal aberrations for the same cell line exposed to 116 keV/μm alpha particles are also shown, compared with experimental data obtained by the same authors in a subsequent work [136]. A value of 3 μm was used for the threshold distance d, while values of 2 CLs·Gy^{-1}·cell^{-1} and 9.4 CLs·Gy^{-1}·cell^{-1} were used for X-rays and alpha particles, respectively. With these values a good agreement with the data (considering the experimental error bars) was found.

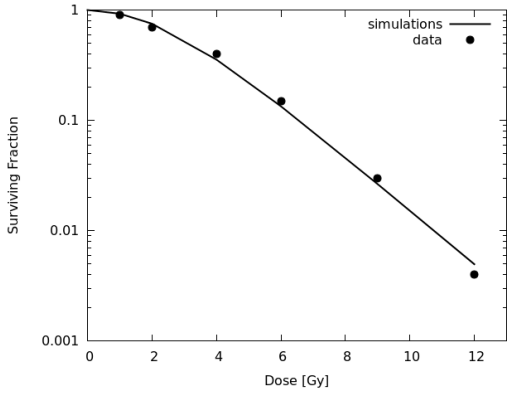

(a)

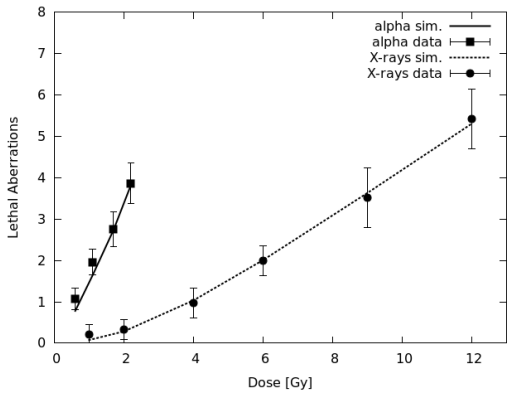

(b)

Figure 3.5: (a) Surviving fraction for AG1522 cells exposed to X-rays; (b) Average number of total lethal aberrations per cell for AG1522 cells exposed to X-rays and 116 keV/μm alpha particles. In both cases the lines are simulation results, whereas the points are experimental data [129].

The approach was then extended to two other AG1522 data sets taken from the literature: the first one [137] on gamma rays, 50 MeV He-ions (16.2 keV/μm), 320 MeV C-ions (76.3 keV/μm), 220 MeV C-ions (108 keV/μm), 350 MeV Ne-ions (321 keV/μm), and 260 MeV Ne-ions (437 keV/μm); the second one [138] on gamma rays and 2.9 MeV alpha particles (132 keV/μm). All curves were obtained with $d = 5$ μm; the difference with respect to the 3 μm value used for Cornforth and Bedford's data may be explained by differences between the cell lines and the experimental protocols: for instance, Cornforth and Bedford worked with delayed cell plating after irradiation, whereas the other authors worked with immediate plating. The calculated survival curves for these radiation types are reported in figure 3.6, together with the corresponding experimental data. In order to reach a good agreement with the data, the two photon curves were obtained with 2.1 CLs$\cdot$Gy$^{-1}\cdot$cell^{-1} and 2.4 CLs$\cdot$Gy$^{-1}\cdot$cell^{-1} respectively, whereas the CL yields used for the ion curves ranged between 3 CLs$\cdot$Gy$^{-1}\cdot$cell^{-1} (for 50 MeV He ions) and 18 CLs$\cdot$Gy$^{-1}\cdot$cell^{-1} (for 2.9 MeV alpha particles). The parameter values were within the ranges consistent with their biophysical meaning, suggesting that the considered DNA cluster lesions are likely to be less rare than the so-called DSB^{++}, which for low-LET protons have been calculated to be <1 per Gy and per cell [115] [139]. Possible candidates might be multiple DSBs localized in larger genomic regions with respect to the 30 bp used to define DSB^{++}. This is consistent with the hypothesis by Schipler and Iliakis [25] and also with the yields of "reactive DSBs" obtained by Chen et al. [140] (defined as DSBs that are severe enough to lead to chromosome aberrations following mis-rejoining of chromosome fragments). A more detailed discussion on this type of damage will be provided in Chapter 4.

Finally, as an original part of this thesis work, a systematic study on the irradiation of the two considered cell lines with radiation qualities of increasing mass and LET was performed [141]. This study had the double aim of completing the model testing and investigating the dependence of the CL yields on LET. The considered data sets used for comparison were the following ones: V79 cells exposed to X-rays and protons [142], V79 cells exposed to γ-rays and alpha particles [143] [144] [145], AG01522 cells exposed to X-rays and protons [45], AG01522 cells exposed to carbon ions [146], and AG1522 cells exposed to γ-rays and iron ions [147]. Photons were mainly used as a reference radiation; the differences in the photon responses may reflect the radiosensitivity of the slightly different considered cell lines (V79-379A for Folkard et al.; V79-4 for Thacker et al. and Phoenix et al.; V79-753B for Belli et al.; AG01522 for Chaudhary et al. and Kavanagh et al.; AG1522 for Tsuboi et al.). The comparison between simulations and experimental data will be presented on the basis of the type of particle used for the irradiation: photons, protons, helium ions and heavier ions (carbon and iron). Moreover the value of the threshold distance d which led to a good agreement with the photon survival curve was unchanged for all ion simulations; for both hamster and human fibroblasts, d

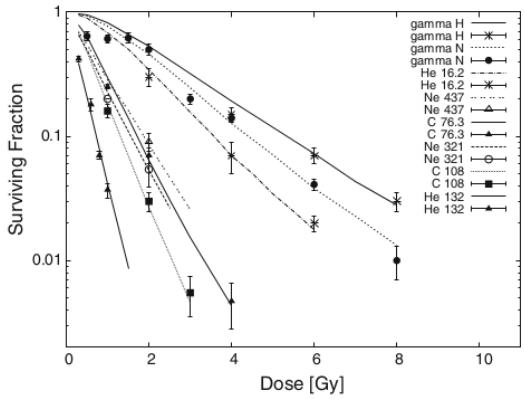

Figure 3.6: From top to bottom: survival of AG1522 cells exposed to γ-rays (two curves: the upper one compared with data from Hamada et al. 2006, and the lower one compared with data from Neti et al. 2004), 50 MeV He ions (16.2 keV/μm), 260 MeV Ne ions (437 keV/μm), 320 MeV C ions (76.3 keV/μm), 350 MeV Ne ions (321 keV/μm), 220 MeV C ions (108 keV/μm), and 2.9 MeV alpha particles (132 keV/μm). The lines are simulation results, whereas the points are experimental data taken from Hamada et al. 2006 (upper gamma curve, He ions, C ions, and Ne ions) or Neti et al. 2004 (lower gamma curve and alpha particles) [129]

was fixed at 5 μm.

Figure 3.7 (panel *a*) shows survival curves for V79 cells exposed to γ-rays [144] [46] [145] and X-rays [142], AG1522 cells exposed to γ-rays [138] and AG01522 cells exposed to X-rays [45]. All the curves were obtained with $d =$ 5 μm. Smaller d values tended to underestimate the effectiveness of low doses and to overestimate the effectiveness of high doses, whereas higher values would not be in line with the biophysical meaning of this parameter. The CL yields were in the range 2-4 CLs$\cdot$Gy$^{-1}\cdot$cell^{-1}, with lower values for hamster cells and higher values for human cells.

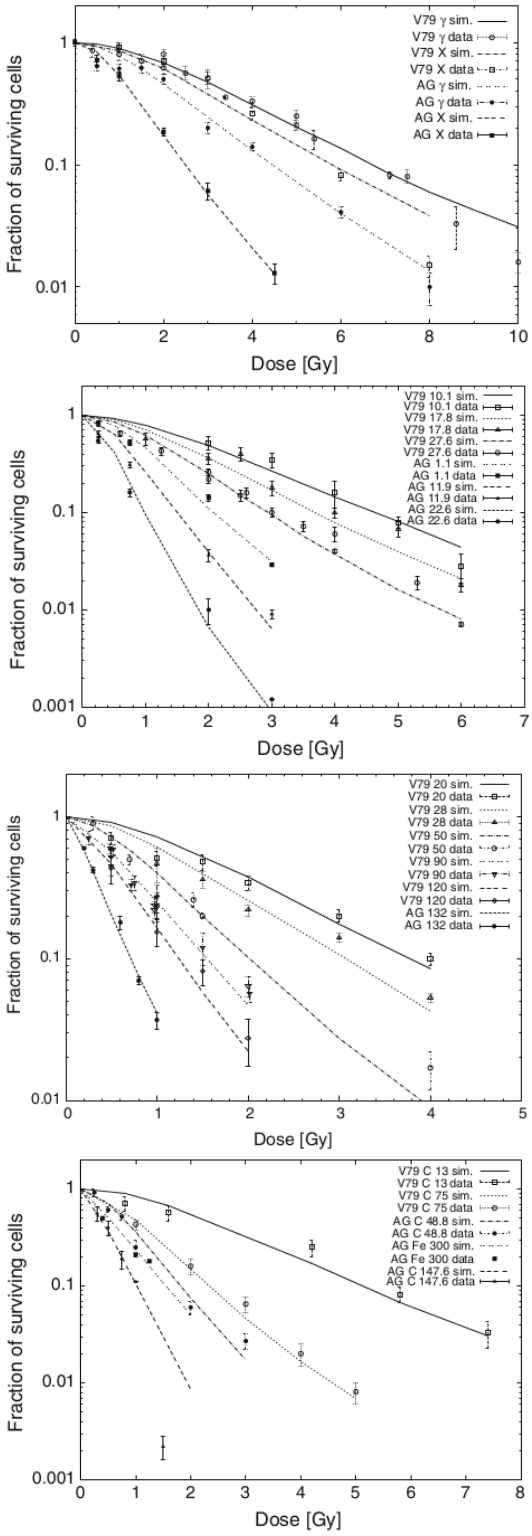

Figure 3.7: (a) Survival of V79 and AG1522 cells exposed to X- or γ-rays; (b) Survival of V79 and AG01522 cells exposed to different monoenergetic proton beams; (c) Survival of V79 and AG1522 cells exposed to He ions of different LET; (d) Survival of V79 and AG1522 cells exposed to different heavy-ion beams. The lines are simulation results, the points are experimental data [141]

Figure 3.7 (panel *b*) shows survival curves for V79 cells exposed to monoenergetic proton beams with a LET of 10.1, 17.8 and 27.6 keV/μm [142] [46], and for AG01522 cells exposed to monoenergetic protons of 1.1, 11.9 and 22.6 keV/μm [45]. According to the meaning of the threshold distance d, the value of this parameter was left unvaried with respect to the photon simulations. The yield of cluster lesions, adjusted separately for each curve, were in the range $\sim$2–12 CLs$\cdot$Gy$^{-1}\cdot$cell^{-1}. Some of the simulated curves (especially for the highest considered LET values) tend to show a slope decrease at the highest considered doses. This may reflect the model assumption that cell inactivation derives from simple aberrations, and does not take into account the role of complex exchanges, which start becoming important at high doses. It is also likely that the dose above which this phenomenon becomes important depends on radiation quality: in general, the expected slope change should occur at higher doses for low LET radiation with respect to high LET.

Figure 3.7 (panel *c*) shows survival curves for V79 cells exposed to alpha particles of 20, 28,50, 90 and 120 keV/μm [143] [144] [145], and for AG1522 cells exposed to 132 keV/μm alpha particles [138]. Like for protons, d was maintained unvaried at 5 μm, whereas the CL yield was varied to find a good agreement with the data, in the range $\sim$3–18 CLs$\cdot$Gy$^{-1}\cdot$cell^{-1}.

Finally, Figure 3.7 (panel *d*) shows survival curves for V79 cells exposed to carbon ions of 13 and 75 keV/μm [46], AG1522 cells exposed to C ions of 48.8 and 147.6 keV/μm [146], and AG1522 cells exposed to Fe ions of 300 keV/μm [147]. Again, d was maintained at 5 μm, whereas the yields of cluster lesions were varied in the range $\sim$2–12 CLs$\cdot$Gy$^{-1}\cdot$cell^{-1}.

Some of these curves tend to show an overestimation of cell survival at low doses (typically around 1 Gy or less). This might be related to the so-called incomplete exchanges, that is those chromosome aberrations for which not all the involved chromosome fragments find a "partner" for rejoining, giving rise to additional acentric fragments; in the BIANCA model all exchanges were assumed to be complete. A possible solution to this problem will was explored in the BIANCA II version, as illustrated in Section 3.3.1. However, a good general agreement of BIANCA with the considered experimental data was obtained by adjusting only one free parameter (the CL yield), after fixing the threshold distance parameter through the comparison with photon survival curves. Nevertheless a value of 5 μm for d appears to be too large with respect to most values reported in the literature [128]; also this issue was addressed in the BIANCA II version, in which smaller values were considered.

All the values used for the CL yield parameter, depending on radiation quality (type and energy), are reported in table 3.1. This information will be of fundamental importance for the study reported in Section 4.1, aimed to provide a characterization for the types of DNA complex lesions that have a role at inducing chromosome aberrations and cell death. Some of the values reported in the table are not shown graphically shown in the Figures.

Cell line	Radiation type	LET (keV/μm)	CLs/(Gy·cell)
V79	γ-rays		1.6
V79	X-rays		1.7
V79	Protons	7.7	2.0
V79	Protons	10.1	2.1
V79	Protons	10.8	2.4
V79	Protons	17.8	2.6
V79	Protons	19.1	2.9
V79	Protons	27.6	3.2
V79	Protons	30.4	3.1
V79	He-ions	20	2.5
V79	He-ions	28	3.2
V79	He-ions	50	4.7
V79	He-ions	70	5.7
V79	He-ions	90	6.6
V79	He-ions	120	8.0
V79	C-ions	13	2.0
V79	C-ions	24	2.0
V79	C-ions	40	2.8
V79	C-ions	50	3.1
V79	C-ions	75	4.0
AG	γ-rays		2.4
AG	X-rays		3.8
AG	Protons	1.1	4.6
AG	Protons	2.5	5.2
AG	Protons	4.0	5.4
AG	Protons	7.0	6.7
AG	Protons	11.9	7.9
AG	Protons	18.0	10.1
AG	He-ions	16.2	2.7
AG	He-ions	132	15.9
AG	C-ions	48.8	5.4
AG	C-ions	76.3	6.1
AG	C-ions	108	8.2
AG	C-ions	147.6	11.3
AG	Fe-ions	200	8.5
AG	Fe-ions	300	8.6
AG	Fe-ions	500	7.6

Table 3.1: Values of the CL yields used as input for the BIANCA code in order to reproduce survival curves by different radiation types and energies. The considered cell lines are V79 hamster fibroblasts and AG1522 or AG01522 human fibroblasts (simply denoted as AG).

3.3 The BIANCA II version

In this section, the current version of the model, called BIANCA II and entirely developed within this work, will be presented. Some shortcomings of the BIANCA model were addressed in this version through some changes in the assumptions and parameters. Moreover few technical improvements were performed.

3.3.1 Description of the model

One of the problems of the BIANCA model version was related to the threshold distance d. A good agreement with the experimental data was obtained setting the value of this adjustable parameter to 5 μm for both hamster and human normal fibroblasts. However this value appears to be too large if compared with some experimental evidences; for instance, 1–2 μm DSB migration distances have been estimated for MCF10A human epithelial cells [128]. Furthermore, basing on the idea that repair mainly takes place in small channels separating adjacent chromosome domains [148], in BIANCA II we assumed that a single Cluster Lesion can travel a maximum distance similar to the "radius" of the hit chromosome territory; this lenght was found to be consistent with the distances found by Neumaier et al. Therefore in BIANCA II we continue using a step-like distance dependence, to take into account the existence in the cell nucleus of repair centers where DSBs should migrate for repair. However the value of d was set equal to the mean distance between two adjacent chromosome territories, instead of being considered as an adjustable parameter like in BIANCA. Technically, the mass center coordinates of all chromosomes were computed as follows

$$\begin{aligned} \bar{x} &= \frac{1}{N}\sum_{i=1}^{N} x(i) \\ \bar{y} &= \frac{1}{N}\sum_{i=1}^{N} y(i) \\ \bar{z} &= \frac{1}{N}\sum_{i=1}^{N} z(i) \end{aligned} \tag{3.6}$$

where N is the number of voxels constituting a specific chromosome territory, and i is an index running over all voxels. The distances between all the pairs of mass centers belonging to adjacent chromosomes were then computed and averaged. The mean distance obtained in this way was finally the value assigned to d. Since human fibroblasts have a volume that is only slightly smaller than hamster fibroblasts, but a significantly higher number of chromosomes, the latter cell line is expected to be characterized by a larger value of d. In particular, for the representative cells used in the simulations, d was found to have a value of 3 μm for AG human fibroblasts and 3.6 μm for V79 hamster

cells. It is important to point out that in BIANCA II the threshold distance d is fixed *a priori* on the basis of the cell geometry, and it is not an adjustable parameter anymore.

Another problem of the BIANCA model was related to the overestimation of the survival level at low doses. In that version, a chromosome fragment having at least one potential partner for rejoining (that is, at least another fragment within the threshold distance d) was assumed to undergo rejoining with 100% probability. This led to a situation in which an isolated CL (that is, without another CL within d) could not cause chromosome aberrations, since eu-rejoining would be the only possible outcome. Especially at low doses, this issue could cause an overestimation of the survival level. In BIANCA II a more realistic scenario was considered in which a chromosome fragment, even if one or more potential "partners" are available within d, has a probability f of remaining un-rejoined. This assumption is consistent with studies indicating that a certain fraction of exchange-type chromosome aberrations are "incomplete", i.e. not all the involved chromosome fragments are finally rejoined [149] [150] [151]. The observed probability of unrejoining tends to be cell-line-dependent, since in general radiosensitive cells show higher frequencies of deletions with respect to normal or radioresistant cells. For instance, in ataxia-telangiectasia (A-T) cells exposed to X-rays, the fraction of un-rejoined breaks was five to six times higher than that for normal fibroblasts [152]. Concerning a possible dependence on radiation quality, contradicting results can be found in the literature. Thus, for the sake of simplicity, in the BIANCA II model version we assumed that the value of f was cell-line-dependent but LET-independent [153]. Every cell line should be therefore characterized by a different f value, fixed through the comparison with experimental data, as illustrated in the next Section for the two reference cell lines considered in this work. For BIANCA II f is thus the second -and last- adjustable parameter. In conclusion, in BIANCA II some changes were introduced concerning the biophysical assumptions, but the adjustable parameters are still only two.

Finally, in BIANCA II the way to treat the CLs falling into "empty" voxels was changed. In particular, instead of re-positioning the lesion in a different voxel, the CL is now assigned to the closest chromosome (which is identified by calculating the distance from the chromosome mass center); the chromosome arm is then chosen like in the BIANCA version. In this way, the CLs can be distributed in the whole nucleus volume, avoiding to introduce a geometrical bias. The testing of the BIANCA II version against experimental data, mainly based on the comparison with chromosome aberration yields, will be illustrated in the next Section, while the main results obtained with this version will be the topic of Chapter 4.

3.3.2 Simulation of chromosome aberration yields

The testing of the BIANCA II model version was mainly focused on the comparison between simulations and experimental data on chromosome aberra-

tions, both for V79 hamster fibroblasts and for AG1522 human fibroblasts. In fact, although the final goal is the evaluation of cell survival, according to our approach this endpoint is strictly related to lethal chromosome aberrations. In particular, the first considered data set was that of the already mentioned experiment by Cornforth and Bedford [40] on AG1522 cells exposed to X-rays [153]. Figure 3.8 shows dose–response curves for different aberration types: dicentrics, rings, and deletions (both separately and summed up to give "total aberrations"). The lines are simulation outcomes while the points are experimental data. The error bars associated with the experimental points represent 95% confidence about means as reported in [40]. Error bars for ring aberrations are not reported in the plots of the original paper, but we calculated them by assuming Poisson statistics, that is

$$\varepsilon_{2\sigma} = 2\sqrt{\frac{n_r}{N_c}} \tag{3.7}$$

where $\varepsilon_{2\sigma}$ is the error at 2σ confidence level, n_r is the number of scored rings and N_c is the number of observed cells. This is the same procedure followed by the authors of the experimental work to calculate error bars for the other aberration types.

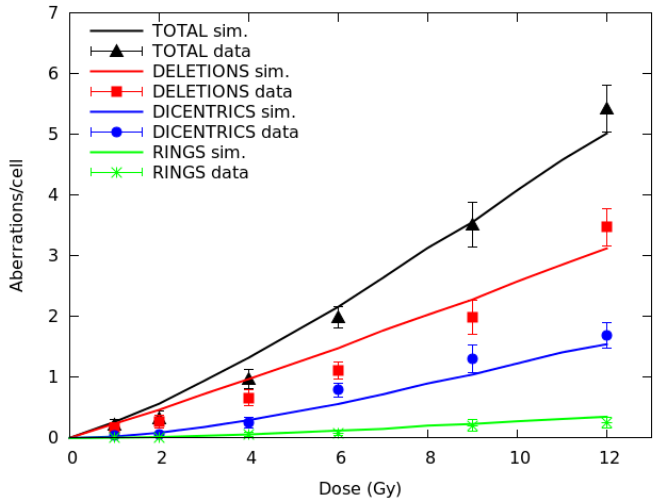

Figure 3.8: Yields (mean number per cell) of different aberration types (dicentrics, rings and deletions, as well as total aberrations) in AG1522 primary normal human fibroblasts exposed to different doses of X-rays. The lines are simulation outcomes, the points are experimental data taken from [40]. Figure modified from [153].

Both for dicentrics and rings, the simulated aberration yields are within the experimental errors, with the only exception of dicentrics at 6 Gy. The capability of reproducing separately the yields of dicentrics and rings supported the assumption adopted in BIANCA II for d, since we found that higher d

values tend to overestimate the ratio of dicentrics to rings (the so-called "F-ratio"), and viceversa. Concerning deletions, the simulated response is basically linear, while the experimental response shows a non-negligible quadratic component. This can be explained considering that in the simulations most deletions were "terminal deletions", which being due to a single chromosome break involve a single-particle mechanism proportional to dose, whereas according to the authors most experimental deletions were of the "interstitial" type, which requiring two chromosome breaks (also) involves a two-particle mechanism proportional to the square of dose. However the general trend of a clear prevalence of deletions compared to dicentrics is in agreement with the data.

The curves reported in Figure 1 were obtained with a f value of 0.18, and a CL yield of $\sim$1.3 CLs$\cdot$Gy$^{-1}\cdot$cell^{-1}. This value is lower than the value used with the BIANCA version (where $f = 0$); in fact, by increasing f, the yield of deletions, and thus of total aberrations, increased, implying that a lower CL yield was sufficient to get the same yield of total aberrations. In the BIANCA version, although it was possible to reproduce the yields of total aberrations with $f = 0$ [129], at most doses the yields of deletions were underestimated by a factor $\sim$2, and the yields of dicentrics were overestimated, again by a factor $\sim$2. On the contrary, as shown in Figure 3.8, the introduction in BIANCA II of a f value higher than 0 allowed obtaining a good agreement not only with total aberrations as a whole but also with dicentrics, rings, and deletions considered separately. Through this comparison, a value for the f parameter was set; lower f values in fact led to an underestimation of deletions associated with an overestimation of dicentrics, whereas higher f values led to an overestimation of deletions associated with an underestimation of dicentrics. The value 0.18 used for f in this work was maintained fixed for any other simulation of AG1522 cells irradiation, since in BIANCA II f is considered as independent of radiation quality.

The second data set used for comparison was that of the experiment performed by Cornforth, Bailey and Goodwin in 2002 [136] on AG1522 cells exposed to alpha particles. These particles were delivered acutely, using a collimated 85-MBq ^{238}Pu source with a mean energy of 3.5 MeV and a LET of 116 keV/μm. In figure 3.9 the experimental yields of dicentrics, deletions and total lethal aberrations are reported, together with the simulation results. The error bars associated with the experimental points represent 95% confidence about means and they were calculated like in the previuos experiment. All the simulated aberration yields (at all dose levels) were within the 3σ confidence level. The shapes of curves for the various aberration types are almost linear with dose (consistent with the behaviour of high LET radiation). In order to reproduce the experimental data, the value of f was maintained fixed at 0.18 (as explained before), while the CL yield was adjusted to $\sim$6.3 CLs$\cdot$Gy$^{-1}\cdot$cell^{-1}, significantly higher than the yield used to reproduce the response to X-rays. In conclusion, the BIANCA II model version was able to reproduce pretty well

the dose-dependence of several different chromosome aberration types, for at least two different radiation qualities.

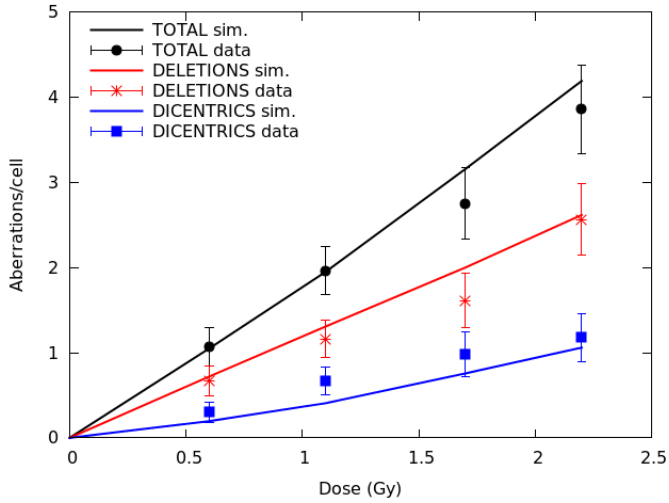

Figure 3.9: Yields (mean number per cell) of different aberration types (dicentrics, deletions and total lethal aberrations) in AG1522 primary normal human fibroblasts exposed to different doses of 116 keV/μm alpha particles. The lines are simulation outcomes, the points are experimental data taken from [136].

As a last step in the testing of the model, an experiment on V79 chromosome aberrations was also analyzed. This was also essential for adjusting a value of f for V79 cells, since every cell line should be characterized by its own value. In an experiment performed by Carrano in 1973 [39], synchronous cultures of V79 hamster cells were irradiated with 3 Gy of X-rays. The main information collected by the author were the yields of deletions, two-hit aberrations (that is dicentrics plus centric rings), total lethal aberrations and also isolated deletions (i.e. deletions in cells without two-hit aberrations). The experimental results, together with simulation outcomes, are reported in Table 3.2. The agreement is good and all the simulations are within a confidence level of 1σ, except for the yield of isolated deletions, which is within 3σ. Another important result concerns the statistical distribution of the two-hit aberrations, which is reported in the original paper; the BIANCA Monte-Carlo code allows for scoring the exact number of aberrations for each cell, and thus for a comparison with the experimental data by Carrano. The fractions of cells with 0, 1, 2 and 3 or more two-hit aberrations are reported in Table 3.3: the agreement between simulations and experimental data is really high, with a reduced Chi-Square value of $\sim$1.2. Thus by tuning only two parameters a good agreement can be found with the yields of several aberration types and even with their statistical distributions. The CL yield used to find the agreement with the data was $\sim$1.7 CLs$\cdot$Gy$^{-1}\cdot$cell^{-1}, while f was set to 0.08. This value is

smaller than the one used for human fibrobasts, consistent with the meaning of f. In fact this parameter reflects the capability of a cell of repairing critical DNA damages, and for AG1522 cells, which are more radiosensitive, a higher number of Cluster Lesions ($\sim$18% against $\sim$8% for V79 cells, according to our simulations) will not be repaired.

Data	2-hit aberrations	Deletions	Isolated deletions	Total
Exp.	0.410 $\pm$ 0.018	0.606 $\pm$ 0.022	0.370 $\pm$ 0.017	1.016 $\pm$ 0.029
Sim.	0.410	0.594	0.339	1.004

Table 3.2: Experimental and simulated yields (mean number per cell) of different aberration types (two-hit, deletions, isolated deletions and total aberrations) in V79 Chinese hamster cells exposed to a single dose (3 Gy) of X-rays. The experimental data were taken from [39]. The yield of isolated deletions was calculated as the total number of deletions in cells without two-hit aberrations divided by the total number of scored cells.

Fraction of cells	0	1	2	≥ 3
Exp.	0.652	0.282	0.061	0.005
Sim.	0.651	0.292	0.054	0.003

Table 3.3: Experimental and simulated fractions of cells with 0, 1, 2 and 3 or more two-hit aberrations in V79 Chinese hamster cells exposed to a single dose (3 Gy) of X-rays. The experimental data are taken from [39].

The two values of f obtained by these comparisons, both for AG1522 and for V79 cells, were changed for irradiations with other radiation qualities, and were used as input parameters for the simulation of cell curvival curves by different ion species, as illustrated in Chapter 4. The results were used in particular for applications in the field of hadrontherapy.

Chapter 4

Results - Part II: model applications

In Chapter 3 the structures of the different model versions were described, as well as their assumptions and parameters and the first comparisons with experimental data. In the present Chapter the main results of both the BIANCA and the BIANCA II versions, entirely obtained within this thesis work, will be illustrated. In particular with BIANCA a study on the characterization of the DNA Cluster Lesions (that is the critical DNA damage for chromosome aberrations and cell death) was performed. With BIANCA II on the contrary the attention was mainly focused on possible applications for hadrontherapy. The effectiveness variation along a protontherapy beam was evaluated and the effectiveness dependence on LET for Carbon ions was investigated. Other studies, such has an investigation on a helium ion microbeam and on the statistical distributions of chromosome aberrations, were also carried out. Finally a possible improvement to make the model more predictive was introduced.

4.1 Characterization of DNA Cluster Lesions with BIANCA

As mentioned in Section 1.2.1, clusters of DNA DSBs can undermine local chromatin stability generating small DNA fragments, the loss of which is likely to impair the function of all DSB repair pathways and to lead to cell death and other endpoints including chromosome aberrations [154]. However, the spatial dimensions of these clusters, which can be quantified in terms of number of base-pairs, still need to be elucidated. Many theoretical studies based on radiation track-structure simulations focused the attention on DSB^{++} (at least two SSBs on each strand within 30 base-pairs) and other types of local DNA cluster damage [155] [156] [157] [115] [158] [159]. Experimentally, DNA fragments smaller than 70 bp were suggested to be implicated in the enhanced cell killing

observed after high LET irradiation by Wang et al. [160]; a role for larger fragments was suggested by Rydberg and co-workers basing on both experiments and simulations [34] [161] [162] [163] (see Section 1.2.1). The authors concluded that, in addition to local clustering, also a clustering at the chromatin fiber level, which they called "regional clustering", may be important. Other authors [164] [165] proposed that the spatial distribution of DSBs in looped chromatin domains at the Mbp level plays a crucial role in DSB repair and that mis-repair involves DNA fragment loss at such DSB clusters. The importance of this damage scale was also suggested in some modeling studies [166] [48].

Thanks to the BIANCA model simulations, we attempted to provide a characterization for such critical DNA damage, which is represented by the Cluster Lesion (CL) parameter of the model. Yields of CLs were thus compared with experimental or theoretical yields of DNA fragments of different sizes taken from the literature, focusing on the ∼bp scale ("local clustering", related to the double helix), the ∼kbp scale ("regional clustering", related to the chromatin fiber) and the ∼Mbp scale (related to chromatin fiber loops). To this purpose the CL yields used for all the simulations reported in Section 3.2.3 were considered [141]. This allowed us to have a large set of data regarding the irradiation of two cell lines of different radiosensitivity by different ion species covering a wide range of LET values.

The yields (average number per Gy and per cell) of cluster lesions used to obtain the various survival curves reported in Section 3.2.3 are shown in Figure 4.1 as a function of the particle type and LET. With the exception of very high LET values, the CL yield for a given particle type was found to increase with LET for both cell lines (AG human fibroblasts and V79 hamster fibroblasts); furthermore, lighter particles were more effective than heavier particles having the same LET (as in the case of He ions compared to protons). Both these features are consistent with the hypothesized clustering nature of such lesions, since DNA cluster damage is known to show this kind of dependence on radiation quality [115] [46]. The particle and LET dependence shown by CLs reflects the dependence shown by cell survival, for which the RBE is characterized by a peak around 100–200 keV/μm.

Concerning higher LET values, where the effectiveness in cell killing is known to decrease, the effectiveness in DNA (cluster) damage is still an open question. An increase also at very high LET has been found for DSB^{++}, whereas a maximum has been found around 300 keV/μm for DSB^{+} [159] and around 400 keV/μm for fragments in the size range 0.1–2 kbp [34]. On the contrary, the trend of a "mixture" of different types of complex DSBs (defined as a weighted sum of DSB, DSB^{+} and DSB^{++} in a 18-kbp chromatin fiber stick), has been found in good agreement with cell survival RBE [167], while a much smoother trend has been observed for fragments in the Mbp range, with only a slight decrease above 200-300 keV/μm [168] [35] (see also Section 1.2.1). Concerning the differences between the two cell lines considered in this

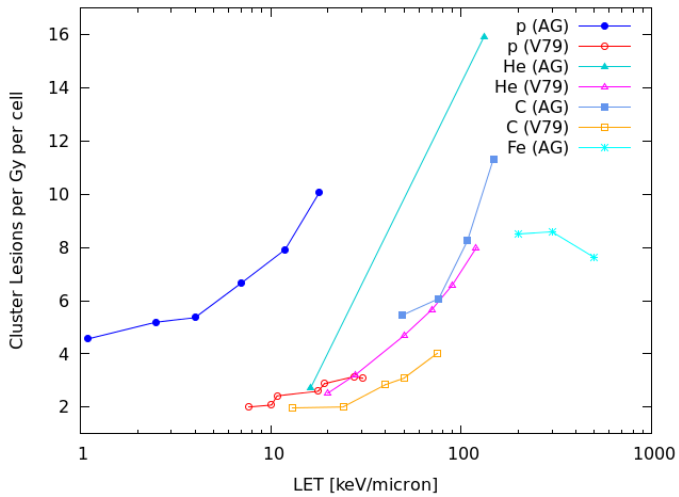

Figure 4.1: Yields of cluster lesions used in the simulations to obtain the various survival curves reported in Section 3.2.3. The lines are simply guides for the eye, whereas the points represent CL yields induced by protons (circles), He ions (triangles), C ions (squares) and Fe ions (asterisks). Empty symbols refer to V79 cells, full symbols and asterisks refer to AG1522 cells. Figure modified from [141]

thesis work for a given particle type and LET, the lower CL yields for hamster fibroblasts reflect the lower radiosensitivity of these cells with respect to human fibroblasts. In fact cluster lesions represent those DNA lesions that are severe and thus difficult to be repaired: while severity depends on radiation quality, the difficulty in repair depends on the specific cell repair machinery.

After this qualitative analisys of the CL trend as a function of LET, the CL yields were compared with yields of DNA fragments taken from experimental or theoretical works available in the literature, with the aim of finding a characterization for these lesions. The comparison was focused on three fragment size scales:

- the base-pair (bp) scale (the scale of the so-called DSB^{++})
- the kbp scale, which is related to nucleosome packing in the chromatin fiber
- the Mbp scale, which is related to interphase chromatin organization in loops

Figure 4.2 reports the CL yields shown in Figure 4.1 for AG1522 cells compared with yields of DSB^{++} calculated by PARTRAC Monte Carlo simulations [35] [159]. With respect to DSB^{++}, CLs increased with LET much less rapidly, showing in general higher values at low LET and lower values at high LET.

Furthermore, while DSB^{++} continued to increase also at very high LET, CLs showed a (slight) decrease after 300–400 keV/μm.

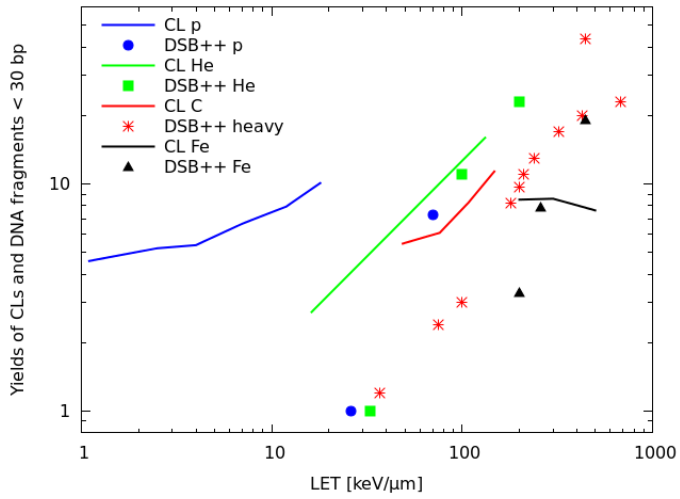

Figure 4.2: Comparison between the CL yields for AG1522 cells (blue line for protons, green line for He ions, red line for C ions and black line for Fe ions) and calculated yields of DSB^{++} taken from [35] and [159] induced by protons (blue), He ions (green), Fe ions (black) and other heavy ions (red), that is: B of 37 and 180 keV/μm; N of 75 and 320 keV/μm; Ne of 210 and 680 keV/μm; O of 430 keV/μm; C of 100, 201, 240 and 442 keV/μm. Figure modified from [141]

In Figure 4.3, the CL yields for AG cells are compared with experimental or theoretical yields of DNA fragments with size at the kbp scale. The following fragment data were considered: experimentally-detected fragments with size in the range 1–9 kbp induced by gamma rays and 28.5 keV/μm protons (Tabocchini et al., personal communication of data based on the Constant Field Gel Electrophoresis technique described in [169]); experimentally-detected fragments with size in the range 0.1–9 kbp induced by alpha particles of increasing LET in the range 67–120 keV/μm [163]; fragments calculated by the PARTRACK code with size in the range 1–9 kbp induced by the following radiation types: 100 keV/μm alpha particles, C ions of 13.8, 201, 240 and 442 keV/μm and Fe ions of 201, 260 and 442 keV/μm [35]. The irradiated cell line is the AG1522 line, with the exception of the data taken from Rydberg et al. that are for GM98 (still normal human fibroblasts). The particle and LET dependence shown by cluster lesions was rather similar to the dependence shown by these kbp fragments, suggesting that such fragments may play an important role in the induction of cell death and possibly other endpoints such as chromosome aberrations. This is in line with the idea that endpoints like chromosome aberrations and cell death require the disruption of the chromatin fiber continuity, which is very likely following DSB clusters, but much

less likely following less complex DSBs [25] [154]. An analogous conclusion has been drawn by means of Monte Carlo simulations by Friedland et al. [167], who found that regional DNA damage clusters (within a 18-kbp chromatin fiber stick) were in closer correlation to cell inactivation experimental data with respect to local clusters. Moreover Rydberg et al [162], referring to clustering at the chromatin fiber level, stated that "if these clusters are important for cell killing, a possible hypothesis could involve chromatin fiber breakage at sites of clusters and a high probability of forming chromosomal aberrations".

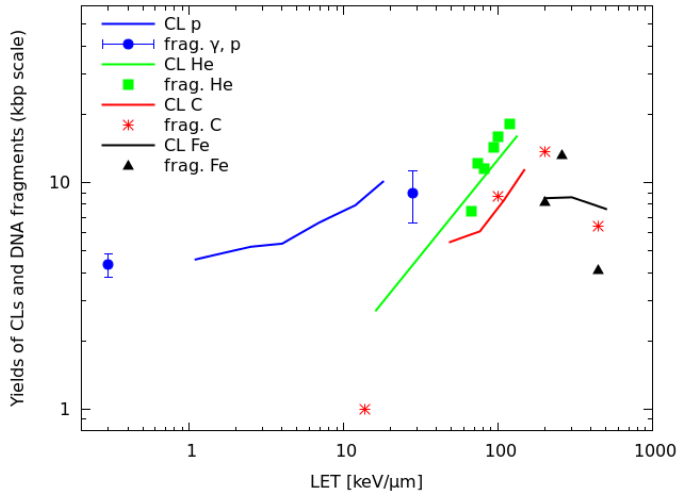

Figure 4.3: Comparison between the CL yields for AG1522 cells (blue line for protons, green line for He ions, red line for C ions and black line for Fe ions) and experimental or theoretical yields of kbp size DNA fragments taken from the literature ([163] and Tabocchini et al., personal communication, for the experimental yields; [35] for the theoretical yields) induced by γ-rays or protons (blue), He ions (green), C ions (red) and Fe ions (black). A LET value of 0.3 keV/μm was assigned to γ-rays [18]. Figure modified from [141]

In Figure 4.4, the CL yields for AG cells are compared with theoretical yields of DNA fragments with size in the range 0.023–1 Mbp calculated by PARTRAC Monte Carlo simulations [35], as well as experimental yields of DNA fragments with size in the range 0.005–1.1 Mbp taken from Hoglund et al. [168]. The latter has been obtained applying pulsed-field gel electrophoresis and fragment analysis to normal human skin fibroblasts (GM 5758) exposed to ^{60}Co γ-rays, 40 keV/μm He ions and N ions of 80, 125, 175 and 225 keV/μm. Quantitatively, the yields taken from the experimental work (empty symbols and crosses) were higher than those deriving from PARTRAC simulations (full symbols and asterisks). This may depend on the fact that the experimental data has been obtained at much higher doses (in the range 30–200 Gy) with respect to the simulations, which have been performed at 5 Gy. However, both data sets showed only a slight increase in the yield of these fragments in the

region of intermediate-to-high LET; cluster lesions, on the contrary, showed a steep increase. A similar behavior has been suggested by Lobrich et al. [170], who measured the size distribution of DNA fragments in GM38 normal human fibroblasts exposed to X-rays, 97 keV/μm N ions and 150 keV/μm Fe ions, covering a total range between 0.1 kbp and 10 Mbp.

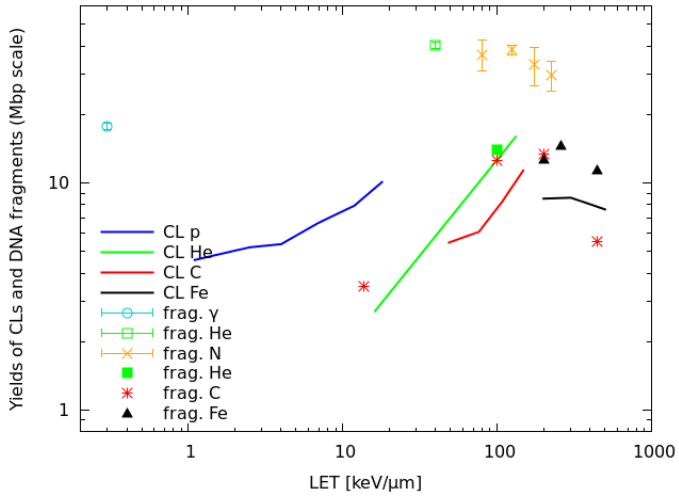

Figure 4.4: Comparison between the CL yields AG1522 cells (blue line for protons, green line for He ions, red line for C ions and black line for Fe ions) and theoretical yields of DNA fragments with size in the range 0.023–1 Mbp induced by He ions (full square), C ions (asterisks) or Fe ions (triangles) taken from [35], as well as experimental yields of DNA fragments with size in the range 0.005–1 Mbp induced by γ-rays (circle), 40 keV/μm He ions (empty square) and N ions of 80, 125, 175 and 225 keV/μm (crosses) taken from [168]. Figure modified from [141]

Clearly it is also possible that two or more classes of DNA cluster damage play a role, although probably with different "weights". An interesting attempt in this sense has been performed by Friedland et al. [167], who found good agreement between experimental RBE for cell inactivation and calculated RBE for a weighted sum of three different DSB classes (DSB, DSB^{+} and DSB^{++}), especially for the case of regional clustering within a 18-kbp chromatin fiber stick. However, according to our simulations, CLs showed a better agreement with kbp size fragments rather than DSB^{++} or Mbp size fragments, suggesting an important role for the disruption of the chromatin fiber continuity at inducing cell death and chromosome aberrations.

4.2 Applications of BIANCA II for hadrontherapy

After applying the BIANCA model to cell survival, the BIANCA II version was developed and used in particular for hadrontherapy applications. As mentioned in the previous Chapters, protons are usually considered low-LET radiation, and a constant relative biological effectiveness (RBE) of 1.1 is generally applied in clinical practice. However, both *in vitro* and *in vivo* studies indicate that proton effectiveness increases with decreasing energy, that is increasing LET. This implies an increase of effectiveness with depth along the SOBP, as well as an extension of the biological effective range. *In vivo*, the average RBE at mid-SOBP is ∼1.1, ranging from 0.7 to 1.6 [103]; *in vitro* data on clonogenic cell survival indicate an average value at mid-SOBP of ∼1.2, ranging from 0.9 to 2.1 [103]. Furthermore, the RBE depends not only on the particle energy but also on many other factors, such as

- dose level: this could introduce discrepancies in treatments with a different number of fractions (and thus with a different dose per fraction);
- cell type: tissues characterized by a different radiosensitivity may have different responses;
- biological endpoint: although the main endpoint of interest for tumor cells is cell death, other endpoints (e.g., mutations, non-lethal chromosome aberrations, etc.) may be relevant for normal tissues.

Although clinical results do not indicate that the use of a constant RBE is incorrect, no trials specifically investigated RBE variations. Applying a constant RBE of 1.1 may lead to an underestimation of the damage to normal tissues, especially for treatments involving organs at risk just beyond the tumor, such as the retina for eye tumors and the heart for (left) breast tumors, which are becoming a major application of protontherapy [171]. On the other side, the currently available RBE data might be insufficient to support a change in clinical practice [104]. Incorporating variations in biological effectiveness without directly considering the RBE may be an alternative strategy.

Since BIANCA II does not make direct use of experimental RBE values, the first model application to hadrontherapy consisted of the evaluation of the biological effectiveness variation along a therapeutic proton SOBP [153]. In addition to the dependence on depth (that is on LET), we also investigated the dependence on the three factors mentioned above, that is: dose level, cell line radiosensitivity and biological endpoint. The model was applied to the 62-MeV proton beam used to treat ocular melanoma at the CATANA facility of INFN-LNS in Catania, Italy (see Section 2.3.2). Experimental survival curves taken from the literature [45] for AG01522 cells exposed to pristine peaks and SOBPs from the CATANA beam were reproduced, and cell death and

chromosome aberrations were calculated for different depth positions along a SOBP. The depth-dose profile was the same used by Chaudhary et al. and it is reported in Figure 4.5, both for the monoenergetic and the Spread-Out case. Finally, cell death and chromosome aberrations were predicted for V79 cells exposed to the same dose profile.

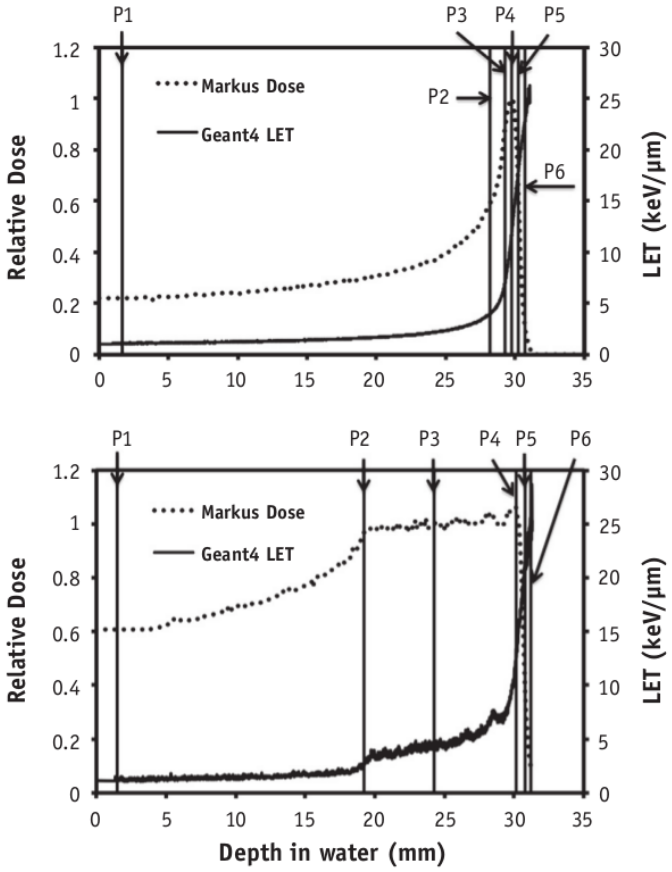

Figure 4.5: Dose (dashed lines) and LET (solid lines) profiles for 62-MeV monoenergetic (top) and modulated (bottom) proton beam configurations. P1-P6 indicate the positions of cell irradiations. Figure taken from [45].

4.2.1 Reproduction of proton survival curves

The first step of this study consisted of reproducing experimental survival curves obtained with the 62-MeV CATANA beam by Chaudhary et al. [45]. In that experiment, AG01522 primary normal human fibroblasts were exposed to six positions along a pristine Bragg peak (water-equivalent depths: 1.69, 28.21, 29.28, 29.76, 30.24 and 30.72 mm) and at six positions along a SOBP (water-equivalent depths: 1.52, 19.22, 24.28, 30.14, 30.82, 31.22 mm). After irradiation, the cells were immediately trypsinized, counted, seeded, and incu-

bated to allow for macroscopic colony formation; colonies consisting of at least 50 cells were scored as viable.

Figure 4.6 reports simulated survival curves for the six positions along the pristine peak (corresponding to the following LET values: 1.1, 4.0, 7.0, 11.9, 18.0, and 22.6 keV/μm), together with the experimental data for comparison and their error bars, which represent one Standard Deviation. All simulations were performed adopting the same value of the chromosome fragment unrejoining parameter f used to calculate chromosome aberrations in AG human fibroblasts, which was 0.18 (see Section 3.3.2). The yields of CLs, which depend on radiation quality, were adjusted separately for each curve; they ranged between ∼4.1 and ∼8.0 CLs·Gy^{-1}·cell^{-1}, increasing with the radiation LET. Also the X-ray reference curve of the experiment was reproduced, with 3.3 CLs·Gy^{-1}·cell^{-1} as input. Despite the general agreement with the experimental data, in some cases, typically for curves corresponding to the highest considered LET values, there was a tendency to underestimate the experimental survival at the highest considered dose, which was 3 Gy. A statistical analysis was performed in order to evaluate this discrepancy. For 1.1 and 4.0 keV/μm the value of the reduced chi-square was around 1. Higher values were found for the other four curves, mainly due to the point at 3 Gy. However, at least in two cases (7.0 and 22.6 keV/μm), the simulations were close to the fit performed by the authors, since the relative difference between calculated and fitted survival was smaller than 20%.

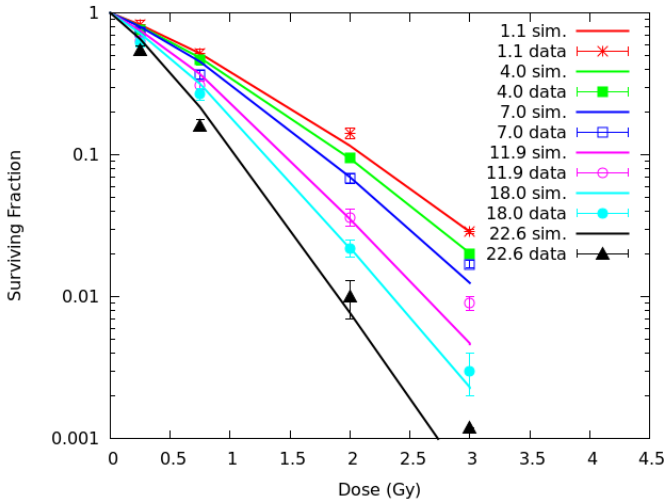

Figure 4.6: Cell survival curves for AG01522 primary normal human fibroblasts exposed at six depth positions along a pristine proton Bragg peak(corresponding to the following LET values: 1.1, 4.0, 7.0, 11.9, 18.0, and 22.6 keV/μm). The lines are simulation outcomes, the points are experimental data taken from [45]. Figure modified from [153].

Figure 4.7 reports simulated survival curves and experimental points for the

six positions along the modulated Bragg peak, corresponding to the following dose-averaged LET values: 1.2, 2.6, 4.5, 13.4, 21.7, and 25.9 keV/μm. The value of f was maintained fixed at 0.18, while the CL yield was adjusted separately for each curve, ranging between ~3.7 and ~6.4 CLs·Gy^{-1}·cell^{-1}. An underestimation of the experimental survival at high doses was found also in this case, especially for the highest considered LET values. The agreement between simulations and experiments was particularly good for the lower LET curves, since a reduced chi-square around 1 was obtained for 1.2, 2.6, and 4.5 keV/μm. Higher (reduced) chi-square values were found for 13.4, 21.7, and 25.9 keV/μm, mainly due to the points at the highest doses (3 and 4 Gy). However, with the only exception of the point at 3 Gy for the 21.7 keV/μm curve, the relative difference between calculated and fitted survival was not larger than 20%. It is also worth mentioning that, since the highest LET values refer to the descending part of the SOBP, where the doses are lower, the calculations of the effectiveness at high doses of the highest LET values were not used for the predictions of cell killing and chromosome aberrations along the SOBP dose profile, which will be illustrated in the next Section.

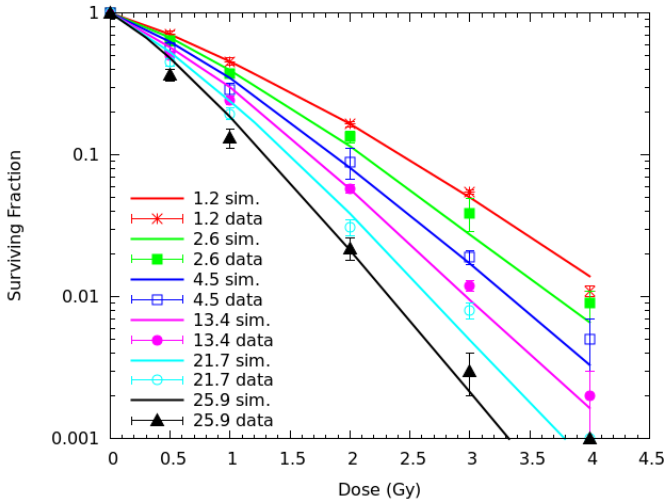

Figure 4.7: Cell survival curves for AG01522 primary normal human fibroblasts exposed at six depth positions along a proton SOBP (corresponding to the following dose-averaged LET values: 1.2, 2.6, 4.5, 13.4, 21.7, and 25.9 keV/μm). The lines are simulation outcomes, the points are experimental data taken from [45]. Figure modified from [153].

Interestingly, the CL yields used for the curves reported in Figure 4.7 were lower than the CL yields used for the pristine peaks of Figure 4.6. This is consistent with the higher RBE observed in the experimental work for the pristine peaks with respect to the SOBP. This systematic deviation is probably related to the averaging procedures in the presence of a LET distribution along the SOBP, as discussed for carbon beams by Belli et al. [172].

The simulated cell surviving fraction and chromosome aberrations at different dose levels for AG cells were used for the study illustrated in the next Section. An analogous analysis was performed on V79 cells, which are rather radioresistant and are widely used in the characterization of hadrontherapy beams. The final goal consisted of predicting cell death and chromosome aberrations for V79 cells along the SOBP dose profile used in [45] to irradiate AG01522 cells (as well as U87 cells, which however were not considered in our work). As a preliminary step, to adjust the model parameters before performing such predictions, experimental survival curves taken from the literature for V79 cells exposed to different monoenergetic proton beams, as well as X-rays as a reference [46] [142], were reproduced.

Figure 4.8 reports calculated survival curves for X-rays and four monoenergetic proton beams (with LET values: 7.7, 11.0, 17.8, 27.6 keV/μm), together with experimental data; all the curves were obtained adopting the same value of f used to calculate chromosome aberrations in V79 cells, which is 0.08 (see Section 3.3.2). The CL yield was adjusted separately for each curve; the X-ray curve was obtained using a CL yield of 1.5 CLs·Gy^{-1}·cell^{-1}, whereas the four proton curves were obtained with CL yields in the range $\sim$2.0–3.2 CLs·Gy^{-1}·cell^{-1}, increasing with LET. For the curve at the lowest LET (7.7 keV/μm), the value of the reduced chi-square was 1.8. Higher (reduced) chi-square values (around 3-4) were found for the other curves. However only the points at 0.6 Gy and 6 Gy of the curve at the highest LET (27.6 keV/μm) showed a displacement larger than 3σ compared to the experimental points. The CL yields for V79 cells were lower than the CL yields for AG01522 cells exposed to similar radiation qualities, as a consequence of the lower radiosensitivity of V79 cells. In fact, although the CL yield mainly depends on radiation quality, it is also modulated by the specific target cell response. This is consistent with the biophysical meaning of this parameter, which represents a type of DNA damage that is severe and difficult to be repaired.

4.2.2 Depth-dose profiles

After reproducing the survival curves for both AG and V79 cells, the model was applied to investigate the depth- and dose- dependence of the beam effectiveness along the CATANA proton SOBP, in terms of both cell death and chromosome aberrations, starting from human fibroblasts. For different depths in water of the SOBP dose profile of Figure 4.5, Figures 4.9 and 4.10 report the calculated relative fraction of inactivated cells and the calculated relative yield of dicentrics, assuming a dose of 2 Gy in the plateau region. The term "relative" means that each quantity was normalized with respect to the proximal point.

For the six depth positions considered in [45], the cell killing calculations did not add substantial information with respect to the experimental work. However, the model allowed predicting the fraction of surviving cells also for other positions, with focus on the dose fall-off region that can be critical for

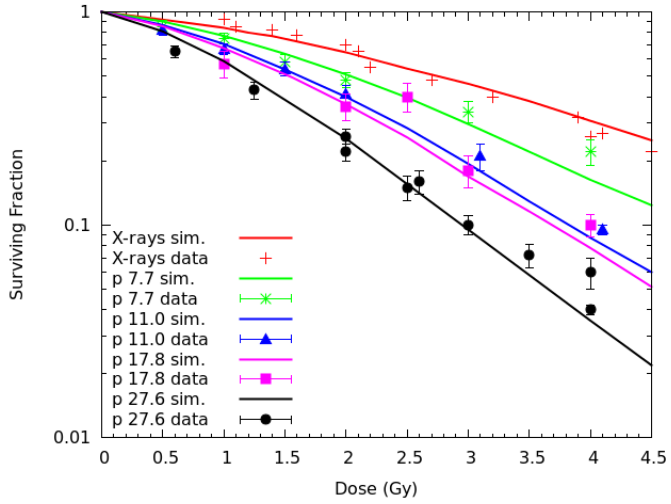

Figure 4.8: Survival curves for V79 cells exposed to four monoenergetic proton beams (LET: 7.7, 11.0, 17.8, and 27.6 keV/μm), as well as X-rays as a reference. The lines are simulation outcomes, the points are experimental data taken from the literature: [46] for X-rays, 7.7 keV/μm protons and 11.0 keV/μm protons; [142] for X-rays, 17.8 keV/μm protons and 27.6 keV/μm protons. Figure modified from [153].

normal tissue damage (see Figure 4.10). These calculations were performed considering two points, for which the information was available from the experiments, linearly interpolating the CL yields and using the resulting yield as input for a simulation at the intermediate depth at the right dose level. Moreover, the model provided predictions of chromosome aberrations, which were not investigated in the experimental work [45]. This information may be useful in the framework of normal tissue damage evaluation, since certain types of chromosome aberrations (typically, some reciprocal translocations) are known to be related to cell conversion to malignancy [38]. For this reason, dicentric yields were shown in Figures 4.9 and 4.10: they are thought to be not significantly different than the yields of reciprocal translocations, which are the symmetrical counterpart of dicentrics among inter-chromosomal simple exchanges (see Section 1.2.2).

The beam effectiveness, for both cell death and chromosome aberrations, was found to increase with depth along the plateau, and high levels of biological damage were also found beyond the distal fall-off. For instance at $\sim$31 mm in water, where the physical dose was about 40% of the proximal dose, the fraction of inactivated cells was almost 80% of the fraction of inactivated cells at the proximal position. The (relative) increase in chromosome aberrations with increasing depth along the plateau was more pronounced with respect to cell killing: while cell killing increased by a factor $\sim$1.1, the yield of dicentrics (and, thus, reciprocal translocations) in the distal position was more than 1.4

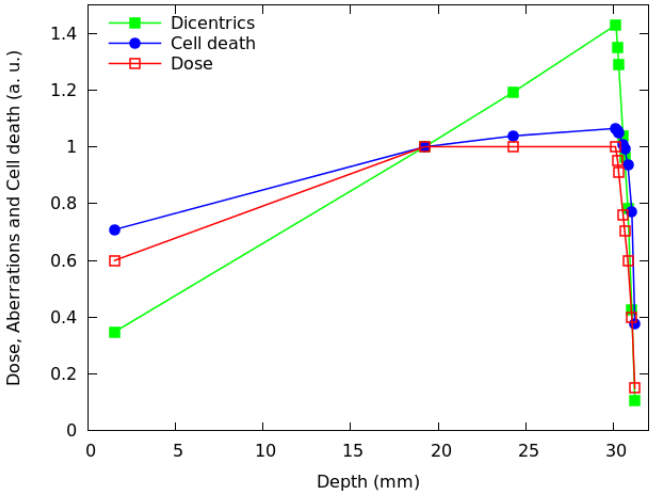

Figure 4.9: Calculated fraction of inactivated cells (blue symbols) and calculated mean number of dicentrics per cell (green symbols) at different depths of the SOBP dose profile reported in Figure 4.5, which is also shown in the figure (red symbols). Each quantity was normalized with respect to the proximal position. The lines are simply guides for the eye [153].

times higher with respect to the proximal position. This is an example of dependence of biological effectiveness on the considered endpoint.

Predictions of cell death and chromosome aberrations were also performed assuming different plateau doses. Figures 4.11 and 4.12 report predictions for the fraction of inactivated cells (Figure 4.11) and the mean number of dicentrics per cell (Figure 4.12) at different depths of the SOBP, assuming a plateau dose of 1 or 4 Gy. For comparison, the Figures also report the results for 2 Gy. Again, the results were normalized with respect to the proximal position. Increasing the physical dose (from 2 to 4 Gy) reduced the increase in biological effectiveness along the plateau, whereas decreasing the dose (from 2 to 1 Gy) led to an even more pronounced increase in effectiveness. This is consistent with the well-known dose-dependence of RBE, which tends to be higher at lower doses and vice-versa (see Section 1.2.4). The non-constant proton RBE therefore may have less relevance for hypofractionated treatments. However, while for cell death the highest considered dose (4 Gy) led to an almost flat biological effectiveness along the plateau, for chromosome aberrations even that dose implied an increase in effectiveness.

To compare the effectiveness of protons with that of X-rays, the ratio between the level of effect (cell death or chromosome aberrations) induced by a given dose of protons and the level of effect induced by the same dose of X-rays was also investigated for different positions along the SOBP dose profile. Although this quantity has not the same meaning as the RBE, which is defined as the iso-effect ratio between X-ray dose and proton dose, both

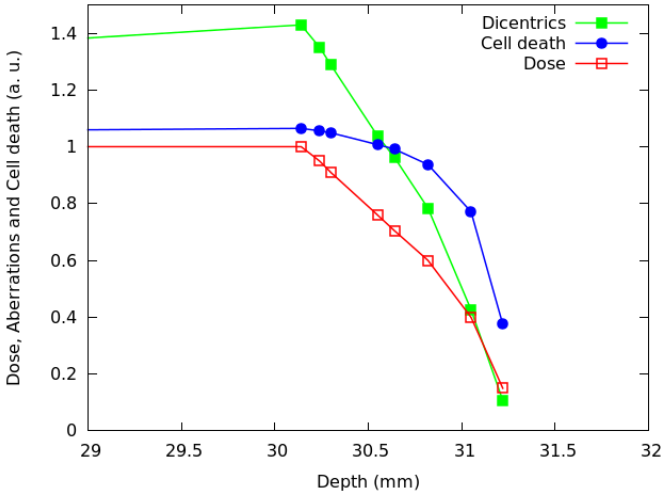

Figure 4.10: Distal and fall-off region of the SOBP shown in Figure 4.9 [153].

these ratios reflect variations in biological effectiveness. Figure 4.13 reports, for different depths along the SOBP dose profile assuming a plateau dose of 2 Gy, the calculated ratio between proton-induced cell death (i.e., fraction of inactivated cells) and cell death induced by the same dose of X-rays. This ratio will be called R_I, where "I" means "inactivation." The figure also reports the ratio between the yield of lethal aberrations (i.e., mean number of dicentrics plus rings plus deletions per cell) induced by protons and the yield of lethal aberrations induced by the same dose of X-rays, which will be called R_{LA}, as well as the ratio between the yield of dicentrics induced by protons and the yield of dicentrics induced by the same dose of X-rays, which will be called R_{DIC}.

All these ratios increased with depth due to the increase in proton LET. However, their depth dependence showed different features. In particular, R_{DIC} (ratio between proton- and X-ray dicentrics) increased up to more than 3.5, whereas R_{LA} (ratio between proton- and X-ray lethal aberrations) and R_I (ratio between proton- and X-ray cell inactivation) increased up to about 2. Again, this is an example of different effectiveness when different endpoints – even different types of chromosome aberrations – are considered. The fact that dicentrics, considered as representative of reciprocal translocations, showed a more pronounced increase with respect to lethal aberrations and cell death may have implications in the evaluation of the risk to normal tissues.

In Figure 4.14, the same quantities reported in Figure 4.13, that is R_I, R_{LA} and R_{DIC}, are plotted as a function of the (dose-averaged) LET, rather than as a function of depth. With the exception of the two points at the lowest LET, this revealed a basically linear increase of R_{LA} with LET. Therefore, at least for LET values in the range ~5–25 keV/μm, additional R_{LA} values (where "additional" means in correspondence of additional LET values and,

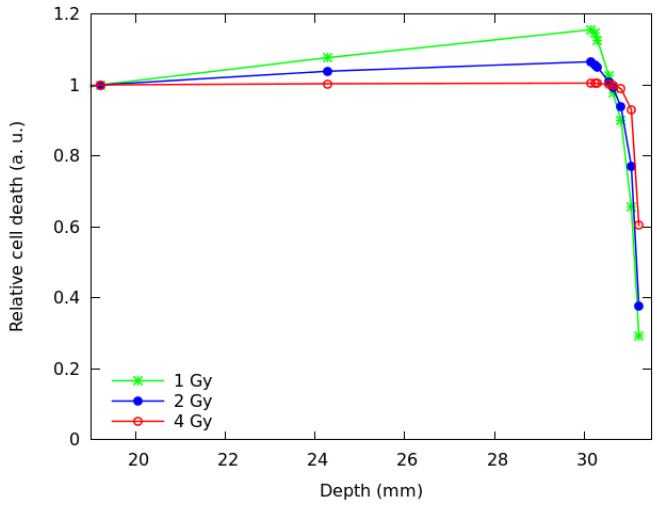

Figure 4.11: Predicted fraction of inactivated cells at different depths along the SOBP, assuming a plateau dose of 1 Gy (green symbols), 2 Gy (blue symbols), or 4 Gy (red symbols). Each quantity was normalized with respect to the proximal position. The lines are simply guides for the eye [153].

thus, additional depth positions, with respect to those considered in Figures 4.11 and 4.12) can be derived by linear interpolation. If the yield of lethal aberrations induced by the same dose of X-rays is known (for instance, from experiments), R_{LA} would then provide the yield of lethal aberrations induced by protons (LA_p). According to our model, LA_p would then allow calculating proton cell survival for these additional depth positions.

After investigating the proton effectiveness dependence on the biological endpoint and dose level (in addition to depth), the model was also applied to V79 hamster fibroblasts in order to address also the dependence on the target radiosensitivity. The first step consisted of reproducing with the model simulations a set of experimental cell survival curves, as illustrated in Section 4.2.1 and reported in Figure 4.8. The results were then used to evaluate cell death and chromosome aberrations for V79 cells along the same SOBP dose profile used for AG01522 cells. While for human fibroblasts a real experiment has been performed with the CATANA proton beam, for V79 cells the results presented below are pure model predictions.

Figures 4.15 and 4.16 report predictions of cell death (i.e., fraction of inactivated cells) and chromosome aberrations (i.e., mean number of dicentrics per cell) for V79 cells along the proton SOBP of Figure 4.5, as well as the dose profile. The results, which were obtained assuming a plateau dose of 2 Gy, were normalized with respect to the proximal position. The considered LET values are those considered in Figure 4.8, in addition to three other values (i.e. 3.0, 10.1 and 20.0 keV/μm, for which the survival data for comparison were taken from [102], [46] and [142], respectively), which were not reported

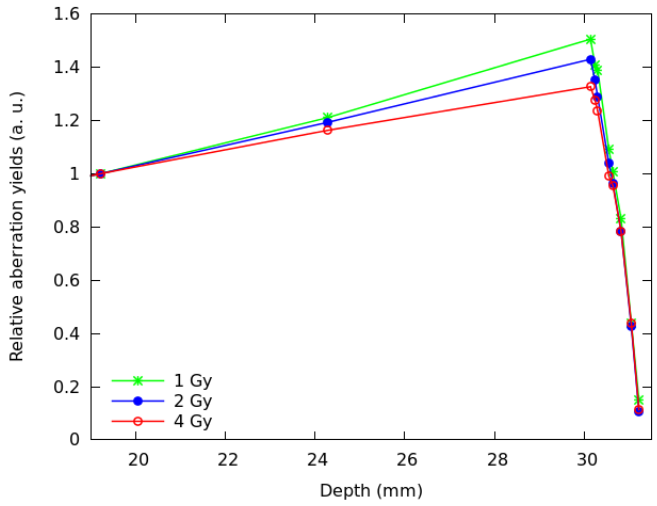

Figure 4.12: Predicted mean number of dicentrics per cell at different depths along the SOBP, assuming a plateau dose of 1 Gy (green symbols), 2 Gy (blue symbols), or 4 Gy (red symbols). Each quantity was normalized with respect to the proximal position; the lines are simply guides for the eye [153].

in Figure 4.8. The corresponding depths were calculated from the LET profile reported in Figure 4.5 (panel *b*).

Like for AG01522 cells, the beam effectiveness was found to increase along the plateau, and high levels of biological damage were also found beyond the distal dose fall-off. Moreover, the increase in chromosome aberrations along the plateau was more pronounced than the increase in cell killing, reflecting the radiation effectiveness dependence on the specific endpoint. Interestingly, the increase in biological effectiveness was more pronounced for V79 cells than for AG01522 cells. For instance, for V79 cells the fraction of inactivated cells increased along the plateau by a factor that was more than 1.2, whereas for AG01522 cells this factor was < 1.1. This behaviour reflects the dependence of proton effectiveness on the last investigated factor, that is cell radiosensitivity; moreover it is consistent with the higher RBE generally shown by cells exhibiting smaller α/β ratios [104], as is the case of V79 cells.

In conclusion, in line with other works, this study indicated that assuming a constant RBE along a proton SOBP may be sub-optimal. In particular, as follows from Figures 4.9 and 4.15, if the dose profile was not flat, but decreasing with depth to have a flat biological effectiveness for the more radiosensitive tissue (which is generally the healty tissue), the effectiveness in the radioresistant tissue (generally, the tumor) would still remain sufficiently high. In this way the tumor would receive a level of damage (cell death) that is not smaller than expected, but the damage to healty tissues, both in the distal and fall-off regions, may be reduced, thus limiting possible damages to organs at risk. Figure 4.17 reports a modulated depth-dose profile which would allow

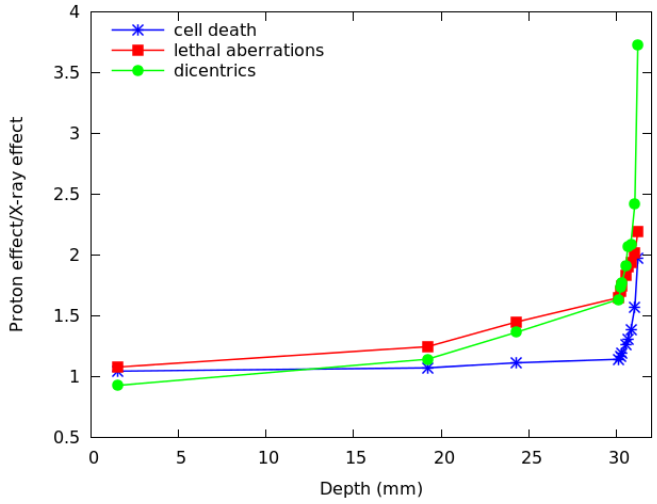

Figure 4.13: R_I (ratio between proton-induced and X-ray-induced cell inactivation after the same dose, blue symbols), R_{LA} (ratio between proton-induced and X-ray-induced lethal aberrations after the same dose, red symbols), and R_{DIC} (ratio between proton-induced and X-ray-induced dicentrics after the same dose, green symbols) calculated at different depths of the SOBP dose profile of Figure 4.5, assuming a plateau dose of 2 Gy. The lines are simply guides for the eye [153].

for a flat biological effectiveness in AG cells along the considered SOBP (in terms of cell death and chromosome aberrations), according to the BIANCA II model calculations. In order to obtain this result, the dose position should be reduced of about 20% compared to the proximal point.

4.2.3 Application to carbon ions

An analogous study was carried out on a carbon ion SOBP, again with the BIANCA II model version. The experimental data used for comparison consist of several survival curves of V79 hamster fibroblasts irradiated with carbon ions at different dephts along a SOBP used for the radiobiological characterization of the CNAO beam, shown in Figure 2.12. The five irradiation depth positions are at 4, 12.5, 14, 16 and 17.5 cm, corresponding to dose-average LET values of 14, 35, 38, 53 and 100 keV/μm, respectively [107]. A X-ray curve was also used as reference.

The main goal of our study was the evaluation of the variations in carbon ion effectiveness (in terms of cell death and chromosome aberrations) along the SOBP. The first step of the work consisted of reproducing the five survival curves obtained at CNAO by irradiating V79 cells in the five depth positions, plus the X-ray curve. In the simulations, the value of the unrejoining parameter f was maintained fixed at 0.08 (as determined in Section 3.3.2), and the CL

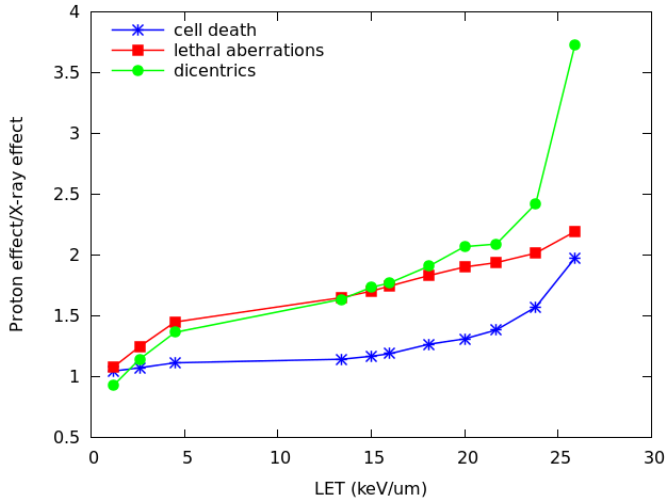

Figure 4.14: R_I (ratio between proton-induced and X-ray-induced cell inactivation after the same dose, blue symbols), R_{LA} (ratio between proton-induced and X-ray-induced lethal aberrations after the same dose, red symbols), and R_{DIC} (ratio between proton-induced and X-ray-induced dicentrics after the same dose, green symbols) for the (dose-averaged) LET values corresponding to the depth positions considered in Figure 4.13. The lines are simply guides for the eye [153].

yield was the only parameter to be adjusted for every curve, in order to find a good agreement with the data. For photons a value of 1.1 CLs·Gy^{-1}·cell^{-1} was used, while for carbon ions the values ranged between ∼3.1 CLs·Gy^{-1}·cell^{-1} (for the 14 keV/μm curve) and ∼5.2 CLs·Gy^{-1}·cell^{-1} (for the 100 keV/μm curve). In Figure 4.18 both the experimental data (points with 1σ error bars) and the simulation results (lines) are shown. The 38 keV/μm curve is not reported to avoid making the figure too "crowded". The agreement between simulations and experiments is good, with χ^2 values smaller than 1 for the 14 and 53 keV/μm curves, aroud 2.5 for the 100 keV/μm curve, and higher than 3 for the 35 and 38 keV/μm curves. The higher chi square values found for 35 and 38 keV/μm are entirely due to the point at 4 Gy, while all other points were within one Standard Deviation from the experimental data.

As a subsequent step, like in the case of the proton SOBP illustrated in the previous Section, a characterization of the variation of different endpoints with depth was performed also for the carbon ion case. For a constant dose of 2 Gy along the SOBP region (that is between 12.5 and 17.5 cm), the variations of cell surviving fraction (and thus cell death) and dicentric yield were quantified, according to the model predictions. Like in the previous study, cell death was analyzed since it is a quantifier for the damage to the tumor, while dicentrics are a good index for the damage to healty tissues: since their yield is comparable to the yield of reciprocal translocations, which in turn are related

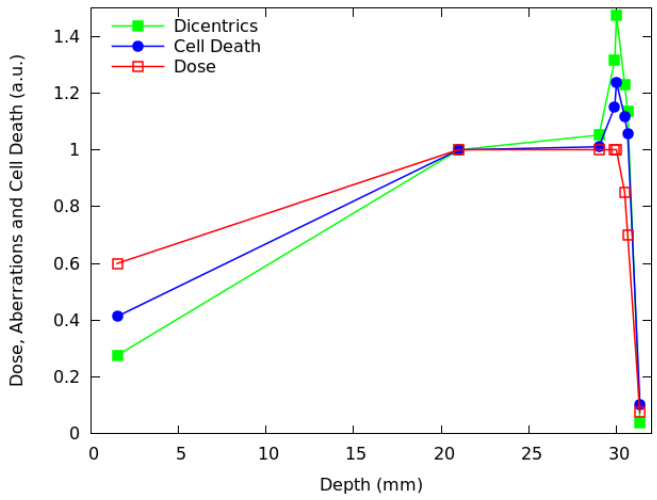

Figure 4.15: Predicted fraction of inactivated cells (blue symbols) and mean number of dicentrics per cell (green symbols) for V79 cells at different depths of the SOBP dose profile reported in Figure 4.5, which is also shown in the figure (red symbols). Each quantity was normalized to the proximal point. The lines are simply guides for the eye [153].

to cell conversion to malignancy.

Figure 4.19 shows the cell surving fraction S, the fraction of inactivated cells (defined as 1-S) and the dicentric yield (average number of dicentrics per cell) for the four positions along the carbon ion SOBP. The LET values corresponding to these positions are 35, 38, 53 and 100 keV/μm. All the values reported in Figure 4.19 were normalized to the values assumed at the proximal point. Interestingly, the fraction of inactivated cells increased by a factor $\sim$1.4 (from the proximal to the distal point), while the dicentric yield increased by a factor $\sim$2. Again, the variation in effectiveness depends on the considered biological endpoint. From this plot it clearly appears the well-known necessity to modulate the dose profile along the SOBP, in order to obtain a flat biological effectiveness.

4.3 Other applications

In addition to the studies aimed to DNA damage characterization and to applications for hadrontherapy, the BIANCA model also allows for other types of applications. The first result presented in this Section concerns the investigation of a particular case of interest in radiobiology, that is the biological effectiveness of a microbeam, where each cell is irradiated with an exact number of ions. Afterwards, a study concerning the statistical distribution of different types of chromosome aberrations in irradiated cells will be illustrated. Finally a further analysis of the trend of Cluster Lesions will be presented, with the

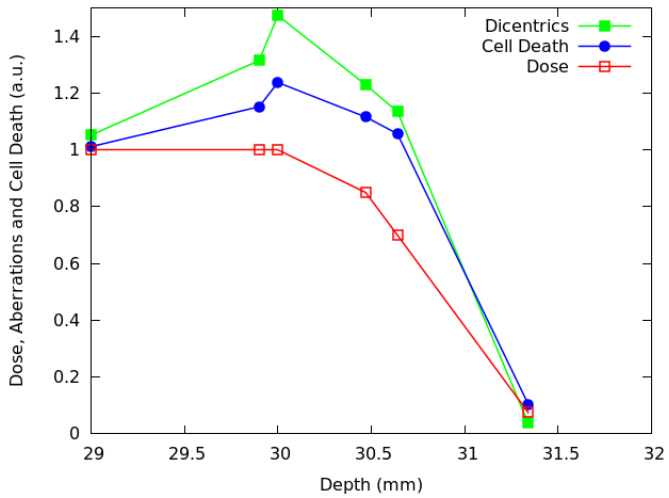

Figure 4.16: Distal and fall-off region of the SOBP shown in Figure 4.15 [153].

aim of going towards a purely predictive model. All these last results are still preliminar.

4.3.1 Microbeam irradiation

In a conventional broad-beam *in vitro* irradiation the effects of single particles cannot be quantified, due to the Poisson distribution of particle tracks traversing the target cells. However the damage induced by an exact number of particles can be studied and analyzed thanks to charged-particle microbeam facilities. These studies are important in radiobiology since they are performed in controlled conditions, allowing for a good knowledge of the energy absorbed by a cell in terms of space, time and quantity. With the BIANCA Monte-Carlo code (and its different versions) it is possible to faithfully simulate the exact irradiation conditions, by fixing a well-defined number of traversing particles and their positions. At the Physikalisch-Technische Bundesanstalt (PTB-Braunschweig) an ion microbeam facility is available. The accelerator facility, including a Van-de-Graaff (VdG) accelerator and an energy variable cyclotron, can provide protons with energies between 1 and 20 MeV and alpha particles with energies between 1 and 28 MeV. The achievable LET values range between 3 keV/μm and 200 keV/μm in water. The beam diameter is less than 2 μm (FWHM), obtained thanks to the focusing properties of quadrupole magnets. More details on the facility can be found in [174] and [175].

In the framework of the 'BioQuaRT' (Biologically weighted Quantities in RadioTherapy) EU project coordinated by Hans Rabus an *in situ* protocol for the analysis of the chromosome damage induced by charged particles has been developed. This method allows for the simultaneous scoring of chromosome aberrations and micronuclei on the same irradiated sample (although in this

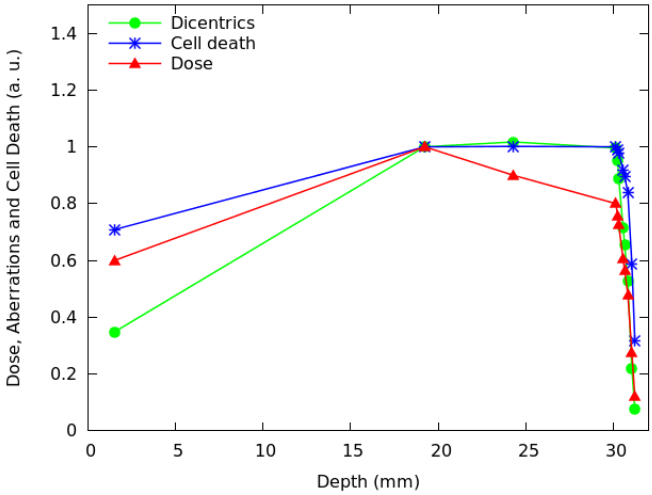

Figure 4.17: Modulation of the depth-dose profile which, according to the BIANCA II model, would allow for a flat effectiveness (in terms of cell death and chromosome aberrations) for AG01522 cells [173].

work we were only interested in aberrations). Details on this approach can be found in [176]. In this context the following experiment has been performed by Patrono et al.: different types of chromosome aberrations (in particular dicentrics, rings and acentric fragments) have been scored after microbeam irradiation with protons and alpha particles of different energies. The ions were provided by the PTB microbeam, and the irradiation was performed on Chinese Hamster Ovary (CHO) cells, widely used in radiobiology experiments. In particular the considered radiation qualities were: 10 MeV He-ions, 20 MeV He-ions or 10 MeV protons. The corresponding LET values were 90, 37 and 4.7 keV/μm, respectively, while the number of particles per cell were 10, 25 or 200, respectively. These numbers were chosen in order to have approximately the same nominal dose deposition in every cell: in agreement with Equation 1.11, and assuming the same cross-sectional area for each cell, the product between number of particles and LET should remain constant. For all radiation qualities, five (nominal) positions were targeted in each cell nucleus, corresponding to the following coordinates in a system with the origin in the nucleus centre: (0,0), (2,2), (-2,2), (-2,-2), (2,-2).

Concerning the simulation work performed within this thesis, the first step consisted of estimating the (mean) dose to the cell nucleus, developing an *ad hoc* simulation code. The cell nucleus was represented as a spherical calotte with variable base area (mean value = 68 μm^2) and fixed maximum thickness (4 μm). For each cell, the actual nucleus area was taken from a Gaussian distribution with mean value = 68 μm^2. Like in the experiments, each nucleus was irradiated from the bottom by a well-determined number of particles, dependent on particle type and energy. The nominal positions of the particle

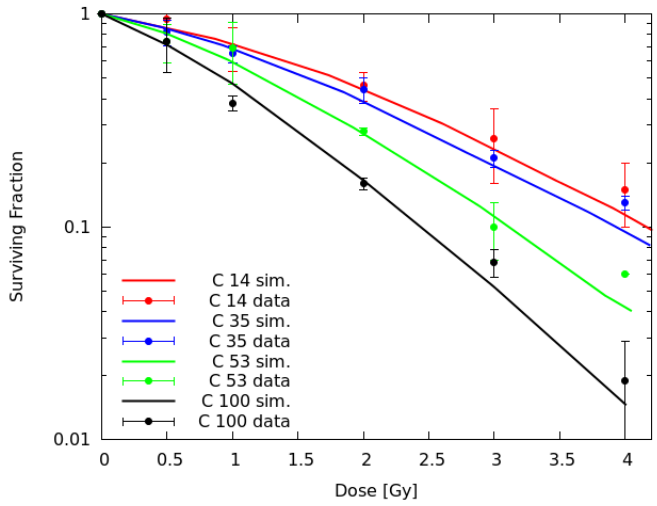

Figure 4.18: Cell survival curves for V79 hamster fibroblasts exposed at four depth positions along a carbon ion SOBP (corresponding to the following dose-averaged LET values: 14, 35, 53 and 100 keV/μm). The lines are simulation outcomes, the points are experimental data obtained at CNAO [A. Facoetti, personal comunication].

tracks were the five mentioned above; in order to take into account the intrinsic uncertainties, the actual position for a particle entering the nucleus was "shifted" radially with respect to the nominal position, by a quantity taken from a Gaussian distribution with FWHM = 4.5 μm (as measured in this particular experiment). This way, about 11% of the particles were found to fall outside the cell nucleus. For each cell nucleus, the energy deposited by each particle traversal was calculated multiplying the particle LET by the nucleus traversal length, and the dose to that nucleus was calculated dividing the energy deposited by all particle traversals by the mass of that nucleus (assuming 1 g/cm^3 as a density). Finally, the mean dose was calculated summing up all doses and dividing them by the number of considered cells. Such calculations provided a mean dose of 2.3 Gy. These estimations are consistent with independent calculations performed by Nagasawa and Little [177] for the same cell line exposed to a 112 keV/μm alpha-particle broad beam, for which the authors calculated that at 2 Gy the mean number of nucleus traversals was 11. Their calculations were based on CR-39 fluence measurements and a mean nuclear area of 62.2 μm^2.

After estimating the mean dose, in the context of chromosome aberration simulations the cell nuclei were modelled as cylinders with circular base (radius: 4.7 μm; height: 4 μm); the assumed geometry was simpler than that used for dose estimation for the sake of simplicity. The mean distance between two adjacent chromosomes, that is the threshold distance d, resulted to be 2.9 μm, while the unrejoining parameter f was set equal to 0.08 like for the

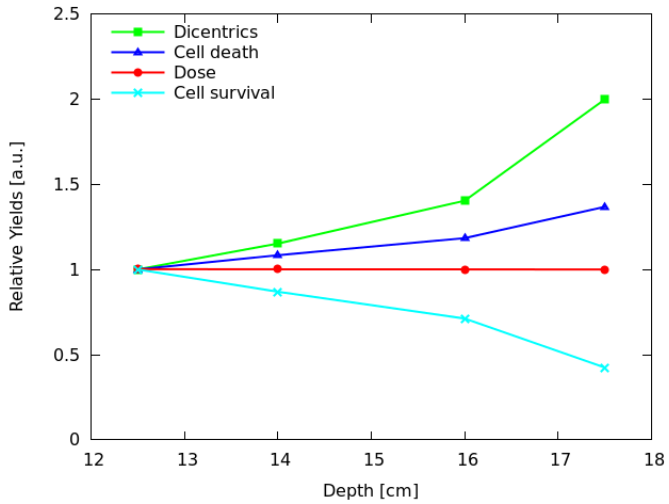

Figure 4.19: Calculated fraction of inactivated (blue) and surviving cells (light blue), and calculated mean number of dicentrics per cell (green) at different depths of the SOBP reported in Figure 2.12. The dose level was fixed at 2 Gy (red). Each quantity was normalized with respect to the proximal position. The lines are simply guides for the eye.

previous work on V79 Chinese Hamster lung fibroblasts (see Section 3.3.2).This corresponds to assume similar DNA repair mechanisms for different types of Chinese hamster fibroblasts, which seems a reasonable approximation. To simulate the irradiation, the CLs were distributed within the nucleus along parallel segments representing the "core" of the particle tracks for both protons and alphas, with a fixed number of particles depending on radiation quality. The entering ion positions were established as described above. The procedure of chromosome aberration simulation and scoring was the same described in Chapter 3.

Table 4.1 reports, for the three considered radiation qualities, calculated yields of Dicentrics + Rings, as well as excess acentric fragments. The corresponding experimental yields (with errors calculated assuming Poisson statistics) are reported in parenthesis. The last two columns report the mean number of "Cluster Lesions" (per particle and per cell, respectively) used to perform the calculations. By tuning the CL yields in order to find a good agreement with the experimental yield of D+R, the experimental ACE are overestimated; the discrepancy between data and simulations tends to become more pronounced with decreasing LET. This might represent an indication that the f parameter should be LET-dependent, because smaller f values with decreasing LET would lead to smaller yields of acentric fragments. As an example, setting f equal to 0.02 in the case of 37 keV/μm alphas would lead to 0.34 D+R and 0.22 ACE, in agreement with the experimental data.

Finally it is worth mentioning that the increase in the yield of CL/particle

Ion	E	LET	Ions	(D+R)/cell	ACE/cell	CL/ion	CL/cell
α	10	90	10	.60 (0.60±0.06)	.78 (0.69±0.07)	0.82	8.2
α	20	37	25	.35 (0.36±0.04)	.50 (0.21±0.03)	0.24	5.9
p	10	4.7	200	.35 (0.36±0.06)	.48 (0.15±0.04)	0.029	5.8

Table 4.1: Calculated yields of Dicentrics+Rings (D+R) and excess acentric fragments (ACE) obtained by irradiating CHO cells with a fixed number of particles. The energy is expressed in MeV, while the LET in keV/μm. The three used radiation qualities are: 10 MeV alphas, 20 MeV alphas or 10 MeV protons. The CL yields (per particle and per cell) used in the simulations are also reported. The experimental data for comparison reported in parenthesis were kindly provided by A. Testa and C. Patrono (personal communication).

is consistent with the increase in LET: from 37 keV/μm alphas to 90 keV/μm alphas, the LET increases by a factor $\sim$2.4 and the CL/particle increases by a factor $\sim$3.4; from 4.7 keV/μm protons to 37 keV/μm alphas, the LET increases by a factor $\sim$7.9 and the CL/particle yield increase by a factor $\sim$8.3. On the contrary, the yield of CL/cell reflects both the LET and the number of particles: from 37 keV/μm alphas to 90 keV/μm alphas, the LET increases by a factor $\sim$2.4 but the number of particles per cell decrease by a factor 2.5; from 4.7 keV/μm protons to 37 keV/μm alphas, the LET increases by a factor 7.9 but the number of particles decreases by a factor 8, leading to similar yields of CL/cell and thus similar yields of aberrations/cell.

4.3.2 Chromosome aberration distributions

In *in vitro* studies addressed to the investigation of chromosome aberrations, in addition to aberration yields also their statistical distribution can be of interest in order to better understand the biophysical mechanisms leading to the production of this cytogenetic damage. Several theoretical and experimental works have dealt with this topic, pointing out that, while in some cases chromosome aberration distributions can be approximated by a Poisson distribution, under various conditions this approximation is not valid [178] [179] [180] [181]. Indeed in many cases these distributions appear to be overdispersed, i.e. they have a variance larger than their mean; at high doses also underdispersion has been observed [182]. Moreover the shape of the distributions varies with the considered aberration type and the radiation quality: in particular the displacement from poisson distribution appears to be more significative for high LET particles.

Within this thesis work an analysis of chromosome aberration distributions, both on experimental data and on simulations by the BIANCA II model, was performed. An original tool for this analysis was developed using the Python programming language and the scientific NumPy framework: different statisti-

cal distributions can be compared with both experimental and simulated data, and their agreement can be evaluated by a Chi Square test. The first analyzed data were those by Carrano [39], presented in Table 3.3. As already pointed out by the author of the original paper, the distribution of two-hit aberrations (dicentrics plus rings) induced in V79 cells by 3 Gy photons can be fitted by a Poisson distribution, with a high agreement confirmed by a χ^2 value smaller than 1. The same consideration holds for the distribution simulated by the BIANCA II model, which was found to be in agreement with the experimental data. This result is also supported by other works, such as the one by Edwards et al. [178], who observed that the distribution of dicentrics may be described by Poisson statistics in the case of X-ray irradiation.

However, according to the simulations performed with the BIANCA II code, the situation appears different if specific cases (e.g. particular aberration types or their combinations) are taken into account. For instance, in the case of V79 cells exposed to 2 Gy of X-rays, while the single aberration categories were approximately fitted by a Poisson distribution, the yields of total Lethal Aberrations (dicentrics plus centric and acentric rings plus deletions) showed a deviation with respect to Poisson statistics, as shown in Figure 4.20. The reduced χ^2 value was of ∼15.1.

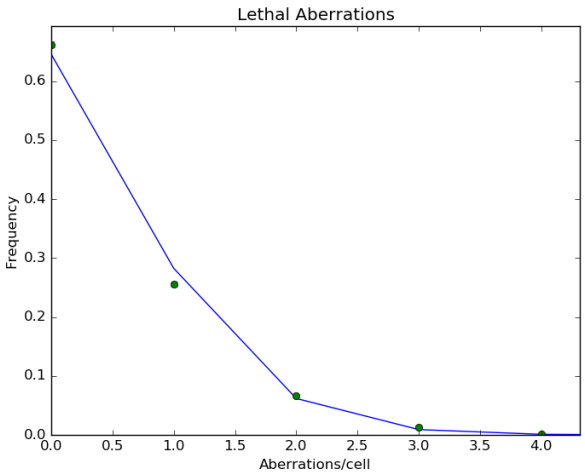

Figure 4.20: Frequencies of Lethal Aberrations (dicentrics plus centric and acentric rings plus deletions) per cell induced in V79 cells by 3 Gy of X-rays. The points are the outcomes of simulations carried out by the BIANCA II model (with error bars smaller than the symbol size), the line represents a Poisson distribution having the same mean value as the data. The reduced χ^2 value was ∼15.1

The subsequent step consisted of searching for a statistical distribution that could better describe the simulation outcomes. By considering that, according to the model assumptions, the yield of DNA Cluster Lesions (CL) follows the

Poisson statistics, and that chromosome aberrations are the result of random rejoining between pairs of chromosome fragments produced by the initial CLs, it is reasonable to think that chromosome aberrations should not follow the Poisson statistics. We thus took into account a compound Poisson-Poisson (Neyman type A) distribution, in which the number of aberrations per cell is given by the product between the number of CLs per cell and the mean number of aberrations induced by one CL. The number of aberrations per cell induced by n CLs is thus given by the following probability distribution

$$P_{n\mu}(m) = \frac{(n\mu)^m e^{-n\mu}}{m!} \tag{4.1}$$

where μ represents the mean number of aberrations per CL. Since the number of CLs, n, is a Poisson variable with a certain mean λ, the aberration distribution of aberrations can be computed by a Neyman type A distribution, as follows

$$P(m) = \sum_{n=0}^{\infty} P_{n\mu}(m) P_{\lambda}(n) = \sum_{n=0}^{\infty} \frac{(n\mu)^m e^{-n\mu}}{m!} \frac{\lambda^n e^{-\lambda}}{n!} = \frac{\mu^m e^{-\lambda}}{m!} \sum_{n=0}^{\infty} \frac{n^m (e^{-\mu}\lambda)^n}{n!} \tag{4.2}$$

In the considered case the mean number of CL per cell, λ, was $\sim$2.91, while the mean number of aberrations per cell was $\sim$0.44. The mean number of aberrations per CL, μ, was therefore $\sim$0.15. Using these values we obtained a distribution in high agreement with the simulation outcomes on Lethal Aberrations, as shown in Figure 4.21. The agreement between the theoretical distribution and the simulation outcomes is quantified by a reduced χ^2 value of $\sim$0.91. Therefore the Neyman type A distribution, already used by other authors for heavy particle irradiation [179], seems to fit well the "total" aberration data also for X-ray irradiation. It is important to note that in our case this was not a fitting procedure, since there was no adjustable parameter; all the quantities in Equation 4.2 were indeed known and fixed *a priori*. Interestingly, the agreement with the simulation outcomes on the single aberration types (in particular dicentrics and deletions) was better for the Poisson distribution than for the Neyman one; this issue deserves further investigation.

A similar approach was applied to proton irradiation. In that case the compound Poisson-Poisson distribution was derived from the distribution of the particle tracks in the cell nucleus (which is poissonian by definition in the BIANCA model) and the distribution of chromosome aberrations per track. Denoting the number of tracks traversing a cell nucleus with k, and their mean value with ξ, the resulting distribution was

$$P(m) = \sum_{k=0}^{\infty} \frac{(k\mu)^m e^{-\mu}}{m!} \frac{\xi^k e^{-\xi}}{k!} = \frac{\mu^m e^{-\xi}}{m!} \sum_{k=0}^{\infty} \frac{k^m (e^{-\mu}\xi)^k}{k!} \tag{4.3}$$

In this case μ clearly represents the mean number of aberrations per track. This distribution was compared with simulation outcomes of "total" chromosome

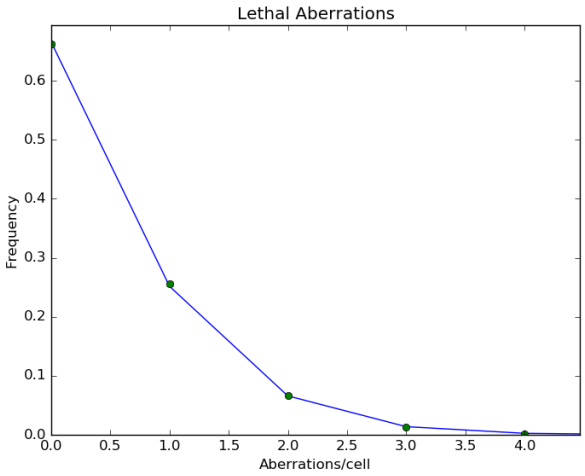

Figure 4.21: Frequencies of Lethal Aberrations (dicentrics plus centric and acentric rings plus deletions) per cell induced in V79 cells by 3 Gy of X-rays. The points are the outcomes of simulations by the BIANCA II model, the line is the represent the trend of a Neyman type A distribution. The reduced χ^2 value for the evaluation of the agreement between the data and the theoretical distribution is $\sim$0.91

aberrations induced in V79 cells by 27.6 keV/μm protons at a dose of 2 Gy. In this case the mean number of tracks k was $\sim$51, while the mean number of aberrations per cell was $\sim$1.31. Therefore the mean number of aberrations per track, μ, was $\sim$0.026. The agreement of such a distribution with the simulation outcomes was better with respect to a Poisson distribution having mean equal to the average number of aberrations per cell. However the agreement was not good as in the case of X-rays, and the χ^2 value was $\sim$9. This was probably due to the high average number of tracks per cell nucleus, which led to a distribution quite similar to the original simple Poisson distribution. Treating k as a free parameter and performing a fitting procedure, the agreement of the Neyman type A distribution would be higher, but the aim of the present study is to find a distribution that, basing on mechanistic assumptions and without parameter adjustment, allows for the description of simulated and experimental data. This work is clearly at a preliminary stage; a testing of other distributions (for example the negative binomial) and a systematic extension of this approach to other cell lines (such as AG1522 human fibroblasts) and other ion types (in particular carbon ions) is currently in progress.

4.3.3 Towards a predictive model

The last study performed within this thesis work was addressed to a deeper analysis of the experimental data and the parameters used for the simulations,

in order to obtain a purely predictive model. The basic idea was to collect a wide data set on a single reference cell line, exposed to several radiation qualities, and to predict the response of other cell lines to different types of radiation (only their response to photons is needed). In particular we developed a formula allowing to convert the Cluster Lesion yield (input prameter of the BIANCA II model) of the reference cell line in the "right" yield for another cell line, depending on the ion type and LET used for the irradiation. In this case we chose V79 hamster fibroblasts as a reference target cell line (due to the abundance of data in the literature) and AG human fibroblasts as representative target on which testing the approach. This choice was simply due to the availability of data already collected for the previous studies performed in this thesis, but in principle this method may be extended to other cell lines.

First we analyzed the trend of the CL yields used as input for the simulations of V79 survival curves, both for protons and for carbon ions. The considered radiation qualities are those reported in Sections 4.2.1 and 4.2.3, that is: protons of 7.7, 11, 17.8 and 27.6 keV/μm; carbon ions of 14, 35, 38, 53, and 100 keV/μm. The average number of CLs/(Gy·cell) and CLs/μm used to perform the simulations which led to the curves shown in Figures 4.8 and 4.18 are reported in tables 4.2 and 4.3. The mean number of CLs/μm can be derived from

$$\frac{CL}{\mu m} = \frac{CL}{cell} \cdot \frac{1}{N \cdot l} \tag{4.4}$$

where N is the average number of particles traversing the cell nucleus and l is the lenght of every traversal (corresponding to the nucleus thickness); however they can be easily calculated through Equation 3.2. The average number of CLs/μm showed a highly regular dependence on LET, as shown in Figure 4.22 for protons and Figure 4.23 for carbon ions. The two curves were fitted by a linear-quadratic function like the following one

$$\left\langle \frac{CL}{\mu m} \right\rangle = a \cdot LET + b \cdot LET^2 \tag{4.5}$$

The fit parameters were

$$\begin{aligned} a_p &= 3.72 \cdot 10^{-4} \\ b_p &= 1.38 \cdot 10^{-5} \end{aligned} \tag{4.6}$$

for protons, and

$$\begin{aligned} a_C &= 4.70 \cdot 10^{-4} \\ b_C &= 5.45 \cdot 10^{-6} \end{aligned} \tag{4.7}$$

for carbon ions. Thanks to these fits, the value of $\langle CL/\mu m \rangle$, and consequently of $\langle CL/(Gy \cdot cell) \rangle$, for any LET value (in the considered range) of the two ion types, can be known with a good approximation.

Protons (V79)				
$\boldsymbol{LET[keV/\mu m]}$	7.7	11	17.8	27.6
$\boldsymbol{\langle CL/(Gy \cdot cell)\rangle}$	2.0	2.3	2.6	3.2
$\boldsymbol{\langle CL/\mu m\rangle[10^{-3}]}$	3.6	6.0	10.8	20.8

Table 4.2: Average numbers of CL/(Gy·cell) and of CL/μm used to reproduce V79 survival curves by protons of different LET. The curves are those reported in Figure 4.8.

Carbon ions (V79)					
$\boldsymbol{LET[keV/\mu m]}$	14	35	38	53	100
$\boldsymbol{\langle CL/(Gy \cdot cell)\rangle}$	2.5	2.6	2.9	3.3	4.3
$\boldsymbol{\langle CL/\mu m\rangle[10^{-3}]}$	8.2	21.5	26.0	41.2	101.4

Table 4.3: Average numbers of CL/(Gy·cell) and of CL/μm used to reproduce V79 survival curves by carbon ions of different LET. The curves are those reported in Figure 4.18.

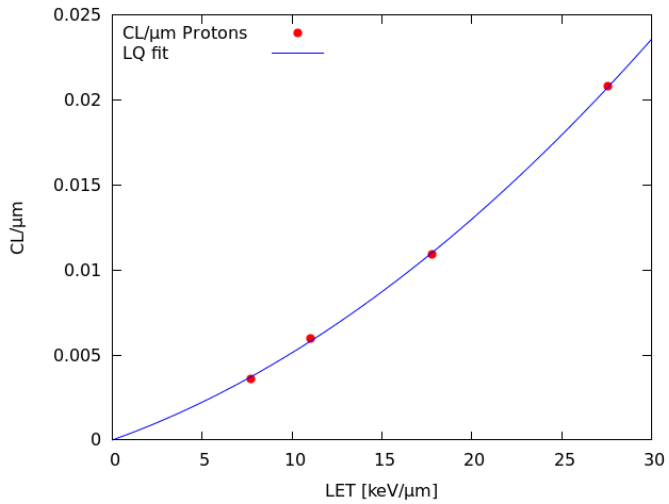

Figure 4.22: Yields of CL/μm used to reproduce the V79 survival curves by protons reported in Figure 4.8. The line represents the linear-quadratic fit of the points.

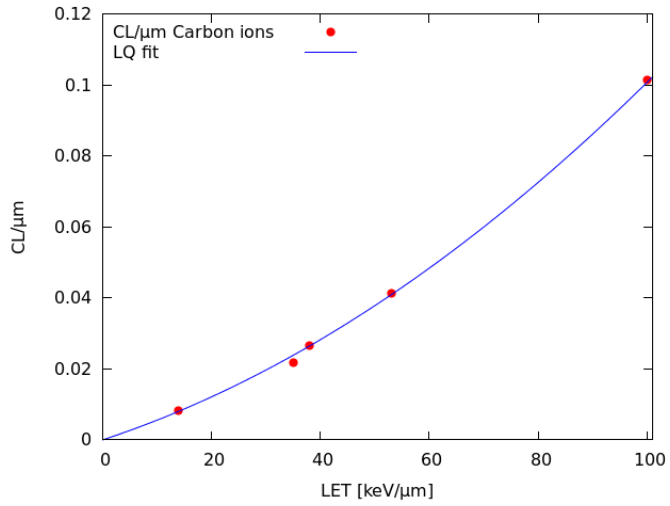

Figure 4.23: Yields of CL/μm used to reproduce the V79 survival curves by carbon ions reported in Figure 4.18. The line represents the linear-quadratic fit of the points.

After that, a formula to convert the yield of CL/μm for V79 cells into a yield of CL/μm for AG cells for any LET value was derived, taking into account that the differences in the induction of DNA damage in two different cell lines rely not only on the different cell radiosensitivity, but also on the target geometry. These two features were represented by the yield of Cluster Lesions per unit DNA mass (for example per Dalton) induced by a reference radiation and the DNA density (that is the number of DNA Dalton in the nucleus volume), respectively. The resulting formula was

$$\left\langle \frac{CL}{\mu m} \right\rangle_{AG,p} = \left\langle \frac{CL}{\mu m} \right\rangle_{V79,p} \cdot \frac{\left\langle \frac{CL}{Gy \cdot Da} \right\rangle_{AG,X}}{\left\langle \frac{CL}{Gy \cdot Da} \right\rangle_{V79,X}} \cdot \frac{N_{Da,AG}}{V_{AG}} \cdot \frac{V_{V79}}{N_{Da,V79}} \tag{4.8}$$

The index p refers to the incident radiation (protons in this case, but the same holds for carbon ions), the index X refers to the reference radiation (X-rays), N_{Da} is the number of DNA Dalton in a cell nucleus and V is the nucleus volume. Since the product between CLs/(Gy·Da) and the number of Dalton contained in the nucleus is the quantity CLs/(Gy·cell), Equation 4.8 reduces to

$$\left\langle \frac{CL}{\mu m} \right\rangle_{AG,p} = \left\langle \frac{CL}{\mu m} \right\rangle_{V79,p} \cdot \frac{\left\langle \frac{CL}{Gy \cdot cell} \right\rangle_{AG,X}}{\left\langle \frac{CL}{Gy \cdot cell} \right\rangle_{V79,X}} \cdot \frac{V_{V79}}{V_{AG}} \tag{4.9}$$

This formula is compatible with Equation 3.2 if one assumes that

$$\frac{\frac{CL}{Gy \cdot cell}_{AG,X}}{\frac{CL}{Gy \cdot cell}_{V79,X}} = \frac{\frac{CL}{Gy \cdot cell}_{AG,p}}{\frac{CL}{Gy \cdot cell}_{V79,p}} \tag{4.10}$$

which is reasonable, since these ratios should reflect the response of the target to radiation, with no dependence on the projectile. Since the yield of CL/μm is known for the reference cell line (V79) at any LET, the predicted yield of CL/μm for the new cell line (AG) can be deduced, for any LET value as well, thanks to Equation 4.9.

The final step consisted of the verification of the validity of this Formula. For protons the goal was to reproduce with BIANCA II the survival curves by Chaudhary et al. [45] presented in Section 4.6; however, while in that case the CL input parameter was adjusted separately for each curve to find a good agreement with the experimental data, now the CL yield was deduced from Equation 4.9, applied to the V79 data set. In particular the LET proton values used for AG01522 irradiation (1.1, 4.0, 7.0, 11.9, 18.0 and 22.6 keV/μm) were used in Equation 4.5 with parameters taken from 4.6; the $\langle CL/\mu m \rangle$ values for V79 cells thus found were then used in Equation 4.9 in order to find $\langle CL/\mu m \rangle$ values for AG survival curve simulations. For both cell lines the CL yields for X-rays irradiation for both the cell lines were those used in Section 4.2.1 (1.5 and 3.3 CL·Gy^{-1}·cell^{-1} for V79 and AG, respectively). The six $\langle CL/\mu m \rangle$ values found in correspondence to the six LET values were finally converted into values of CLs·Gy^{-1}·cell^{-1} and used as input for the simulations of the survival curves. The obtained CL yields are reported in Table 4.4, while the results of the simulations are shown in Figure 4.24. The agreement between the simulated curves and the experimental data was very good for the lower LET values, with reduced χ^2 values of 1.3 and 1.1 for the first two curves; the χ^2 values were between 4 and 8 for the three subsequent curves, and the agreement was basically lost for the 22.6 keV/μm curve. This issue deserves further investigation, but it is worth underlining that the simulations are pure model predictions, without any *a posteriori* parameter tuning.

Protons (AG01522)						
$\boldsymbol{LET[keV/\mu m]}$	1.1	4.0	7.0	11.9	18.0	22.6
$\boldsymbol{\langle CL/(Gy \cdot cell)\rangle}$	3.9	4.3	4.7	5.3	6.1	6.6
$\boldsymbol{\langle CL/\mu m\rangle[10^{-3}]}$	1.0	4.2	8.0	15,7	27.4	37.9

Table 4.4: Average numbers of CL/(Gy·cell) and of CL/μm obtained from Equation 4.9 and used to reproduce AG survival curves by protons of different LET.

Concerning carbon ion irradiation, the same method was used, starting from the V79 data set of Figure 4.8 and applying Equation 4.9 to deduce the $\langle CL/\mu m \rangle$ to simulate AG survival curves by carbon ions of different LET.

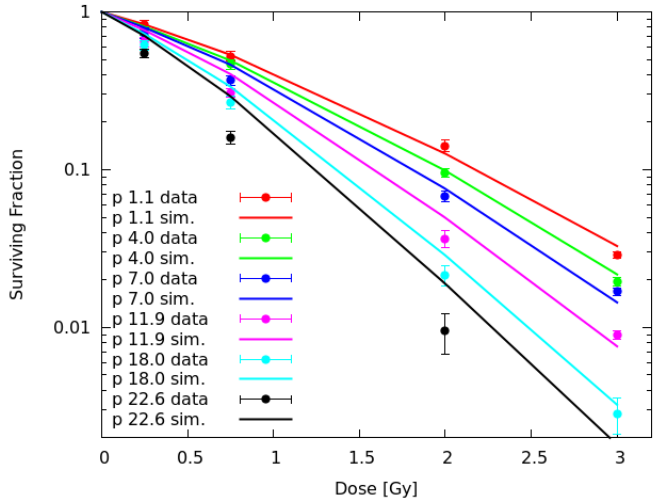

Figure 4.24: Pure model predictions, without any parameter tuning, compared with experimental survival curves for AG cells irradiated by protons of different LET (1.1, 4.0, 7.0, 11.9, 18.0 and 22.6 keV/μm). The lines are model simulations, whereas the points are experimental data.

The experimental data are those reported in Figure 3.6 and 3.7: 76.3 and 108 keV/μm carbon ion data were taken from Hamada et al. [137], while the 48.8 and 147.6 keV/μm data were taken from Kavanagh et al. [146]. The CL yields for photon irradiation were 1.1 and 1.7 CL·Gy^{-1}·cell^{-1} for V79 and AG cells, respectively. The four CLs·Gy^{-1}·cell^{-1} obtained for the four carbon LET values are reported in Table 4.5; the comparison between simulated and experimental survival curves is shown in Figure 4.25. The agreement was good, with reduced χ^2 values between 1.5 and 3.3 for the first three curves. The curve with the highest LET was characterized by a high χ^2 value, which however becomes smaller than 1 if the point at 1.5 Gy is not taken into account; moreover the shape of the simulated curve was very similar to the linear-quadratic data fit. Again, the relevance of these results relies on the fact that the simulations are pure model predictions, obtained without any *a posteriori* parameter tuning.

Carbon ions (AG01522)				
$\boldsymbol{LET[keV/\mu m]}$	48.8	76.3	108	147.6
$\boldsymbol{\langle CL/(Gy \cdot cell)\rangle}$	5.1	6.1	7.2	8.6
$\boldsymbol{\langle CL/\mu m\rangle[10^{-3}]}$	63.2	117.9	198.1	323.9

Table 4.5: Average numbers of CL/(Gy·cell) and of CL/μm obtained from Equation 4.9 and used to reproduce AG survival curves by carbon ions of different LET.

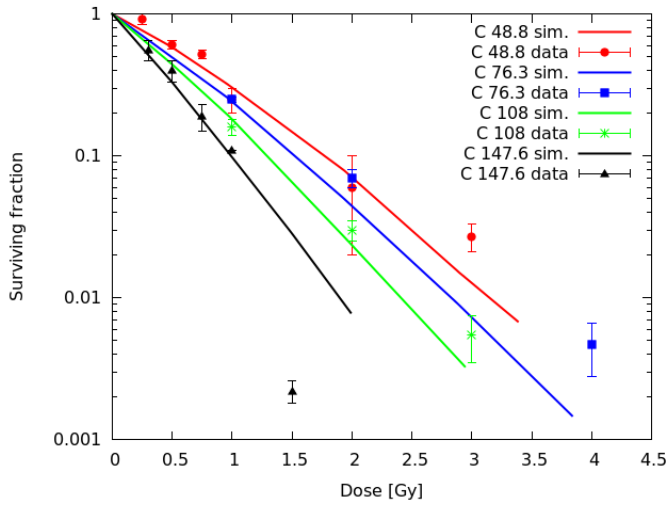

Figure 4.25: Pure model predictions, without any parameter tuning, compared with experimental survival curves for AG cells irradiated by carbon ions of different LET (48.8, 76.3, 108.0, 147.6 keV/μm). The lines are model simulations, whereas the points are experimental data.

The results presented in this Section are among the main outcomes obtained within this thesis. This study however is still at a preliminary stage: the lack of agreement for "high" LET proton survival curves needs to be further investigated, and the approach needs to be tested and extended to other particle types (such as alpha particles) and to other cell lines, in order to become more general. In any case this method can be considered as a first step towards a purely predictive model.

Conclusions and future perspectives

In this thesis work, cell death and chromosome damage (which are both important for hadrontherapy) by charged particles were investigated by the development and application of a biophysical model. The model, implemented in the form of a Monte-Carlo simulation code and called BIANCA, is based on few assumptions on the main mechanisms and is characterized by two adjustable parameters only. Providing simulated dose-response curves directly comparable with experimental data, BIANCA was used both to investigate some radiobiological open questions and for applications in the field of hadrontherapy.

In particular, after testing the model against experimental data, a study on the initially-induced DNA damage suggested that DNA cluster lesions at the kilobase-pair level may play a role in the subsequent induction of chromosome aberrations and cell death, in addition to damages at smaller scales, such as the so-called DSB^{++} (defined as at least two SSBs on each strand within 30 bp). Furthermore, an analysis of the biological effectiveness variation along a therapeutic proton beam as a function of depth and other physical factors supported the idea that the constant proton RBE currently applied in clinics may be sub-optimal. On the contrary, non-constant dose profiles may allow to better exploit the features of these particles, possibly reducing the damage to healthy tissues. An analogous study was performed on carbon ions, with results in line with what is currently applied in clinics.

In the last part of this work a formula was developed, linking the yields of DNA Cluster Lesions used as input parameters for a reference cell line with those used for other cell lines. More specifically, starting from the reproduction of a complete set of experimental data on hamster fibroblasts (taken as a reference) exposed to different radiation qualities, cell survival curves of human fibroblasts were predicted for proton and carbon ion irradiation in a wide energy range. This study is still preliminary and the approach tends to fail for the highest considered proton LET. However for the other curves the agreement with the experimental data was good and this method seems promising, show-

ing that the BIANCA approach can be applied not only to interpret already existing data, but also to perform predictions.

Concerning the possible future perspectives, a correction of the tendency of the model version BIANCA II to overestimate the effectiveness at very low survival levels for some radiation qualities is planned. A possible solution may consist of introducing a dependence on the LET for the f parameter, which represents the unrejoining probability for the initially-induced chromosome fragments. Furthermore we plan to extend the model to other cell lines, including tumor cells. Caution is needed in this latter case, also considering that tumor cells are often characterized by tetraploidy or other changes in the karyotype, which will require the implementation of an *ad hoc* cell nucleus model. Still in the framework of tumor therapy, the model may also be applied to simulate the induction of non-lethal, transmissible chromosome aberrations in normal cells surrounding the tumor region, since some of these aberration types (such as reciprocal translocations involving specific genes) are related to the induction of (second) tumors. As regards the predictive approach developed in the last part of this thesis, the method should be extended to other ion types (such as He-ions) and other cell lines. As a final step, to be of practical use, the model will be "coupled" to a Treatment Planning System and/or a radiation transport code. To this aim, a collaboration with the FLUKA group has already been established in the framework of the "MC-INFN/FLUKA" project funded by INFN.

List of Publications

Articles

1 - F. Ballarini, S. Altieri, S. Bortolussi, M. Carante, E. Giroletti and N. Protti, The BIANCA model/code of radiation-induced cell death: application to human cells exposed to different radiation types, *Radiat Environ Biophys*, 53:525-533 2014

2 - F. Ballarini, S. Altieri, S. Bortolussi, M. Carante, E. Giroletti and N. Protti, The role of DNA cluster damage and chromosome aberrations in radiation-induced cell killing: a theoretical approach, *Radiat Prot Dosim*, 166:75-79 2015

3 - M.P Carante and F. Ballarini, Modelling the induction of cell death and chromosome damage by therapeutic protons, *Proc. 14th Int. Conf. Nuclear Reaction Mechanisms, Varenna (Italy), June 15th – 19th, 2015, Edited by F. Cerutti, M. Chadwick, A. Ferrari, T. Kawano and P. Schoofs, CERN-Proceedings-2015-001, CERN, Geneva*, 6:361-368 2015

4 - M.P. Carante, S. Altieri, S. Bortolussi, I. Postuma, N. Protti and F. Ballarini, Modelling radiation-induced cell death: role of different levels of DNA damage clustering, *Radiat Environ Biophys*, 54:305–316 2015

5 - M.P. Carante, Modellizzazione di morte cellulare e aberrazioni cromosomiche indotte da protoni di diverso LET presso i Laboratori Nazionali del Sud, *Radiazioni - Ricerca e Applicazioni*, XVIII:4–7 2015

6 - L. Cansolino, A.M. Clerici, C. Zonta, P. Dionigi, G. Mazzini, R. Di Liberto, S. Altieri, F. Ballarini, S. Bortolussi, M.P. Carante, M. Ferrari, S.J. González, I. Postuma, N. Protti, G.A. Santa Cruz and C. Ferrari, Comparative study of the radiobiological effects induced on adherent vs suspended cells by BNCT, neutrons and gamma rays Treatments, *Applied Radiation and Isotopes*, 106:226–232 2015

7 - M.P Carante and F. Ballarini, Calculating Variations in Biological Effectiveness for a 62 MeV Proton Beam, *Front. Oncol.*, 6:76 2016

8 - F. Ballarini and M.P Carante, Chromosome aberrations and cell death by ionizing radiation: evolution of a biophysical model, *Radiation Physics and Chemistry*, In Press

9 - S. Bortolussi, N. Protti, M. Ferrari, I. Postuma, S. Fatemi, M. Prata, F. Ballarini, M.P. Carante, R. Farias, S.J. González, M. Marrale, S. Gallo, D. Nigg and S. Altieri, Experimental characterization of the thermal neutron irradiation facility at the TRIGA reactor of the University of Pavia, *Submitted to Physica Medica*

Abstracts

1 - N. Protti, F. Ballarini, S. Bortolussi, M.P. Carante, E. Giroletti, I. Postuma, G. Zanoni and S. Altieri, 106. Computational studies to evaluate the feasibility of Neutron Capture Therapy (NCT) to slow down the progression of Alzheimer's Disease (AD), *16th International Congress on Neutron Capture Therapy, Helsinki, Finland, Book of abstracts*, 2014

2 - L. Cansolino, A.M. Clerici, C. Zonta, C.M. Bianchi, P. Dionigi, G. Mazzini, R. Di Liberto, S. Altieri, F. Ballarini, S. Bortolussi, M.P.Carante, M. Ferrari, I. Postuma, N. Protti and Ferrari C., Comparative Study of the Radiobiological Effects Induced on Adherent vs Suspended Cells by BNCT, Neutrons and Gamma Rays Treatments, *16th International Congress on Neutron Capture Therapy, Helsinki, Finland, Book of abstracts*, 2014

3 - I. Postuma, S. Bortolussi, N. Protti, F. Ballarini, M.P. Carante, M. Ferrari and S. Altieri, Geant4 study of BNCT mixed field energy deposit in an approximated healthy tissue geometry, *6th International Congress on Neutron Capture Therapy, Helsinki, Finland, Book of abstracts*, 2014

4 - S. Bortolussi, I. Postuma, N. Protti, F. Ballarini, M. Carante, A. De Bari, P. Bruschi, C. Ferrari, L. Cansolino, C. Zonta, A.M. Clerici, L. Ciani, S. Ristori, L. Panza, S.J. González, O. Galasso, G. Gasparini and S. Altieri, Results of pre-clinical studies of BNCT for Osteosarcoma, *6th International Congress on Neutron Capture Therapy, Helsinki, Finland, Book of abstracts*, 2014

5 - F. Ballarini, M. Carante, A biophysical model linking DNA damage, chromosome aberrations and cell death, *NanoIBCT workshop MiND-IBCT, Austria, Book of abstracts*, 2014

6 - M. Carante and F. Ballarini, Un modello biofisico di morte cellulare basato sulle lesioni a cluster del DNA e le aberrazioni cromosomiche: implicazioni sui meccanismi e applicazioni nell'ambito dell'adroterapia, *Radiazioni – Ricerca e Applicazioni* , XVII-3 2014

7 - N. Protti, M. Ferrari, F. Ballarini, S. Bortolussi, M.P. Carante, A.De Bari, E. Giroletti, I. Postuma, S. Gallo, M. Marrale, A. Longo, S. Panzeca, G. Iacoviello and S. Altieri, Caratterizzazione dosimetrica della facility a neutroni termici del reattore TRIGA di Pavia: studio della dose da fotoni mediante rivelatori ESR, *Radiazioni – Ricerca e Applicazioni* , XVII-3 2014

8 - L. Cansolino, A.M. Clerici, P. Dionigi, G. Mazzini, R. Di Liberto, S. Altieri, F. Ballarini, S. Bortolussi, M.P. Carante, M. Ferrari, I. Postuma, N. Protti, and Ferrari C, Radiosensitivity differences of adherent vs suspended cell lines exposed to BNCT, Neutrons and Gamma Rays radiations114. Radiosensitivity differences of adherent vs suspended cell lines exposed to BNCT, Neutrons and Gamma Rays radiations, *Radiazioni – Ricerca e Applicazioni* , XVII-3 2014

9 - I. Postuma, S. Bortolussi, N. Protti, F. Ballarini, M.P. Carante, M. Ferrari and S. Altieri, Geant4 study of BNCT mixed field energy deposit in an approximated healthy tissue geometry, *Radiazioni – Ricerca e Applicazioni* , XVII-3 2014

10 - M. Carante and F. Ballarini, A biophysical model of cell death based on DNA cluster lesions and chromosome aberrations, *5th International Congress of Radiation Research, Kyoto, Japan*, 2015

11 - Testa A., Patrono C., Monteiro Gil O., Giesen U., Langner F., F. Ballarini, M. P. Carante, Palma V., M. Pinto and Rabus H., Alpha-particles microbeam irradiation: Analysis of radiation-induced chromosome damage on a cell-by-cell basis within the BIOQUART project, *5th International Congress of Radiation Research, Kyoto, Japan*, 2015

12 - A. Testa, C. Patrono, O. Monteiro-Gil, U. Giesen, F. Langner, F. Ballarini, M. P. Carante, V. Palma, M. Pinto, H. Rabus, Detection of chromosome aberrations and micronuclei in CHO cells after alpha-particle microbeam irradiation within the BioQuaRT project, *The 12th International Workshop on Microbeam Probes of Cellular Radiation Response, Tsuruga, Fukui, Japan*, 2015

13 - F. Ballarini and M. Carante, BIANCA, a model of radiation-induced cell death: biophysical mechanisms and possible applications for hadron therapy, *14th INTERNATIONAL CONFERENCE ON NUCLEAR REACTION MECHANISMS, Varenna (Italy)*, 2015

14 - M.P. Carante and F. Ballarini, Modeling chromosome aberrations and cell death by light ions: biophysical mechanisms and hadrontherapy applications, *61st Annual Meeting of the Radiation Research Society, Weston, Florida*, 2015

15 - M.P. Carante and F. Ballarini, Biological effectiveness calculations for an eye melanoma proton beam: a modeling approach, *55th Annual Conference of the Particle Therapy Co-operative Group, Prague, Czech Republic*, 2016

16 - M.P. Carante and F. Ballarini, Calculating variations in proton biological effectiveness by the BIANCA biophysical model, *42nd Conference of the European Radiation Research Society, Amsterdam, The Netherlands*, 2016

17 - F. Ballarini, M.P. Carante and L. Pederzoli, BIANCA, a biophysical model of radiation-induced cell death and chromosome damage, *42nd Conference of the European Radiation Research Society, Amsterdam, The Netherlands*, 2016

18 - F. Ballarini, M.P. Carante and L. Pederzoli, Particelle cariche e morte cellulare: a cosa servono i modelli biofisici?, *XVII Convegno Nazionale SIRR, Trento*, 2016

19 - M.P. Carante and F. Ballarini, Efficacia biologica di un fascio terapeutico di protoni: un approccio modellistico, *XVII Convegno Nazionale SIRR, Trento*, 2016

Bibliography

[1] A. Ottolenghi and F. Ballarini. Biophysics: ionizing radiation effects in biological materials. *In: Encyclopedia of Condensed Matter Physics, Edited by F. Bassani, J. Liedl and P. Wyder, published by Elsevier.*, 2005.

[2] W.D. Newhauser and R. Zhang. The physics of proton therapy. *Phys. Med. Biol*, 60:155–209, 2015.

[3] J.E. Turner. *Atoms, radiation, and radiation protection.* WILEY-VCH Verlag GmbH & Co. KGaA, 2008.

[4] W.R. Leo. *Technique for Nuclear and Particle Physics Experiments.* Springer-Verlag, 1994.

[5] N. Bohr. On the decrease of velocity of swiftly moving electrified particles in passing through matter. *Phil. Mag.*, 30:581–612, 1915.

[6] H. Bethe. Zur theorie des durchgangs schneller korpuskularstrahlen durch materie. *Ann. Phys.*, 5:324–400, 1930.

[7] F. Bloch. Zur bremsug rasch bewegter teilchen beim durchgang durch. *Ann. Phys.*, 16:285–320, 1933.

[8] S. Tavernier. *Experimental techniques for nuclear and particle physics.* Springer-Verlag, 2008.

[9] Chadwick et al. Nuclear data for neutron and proton radiotherapy and for radiation protection. ICRU report 63, 2000.

[10] H. Paganetti. *Proton Therapy Physics.* Series in Medical Physics and Biomedical Engineering. CRC Press Taylor and Francis Group, 2012.

[11] H. Paganetti. Nuclear interactions in proton therapy: dose and relative biological effect distributions originating from primary and secondary particles. *Phys. Medi. Biol.*, 47(5):747, 2002.

[12] S.M. Seltzer. An assessment of the role of charged secondaries from non-elastic nuclear interactions by therapy proton beams in water. NIST technical note NISTIR 5221, 1993.

[13] J. Soltani-Nabipour et al. Monte carlo investigation of light-ions fragmentation in water targets. *UPB Scientific Bulletin, Series A: Applied Mathematics and Physics*, 72(1), 2010.

[14] E. Haettner et al. Experimental study of nuclear fragmentation of 200 and 400 MeV/u ^{12}C ions in water for applications in particle therapy. *Phys. Med. Biol.*, 58(23):8265–8279, 2013.

[15] J. Hüfner. Heavy fragments produced in proton-nucleus and nucleus-nucleus collisions at relativistic energies. *Phys. Reports*, 125:129–185, 1985.

[16] E.M. Friedländer and H.H. Heckmann. Relativistic heavy-ion collisions experiment. In D.A (Ed.) Bromley, editor, *Treatise on Heavy-Ion Science*, chapter 4, pages 304–365. 1985.

[17] G. Kraft. Radiobiological effects of highly charged ions. In F. J. Currell Kluwer Academic Publisher, editor, *The Physics of Highly and Multiply Charged Ions*, chapter 10. 2002.

[18] Linear energy transfer. ICRU report 16, 1970.

[19] E.J. Hall and A.J. Giaccia. *Radiobiology for the Radiologist*. Lippincott Williams & Wilkins, 7 edition, 2012.

[20] D. Schardt, T. Elsässer, and D. Schulz-Ertner. Heavy-ion tumor therapy: Physical and radiobiological benefits. *Rev. Mod. Phys.*, 82(383):143–149, 2010.

[21] J. Kiefer and H. Straaten. A model of ion track structure based on classical collision dynamics. *Phys. Med. Biol.*, 31:1201–1209, 1986.

[22] M. Scholz. Effects of ion radiation on cells and tissues. *Adv. Polym. Sci.*, 62(383):96–155, 2003.

[23] N.E. Morton. Parameters of the human genome. *Proc. Natl. Acad. Sci.*, 88:7474–7476, 1991.

[24] R. D. Kornberg. Chromatin Structure: A Repeating Unit of Histones and DNA. *Science*, 184:868–871, 1974.

[25] A. Schipler and G. Iliakis. DNA double-strand-break complexity levels and their possible contributions to the probability for error-prone processing and repair pathway choice. *Nucleic Acids Res.*, 41(16):7589–7605, 2013.

[26] R.F. Martin and W.A. Haseltine. Range of radio chemical damage to DNA with decay of iodine-125. *Science*, 213(4510):869–898, 1981.

[27] H. Nikjoo, R.F. Martin, D.E. Charlton, M. Terrisol, P Kandayia, and P. Lobachevsky. Modelling of Auger induced DNA damage by incorporated ^{125}I. *Acta. Oncol.*, 35(7):849–856, 1981.

[28] W. Friedland, P. Jacob, H.G. Paretzke, and T. Stork. Monte Carlo simulation of production of short DNA fragments by low-linear energy transfer radiation using higher order DNA models. *Radiat. Res.*, 150(2):170–182, 1998.

[29] M. Jasin and N. Rothstein. Repair of strand breaks by homologous recombination. *Cold Spring Harb. Perspect. Biol.*, 5(11):a012740, 2013.

[30] J.K. Moore and J.E. Haber. Cell cycle and genetic requirements of two pathways of nonhomologous end-joining repair of double-strand breaks in Saccharomyces cerevisiae. *Mol. Cell. Biol.*, 16(5):2164–2173, 1996.

[31] A. Asaithamby and D.J. Chen. Cellular responses to DNA double-strand breaks after low-dose γ-irradiation. *Nucleic Acids Res.*, 37(12):3912–3923, 2009.

[32] H. Nikjoo, P. O'Neill, D. Goodhead, and M. Terrisol. Computational modelling of low-energy electron-induced DNA damage by early physical and chemical events. *Int. J. Radiat. Biol.*, 71(5):467–483, 1997.

[33] D.T. Goodhead. Initial events in the cellular effects of ionizing radiations: clustered damage in DNA. *Int. J. Radiat. Biol.*, 65(1):7–17, 1994.

[34] W.R. Holley and A. Chatterjee. Clusters of DNA damage induced by ionizing radiation: formation of short DNA fragments. 1. theoretical modeling. *Radiat. Res.*, 145:188–199, 1996.

[35] D. Alloni et al. A Monte Carlo study of the radiation quality dependence of DNA fragmentation spectra. *Radiat. Res.*, 173:263–271, 2010.

[36] L. Hlatky, R.K. Sachs, M. Vazquez, and M.N. Cornforth. Radiation-induced chromosome aberrations: insights gained from biophysical modeling. *BioEssays*, 24:714–723, 2002.

[37] J.A. Simmons, P. Cohn, and T. Min. Survival and yields of chromosome aberrations in hamster and human lung cells irradiated by alpha particle. *Radiat. Res.*, 145:174–180, 1996.

[38] T.H. Rabbits. Chromosomal translocations in human cancer. *Nature*, 372(6502):143–149, 1994.

[39] A.V. Carrano. Chromosome aberrations and radiation induced cell death I. trasmission and survival parameters of aberrations. *Mutat. Res.*, 17:341–353, 1973.

[40] M.N. Cornforth and J.S. Bedford. A quantitative comparison of potentially lethal damage repair and the rejoining of interphase chromosome breaks in low passage normal human fibroblasts. *Radiat. Res.*, 111:385–405, 1987.

[41] N.A. Dogget and W.H. McKenzie. An analysis of the distribution and dose response of chromosome aberrations in human lymphocytes after in vitro exposure to ^{137}Cesium gamma radiation. *Radiat. Environ. Biophys*, 22(1):33–51, 1983.

[42] D.L. Stevens, S. Bradley, D.T. Goodhead, and M.A. Hill. The influence of dose rate in the induction of chromosome aberrations and gene mutations following exposure of plateau phase V79-4 cells with high-LET alpha-particles. *Radiat. Res.*, 182(3):331–337, 2014.

[43] K. George, M. Durante, H. Wu, V. Willingham, and F.A Cucinotta. In vivo and in vitro measurements of complex-type chromosomal exchanges induced by heavy ions. *Advances in space research*, 31:1525–1535, 2003.

[44] N.S. Russel, C.F. Arlett, H. Bartelink, and A.C. Begg. Use of fluorescence *in situ* hybridization to determine the relationship between chromosome aberrations and cell survival in eight human fibroblast strains. *Int. J. Radiat. Biol.*, 68(2):185–196, 1995.

[45] P. Chaudary, T.I. Marshall, F.M. Perozziello, L. Manti, F.J. Currel, F. Hanton, F.J. McMahon, J.N. Kavanagh, G.A.P. Cirrone, F. Romano, K.M. Prise, and G. Schettino. Relative biological effectiveness variation along monoenergetic and modulated bragg peaks of a 62-MeV therapeutic proton beam: a preclinical assessment. *Int. J. Radiation Oncol. Biol. Phys.*, 90(1):27–35, 2014.

[46] M Belli, F. Cera, R. Cherubini, M. Dalla Vecchia, A.M.I. Haque, F. Ianzini, G. Moschini, O. Sapora, G. Simone, M.A. Tabocchini, and P. Tiveron. RBE-LET relationship for cell inactivation and mutation induced by low energy protons in V79 cells: further results in the LNL facility. *Int. J. Radiat. Biol.*, 74(4):501–509, 1998.

[47] W.K. Sinclair et al. Relative Biological Effectiveness (RBE), quality factor (Q) and radiation weighting factor (w_r). *ICRP Publication 92*, 33(4), 2003.

[48] T. Friedrich, U. Scholz, T. Elsässer, M. Durante, and M. Scholz. Systematic analysis of RBE and related quantities using a database of cell survival experiments with ion beam irradiation. *J. Radiat: Res.*, 54(3):494–514, 2012.

[49] B.S. Sørensen, J. Overgaard, and N. Bassler. In vitro RBE-LET dependence for multiple particle types. *Acta Oncol.*, 50(6):757–762, 2011.

[50] Nuclear physics for medicine. Nupecc report, 2014.

[51] L.E. Gerweck and S.V. Kozin. Relative biological effectiveness of proton beams in clinical therapy. *Radiother. Oncol.*, 50(2):135–142, 1999.

[52] D.E. Lea. *Actions of radiations on living cells.* Cambridge University Press, Cambridge, UK, 1946.

[53] S.H. Revel. Radiobiological effects of highly charged ions. pages 41–72. Columbia University Press, New York, NY, USA, 1963.

[54] S. Wolff and J. Bodycote. The induction of chromatid deletions in accord with breakage-and-reunion hypothesis. *Mutat. Res.*, 29:85–91, 1975.

[55] F. Ballarini. Chromosome damage by ionizing radiation: a review. *Il Nuovo Cimento*, 124(4):443–458, 2009.

[56] A.A. Edwards, V.V. Moiseenko, and H. Nikjoo. Modelling of DNA breaks and the formation of chromosome aberrations. *Int. J. Radiat. Biol.*, 66(5):633–637, 1994.

[57] G. Kreth, S.K. Pazhanisamy, M. Hausmann, and C. Cremer. Cell type-specific quantitative predictions of radiation-induced chromosome aberrations: A computer model approach. *Radiat. Res.*, 167(5):515–525, 2007.

[58] A.M. Chen, J.N Lucas, F.S. Hill, D.J. Brenner, and R.K. Sachs. Chromosome aberrations produced by ionizing radiation: Monte Carlo simulations and chromosome painting data. *CABIOS*, 11(4):389–397, 1995.

[59] A.M. Chen, J.N Lucas, F.S. Hill, D.J. Brenner, and R.K. Sachs. Proximity effects for chromosome aberrations measured by fish. *Int. J. Radiat. Biol.*, 69(4):411–420, 1996.

[60] R.K. Sachs, D. Levy, A.M. Chen, P.J. Simpson, M.N. Cornforth, E.A. Ingerman, P. Hahnfeldt, and L.R. Hlatky. Random breakage and reunion chromosome aberration formation model; an interaction-distance version based on chromatin geometry. *Int. J. Radiat. Biol.*, 76(12):1579–1588, 2000.

[61] D.E. Lea. *Actions of radiations on living cells.* Cambridge University Press, Cambridge, UK, 2nd edition, 1955.

[62] K.H. Chadwick and H.P. Leenhouts. A molecular theory of cell survival. *Phys. Med. Biol.*, 18(1):78–87, 1973.

[63] A.M. Kellerer and H.H. Rossi. A generalized formulation of dual radiation action. *Radiat. Res.*, 75(3):471–488, 1978.

[64] F. Ballarini. From DNA radiation damage to cell death: theoretical approaches. *J. Nucleic Acids*, 2010.

[65] M. Scholz and G. Kraft. Calculation of heavy ion inactivation probabilities based on track structure, x ray sensitivity and target size. *Radiat. Prot. Dosim.*, 52(1):29–33, 1994.

[66] T. Elsässer, M. Krämer, and M. Scholz. Accuracy of the Local Effect Model for the prediction of biologic effects of carbon ion beams *in vitro* and *in vivo*. *Int. J. Radiat. Oncol. Biol. Phys.*, 71(3):866–872, 2008.

[67] T. Elsässer et al. Quantification of the Relative Biologica Effectiveness for ion beam radiotherapy: direct experimental comparison of proton and carbon ion beams and a novel approach for treatment planning. *Int. J. Radiat. Oncol. Biol. Phys.*, 78(4):1177–1183, 2010.

[68] R. B. Hawkins. A statistical theory of cell killing by radiation of varying linear energy transfer. *Radiat. Res.*, 140:366–374, 1994.

[69] Y. Kase et al. Microdosimetric measurements and estimation of human cell survival for heavy-ion beams. *Radiat. Res.*, 166:629–638, 2006.

[70] T. Furusawa et al. Inactivation of aerobic and hypoxic cells from three different cell lines by accelerated He-, C- andNe-ion beams. *Radiat. Res.*, 154:485–496, 2000.

[71] T. Kanai et al. Examination of GyE system for HIMAC carbon therapy. *Int. J. Radiat. Oncol. Biol. Phys.*, 64:650–656, 2006.

[72] A. Carábe-Fernández, R.G. Dale, and B. Jones. The incorporation of the concept of minimum RBE (RBE_{min}) into the linear-quadratic model andthe potential for improved radiobiological analysis of high-LET treatments. *Int. J. Radiat. Biol.*, 83:27–39, 2007.

[73] A. Carábe-Fernández, M. Moteabbed, N. Depauw, J. Schuemann, and H. Paganetti. Range uncertainty in proton therapy due to variable biological effectiveness. *Phys. Med. Biol.*, 57:1159–1172, 2012.

[74] M. Wedemberg, B.K. Lind, and B. Hårdemark. A model for the relative biological effectiveness of protons: the tissue specific parameter α/β of photons is a predictor for the sensitivity to LET changes. *Acta Oncol.*, 52(3):580–588, 2013.

[75] A.L. McNamara, J. Schuemann, and H. Paganetti. A phenomenological relative biological effectiveness (RBE) model for proton therapy based on all published in vitro cell survival data. *Acta Oncol.*, 60(21):8399, 2015.

[76] M. Durante and Loeffler. Charged particles in radiation oncology. *J. S. Nat. Rev. Clin. Oncol.*, 7:37–43, 2010.

[77] E.J. Hall. Intensity-modulated radiation therapy, protons, and the risk of second cancers. *Int. J. Radiat. Oncol. Biol. Phys.*, 65(1):1–7, 2006.

[78] E. Fokas, G. Kraft, H. An, and R. Engenhart-Cabillic. Ion beam radiobiology and cancer: Time to update ourselves. *Biochim. Biophys. Acta*, 1796:216–229, 2009.

[79] R.R. Wilson. Radiological use of fast protons. *Radiology*, 47:487–491, 1946.

[80] C.A. Tobias et al. Radiological physics characteristics of the extracted heavy ion beams of the Bevatron. *Science*, 174:1131–1134, 1971.

[81] N.G. Burnet, S.J Thomas, K.E. Burton, and F.J. Jefferies. Defining the tumour and target volumes for radiotherapy. *Cancer Imaging*, 4(2):153–161, 2004.

[82] H. Bichsel and T. Hiraoka. Energy loss of 70 MeV protons in elements. *Nucl. Instrum. Methods*, 66(3):345–351, 1992.

[83] W.T. Chu, B.A. Ludewigt, and T.R. Renner. Instrumentation for treatment of cancer using proton and light-ion beams. *Rev. Sci. Instrum.*, 64(8):2055–2122, 1993.

[84] T. Akagi, A. Higashi, H. Tsugami, H. Sakamoto, Y. Masuda, and Y. Hishikawa. Ridge filter design for proton therapy at hyogo ion beam medical center. *Phys. Med. Biol.*, 48(22):301–312, 2003.

[85] T. Haberer, W. Becher, D. Schardt, and G. Kraft. Magnetic scanning system for heavy ion therapy. *Nucl. Instrum. Methods A*, 330(1):296–305, 1993.

[86] H. Brand et al. Therapy slow control system, data analysis and online monitoring. GSI Report, 1998.

[87] W.K. Weyrather. *Medical Applications of Accelerated Ions*, pages 469–490. Springer Berlin Heidelberg, Berlin, Heidelberg, 2004.

[88] Von G. Molière. Theorie der streuung schneller geladener teilchen ii mehrfach- und vielfachstreuung. *Z. Naturforschung*, 3a:78–97, 1948.

[89] U. Amaldi and G. Kraft. Radiotherapy with beams of carbon ions. *Reports on Progress in Physics*, 68(8):1861–1882, 2005.

[90] F. Tommasino, E. Scifoni, and M. Durante. New ions for therapy. *Int J Particle Ther*, 2(3):428–438, 2015.

[91] M. Jermann. Particle therapy statistics in 2014. *Int J Particle Ther*, 2(1):50–54, 2015.

[92] N.K. Abrosimov et al. 1000 mev proton beam therapy facility at petersburg nuclear physics institute synchrocyclotron. *Journal of Physics: Conference Series*, 41(1):424–432, 2006.

[93] http://www.ptcog.ch.

[94] D. Schulz-Ertner, O. Jäkel, and W. Schlegel. Radiation therapy with charged particles. *Semin. Radiat. Oncol.*, 16(4):249–59, 2006.

[95] M. Durante. New challenges in high-energy particle radiobiology. *Br. J. Radiol.*, 86, 2013.

[96] U. Linz et al. *Ion Beam Therapy*. Springer, 2012.

[97] M. Krämer, O. Jäkel, T. Haberer, G. Kraft, D. Schardt, and U. Weber. Treatment planning for heavy-ion radiotherapy: physical beam model and dose optimization. *Phys. Med. Biol.*, 45:3299–3317, 2000.

[98] A. Mairani et al. The fluka monte carlo code coupled with the local effect model for biological calculations in carbon ion therapy. *Phys. Med. Biol.*, 55:4273–4289, 2010.

[99] M. Scholz and G. Kraft. Track structure and the calculation of biological effects of heavy charged particles. *Adv. Space Res.*, 18:5–14, 1996.

[100] T. Inaniwa, T. Furukawa, S. Sato, and T. Kanai. Development of treatment planning for scanning irradiation at HIMAC. *Nucl. Instrum. Methods B*, 266(10):2194–2198, 2008.

[101] T. Inaniwa et al. Treatment planning for a scanned carbon beam with a modified microdosimetric kinetic model. *Phys. Med. Biol.*, 55:6721–6737, 2010.

[102] B.G. Wouters et al. Measurements of relative biological effectiveness of the 70 MeV proton beam at TRIUMF using V79 cells and the high precision cell sorter assay. *Radiat. Res.*, 146:159–170, 1996.

[103] H. Paganetti et al. Relative Biological Effectiveness (RBE) values for proton beam therapy. *J. Radiat. Oncol. Biol. Phys.*, 53:407–421, 2002.

[104] H. Paganetti and P. van Luijk. Biological considerations when comparing proton therapy and photon therapy. *Semin. Radiat. Oncol.*, 23:77–87, 2013.

[105] F. Guan, L. Bronk, U. Titt, S.H. Lin, D. Mirkovic, and M.D. Kerr. Spatial mapping of the biologic effectiveness of scanned particle beams: towards biologically optimized particle therapy. *Sci. Rep.*, 5:9850, 2015.

[106] G. Giovannini et al. Variable RBE in proton therapy: comparison of different model predictions and theirinfluence on clinical-like scenarios. *Radiat. Oncol.*, 11(1):68, 2016.

[107] S. Rosse. The National Centre for Oncological Hadrontherapy (CNAO): Status and perspectives. *Phys. Med.*, 31:333–351, 2015.

[108] U. Amaldi and S. Tosi. Per un centro di teleterapia con adroni. *TERA*, 91:1, 1991.

[109] S. Rossi. The status of CNAO. *Eur. Phys. J. Plus*, 126:78, 2011.

[110] U. Amaldi. History of hadrontherapy in the world and italian developments. *Rivista Medica*, 14(1):7–22, 2008.

[111] G. Cuttone et al. CATANA protontherapy facility: The state of art of clinical and dosimetric experience. *Eur. Phys. J. Plus*, 126(7):65, 2011.

[112] G. Cuttone et al. Use of 62 MeV proton beam for medical application at INFN-LNS: CATANA project. *Phys. Med.*, XVII:23–25, 2000.

[113] G.A.P. Cirrone et al. A 62-MeV proton beam for the treatment of ocular melanoma at Laboratori Nazionali del Sud-INFN. *IEEE TRANSACTIONS ON NUCLEAR SCIENCE*, 51(3):860–865, 2011.

[114] F. Ballarini, M. Merzagora, F. Monforti, M. Durante, G. Gialanella, G. Grossi, M. Pugliese, and A. Ottolenghi. Chromosome aberrations induced by light ions: Monte carlo simulations based on a mechanistic model. *Int. J. Radiat. Biol.*, 75:35–46, 1999.

[115] A. Ottolenghi, M. Merzagora, L. Tallone, M. Durante, H.G. Paretzke, and W.E. Wilson. The quality of DNA double-strand breaks: a Monte Carlo simulation of the end-structure of strand breaks produced by protons and alpha particles. *Radiat. Environ. Biophys.*, 34(4):239–244, 1995.

[116] A. Ottolenghi, F. Ballarini, and M. Biaggi. Modelling chromosomal aberration induction by ionising radiation: the influence of interphase chromosome architecture. *Adv. Space Res.*, 27:369–382, 2001.

[117] F. Ballarini, M. Biaggi, and A. Ottolenghi. Nuclear architecture and radiation-induced chromosome aberrations: models and simulations. *Radiat. Prot. Dosim.*, 99:175–182, 2002.

[118] F. Ballarini and A. Ottolenghi. Chromosome aberrations as biomarkers of radiation exposure: modelling basic mechanisms. *Adv. Space Res.*, 31:1557–1568, 2003.

[119] A.A. Edwards, D.C. Lloyd, J.S. Prosser, P. Finnon, and J.E. Moquet. Chromosome aberrations induced in human lymphocytes by 8.7 MeV protons and 23.5 MeV helium-3 ions. *Int. J. Radiat. Biol.*, 50(1):137–145, 1986.

[120] R.J. Purrott, A.A. Edwards, D.C. Lloyd, and J.W. Stather. The induction of chromosome aberrations in human lymphocytes by in vitro irradiation with α-particles from plutonium-239. *Int. J. Radiat. Biol.*, 38(3):277–284, 1980.

[121] F. Ballarini and A. Ottolenghi. A model of chromosome aberration induction and CML incidence at low doses. *Radiat. Environ. Biophys.*, 43:165–171, 2004.

[122] F. Ballarini and A. Ottolenghi. A model of chromosome aberration induction: applications to space research. *Radiat. Res.*, 164:567–570, 2005.

[123] F. Ballarini, D. Alloni, A. Facoetti, A. Mairani, R. Nano, and A. Ottolenghi. Radiation risk estimation: modelling approaches for "targeted" and "non-targeted" effects. *Adv. Space Res.*, 40:1392–1400, 2007.

[124] F. Ballarini and A Ottolenghi. Heavy-ion effects: from track structure to dna and chromosome damage. *New. J. Phys.*, 10:075008, 2008.

[125] K. George, M. Durante, V. Willingham, H. Wu, T. Yang, and F.A. Cucinotta. Biological effectiveness of accelerated particles for the induction of chromosome damage measured in metaphase and interphase human lymphocytes. *Radiat. Res.*, 160:425–435, 2003.

[126] F. Ballarini and M.P. Carante. Chromosome aberrations and cell death by ionizing radiation: Evolution of a biophysical model. *Radiat. Phys. Chem.*, http://dx.doi.org/10.1016/j.radphyschem.2016.06.009i, 2016.

[127] R. Zirbel, U.R. Mathieu, A. Kurz, T. Cremer, and P. Lichter. Evidence for a nuclear compartment of transcription and splicing located at chromosome domain boundaries. *Chromosome Res.*, 1:93–106, 1993.

[128] T. Neumaier, J. Swenson, C. Pham, A. Polyzos, A.T. Lo, P-A. Yang, J. Dyball, A. Asaithamby, D.J. Chen, S. Thalhammer, M.J. Bissell, and Costes S.V. Evidence for formation of dna repair centres and dose response nonlinearity in human cells. *PNAS*, 109:443–448, 2012.

[129] F. Ballarini, S. Altieri, S. Bortolussi, M. Carante, E. Giroletti, and N. Protti. The BIANCA model/code of radiation-induced cell death: application to human cells exposed to different radiation types. *Radiat. Environ. Biophys.*, 53(3):525–533, 2014.

[130] A. Chatterjee and H.J. Schaefer. Microdosimetric structure of heavy ion tracks in tissue. *Radiat. Environ. Biophys.*, 13(3):215–227, 1976.

[131] D. Bettega, P. Calzolari, S.M. Doglia, B. Dulio, L. Tallone, and A.M. Villa. Technical report: cell thickness measurements by confocal fluorescence microscopy on C3H10T1/2 and V79 cells. *Int J Radiat Biol*, 74(3):397–403, 1998.

[132] S. Carpenter, M.N. Cornforth, W.F. Harvey, M.R. Raju, M.E. Schillaci, M.E. Wilder, and D.T. Goodhead. Radiobiology of ultrasoft X rays IV. Flat and round-shaped Hamster Cells (CHO-1oB, HS-23). *Radiat Res*, 119(3):523–533, 1989.

[133] C.K. Hill, B.E. Nelms, J.F. MacKay, D.W. Pearson, W.S. Kennan, T. Rock Mackie, P.M.Jr DeLuca, M.J. Lindstrom, and M.N. Gould. Synchrotron-produced ultrasoft X rays: equivalent cell survival at the isoattenuating energies 273 eV and 860 eV. *Radiat Res*, 150(5):513–520, 1998.

[134] F. Ballarini, S. Altieri, S. Bortolussi, E. Giroletti, and N. Protti. A model of radiation-induced cell killing: insights into mechanismsand applications for hadron therapy. *Radiat Res*, 180(3):307–315, 2013.

[135] A. Bolzer, G. Kreth, I. Solovei, D. Koehler, K. Saracoglu, C. Fauth, S. Muller, R. Eils, C. Cremer, M.R. Speicher, and T. Cremer. Three-dimensional maps of all chromosomes in human male fibroblast nuclei and prometaphase rosettes. *PLoS. Biol.*, 3(5):e157, 2005.

[136] M.N. Cornforth, S.M. Bailey, and E.H. Goodwin. Dose responses for chromosome aberrations produced in noncycling primary human fibroblasts by alpha particles, and by gamma rays delivered at sublimiting low dose rates. *Radiat. Res.*, 158(1):43–53, 2002.

[137] N. Hamada, T. Funayama, S. Wada, T. Sakashita, T. Kakizaki, M. Ni, and Y. Kobayashi. LET-dependent survival of irradiated normal human fibroblasts and their descendents. *Radiat. Res.*, 166(1):24–30, 2006.

[138] P. Neti, S.M. de Toledo, V. Perumal, E.I. Azzam, and R.W. Howell. A multi-port low-fluence alpha-particle irradiator: fabrication, testing and benchmark radiobiology studies. *Radiat. Res.*, 161(6):732–738, 2004.

[139] H. Nikjoo, P. O'Neill, M. Terrissol, and D.T. Goodhead. Quantitative modelling of DNA damage using Monte Carlo track structure method. *Radiat. Environ. Biophys.*, 38(1):31–38, 1999.

[140] A.M. Chen, J.N. Lucas, P.J. Simpson, C.S. Griffin, J.R.K. Savage, D.J. Brenner, L.R. Hlatky, and R.K. Sachs. Computer simulation of data on chromosome aberrations produced by x rays or alpha particles and detected by fluorescence in situ hybridization. *Radiat. Res.*, 148(5 Suppl.):S93–S101, 1997.

[141] M.P. Carante, S. Altieri, S. Bortolussi, I. Postuma, N. Protti, and F. Ballarini. Modeling radiation-induced cell death: role of different levels of DNA damage clustering. *Radiat. Environ. Biophys.*, 54(3):305–316, 2015.

[142] M. Folkard, K.M. Prise, B. Vojnovic, H.C. Newman, M.J. Roper, and B.D. Michael. Inactivation of V79 cells by low-energy protons, deuterons and helium-3 ions. *Int. J. Radiat. Biol.*, 69(6):729–738, 1996.

[143] R. Cox, J. Thacker, and D.T. Goodhead. Inactivation and mutation of cultured mammalian cells by aluminium characteristics ultrasoft X-rays II. Dose–response of Chinese hamster and human diploid cells to aluminium X-rays and radiations of different LET. *Int. J. Radiat. Biol.*, 31(6):561–576, 1977.

[144] J. Thacker, A. Stretch, and M.A. Stephens. Mutation and inactivation of cultured mammalian cells exposed to beams of accelerated heavy ions II. chinese hamster V79 cells. *Int. J. Radiat. Biol.*, 36(2):137–148, 1979.

[145] B. Phoenix, S. Green, M. Hill, B. Jones, A. Mill, and D. Stevens. Do the various radiations present in BNCT act synergistically? cell survival experiments in mixed alpha-particle and gamma-ray fields. *Appl. Radiat. Isotopes*, 67(7-8 Suppl):S318–S320, 2009.

[146] J.N. Kavanagh, F.J. Currell, D.J. Timson, K.I. Savage, D.J. Richard, S.J. McMahon, O. Hartley, G.A.P. Cirrone, F. Romano, K.M. Prise, N. Bassler, M.H. Holzscheiter, and G. Schettino. Antiproton induced DNA damage: proton like in flight, carbon-ion like near rest. *Sci. Rep.*, 3:1770, 2013.

[147] K. Tsuboi, TC. Yang, and D.J. Chen. Charged particle mutagenesis I. Cytotoxic and mutagenic effects of high-LET charged iron particles on human skin fibroblasts. *Radiat. Res.*, 129(2):171–176, 1992.

[148] J.M. Bridger, H. Herrmann, C. Muenkel, and P. Lichter. Identification of an interchromosomal compartment by polymerisation of nuclear-targeted vimentin. *J. Cell Sci.*, 111:1241–1253, 1998.

[149] H. Wu, K. George, and T.C. Yang. Estimate of the frequency of true incomplete exchanges in human lymphocytes exposed to 1 GeV/u Fe ions in vitro. *Int. J. Radiat. Biol.*, 75(5):593–599, 1999.

[150] H. Wu, Y. Furusawa, K. George, T. Kawata, and F.A. Cucinotta. Analysis of unrejoined chromosomal breakage in human fibroblast cells exposed to low- and high-LET radiation. *J. Radiat. Res.*, 43:S181–S185, 2002.

[151] J.J. Boei, S. Vermeulen, L.H. Mullenders, and A.T. Natarajan. Impact of radiation quality on the spectrum of induced chromosome exchange aberrations. *Int. J. Radiat. Biol.*, 77(8):847–857, 2001.

[152] M.N. Cornforth and J.S. Bedford. On the nature of a defect in cells from individuals with ataxia-telangiectasia. *Science*, 227(4694):1589–91, 1985.

[153] M. Carante and F. Ballarini. Calculating variations in biological effectiveness for a 62 MeV proton beam. *Front. Oncol.*, 6:76, 2016.

[154] G.I. Terzoudi, V.I. Hatzi, C. Donta-Bakoyianni, and G.E. Pantelias. Chromatin dynamics during cell cycle mediate conversion of DNA damage into chromatid breaks and affect formation of chromosomal aberrations: Biological and clinical significance. *Mutation Research/Fundamental and Molecular Mechanisms of Mutagenesis*, 711(1–2):174 – 186, 2011.

[155] D.T. Goodhead and H. Nikjoo. Track structure analysis of ultrasoft x-rays compared to high- and low-let radiations. *International Journal of Radiation Biology*, 55(4):513–529, 1989.

[156] D.E. Charlton, H. Nikjoo, and J.L. Humm. Calculation of initial yields of single- and double-strand breaks in cell nuclei from electrons, protons and alpha particles. *International Journal of Radiation Biology*, 56(1):1–19, 1989.

[157] A. Chatterjee and W.R. Holley. Biochemical mechanisms and clusters of damage for high-let radiation. *Advances in Space Research*, 12(2):33 – 43, 1992.

[158] H. Nikjoo, P. O'Neill, W.E. Wilson, and D.T. Goodhead. Computational approach for determining the spectrum of dna damage induced by ionizing radiation. *Radiat. Res.*, 156:577–583, 2001.

[159] W. Friedland, M. Dingfelder, P. Kundrát, and P. Jacob. Track structures, DNA targets and radiation effects in the biophysical Monte Carlo simulation code PARTRAC. *Mutation Research/Fundamental and Molecular Mechanisms of Mutagenesis*, 711(1–2):28 – 40, 2011.

[160] H. Wang, X. Zhang, P. Wang, X. Yu, J. Essers, D. Chen, R. Kanaar, S. Takeda, and Y. Wang. Characteristics of dna-binding proteins determine the biological sensitivity to high-linear energy transfer radiation. *Nucleic Acids Research*, 38(10):3245–3251, 2010.

[161] Björn Rydberg. Clusters of dna damage induced by ionizing radiation: Formation of short dna fragments. ii. experimental detection. *Radiation Research*, 145(2):200–209, 1996.

[162] Björn Rydberg, William R Holley, I.Saira Mian, and Aloke Chatterjee. Chromatin conformation in living cells: support for a zig-zag model of the 30 nm chromatin fiber1. *Journal of Molecular Biology*, 284(1):71 – 84, 1998.

[163] B. Rydberg, L. Heilbronn, W.R. Holley, M. Lbrich, C. Zeitlin, A. Chatterjee, and P. K. Cooper. Spatial distribution and yield of DNA Double-Strand Breaks induced by 3–7 MeV helium ions in human fibroblasts. *Radiat. Res.*, 158:32–42, 2002.

[164] P.J. Johnston and P.E. Bryant. A component of dna double-strand break repair is dependent on the spatial orientation of the lesions within the higher-order structures of chromatin. *International Journal of Radiation Biology*, 66(5):531–536, 1994.

[165] P. E. Bryant P. J. Johnston, P. L. Olive. Higher-order chromatin structure-dependent repair of dna double-strand breaks: Modeling the elution of dna from nucleoids. *Radiation Research*, 148(6):561–567, 1997.

[166] A.L. Ponomarev and F.A. Cucinotta. Chromatin loops are responsible for higher counts of small dna fragments induced by high-let radiation, while chromosomal domains do not affect the fragment sizes. *International Journal of Radiation Biology*, 82(4):293–305, 2006.

[167] W. Friedland, P. Jacob, H.G. Paretzke, A. Ottolenghi, F. Ballarini, and M. Liotta. Simulation of light ion induced dna damage patterns. *Radiation Protection Dosimetry*, 122(1-4):116–120, 2006.

[168] J. Carlsson B. Stenerlow E. Hoglund, E. Blomquist. Dna damage induced by radiation of different linear energy transfer: initial fragmentation. *International Journal of Radiation Biology*, 76(4):539–547, 2000.

[169] F. Antonelli, M. Belli, A. Campa, A. Chatterjee, V. Dini, G. Esposito, B. Rydberg, G. Simone, and M.A. Tabocchini. {DNA} fragmentation induced by fe ions in human cells: shielding influence on spatially correlated damage. *Advances in Space Research*, 34(6):1353 – 1357, 2004.

[170] P.K. Cooper M. Lobrich and B. Rydberg. Non-random distribution of dna double-strand breaks induced by particle irradiation. *International Journal of Radiation Biology*, 70(5):493–503, 1996.

[171] J.H. Chang, N.K. Lee, J.Y. Kim, Y. Kim, S.H. Moon, T.H. Kim, J. Kim, D.Y. Kim, K.H. Cho, and K.H. Shin. Phase II trial of proton beam accelerated partial breast irradiation in breast cancer. *Radiotherapy and Oncology*, 108(2):209–214, 2013.

[172] M. Belli et al. Effectiveness of monoenergetic and spread-out bragg peak carbon-ions for inactivation of various normal and tumour human cell lines. *Journal of radiation research*, 49(6):597–607, 2008.

[173] M. Carante. Modellizzazione di morte cellulare e aberrazioni cromosomiche indotte da protoni di diverso LET presso i Laboratori Nazionali del Sud. *Radiazioni - Ricerca e Applicazioni*, XVIII(1-2):4–7, 2015.

[174] K. Greif, H.J. Brede, D. Frankenberg, and U. Giesen. The PTB single ion microbeam for irradiation of living cells. *Nucl. Instrum. Meth. B*, 217(3):505–512, 2004.

[175] K Greif, W. Beverung, F. Langner, D. Frankenberg, A. Gellhaus, and F. Banaz-Yasar. The ptb microbeam: a versatile instrument for radiobiological research. *Radiat. Prot. Dosimetry*, 122(1-4):313–315, 2006.

[176] C. Patrono, Gil. Monteiro, U. Giesen, F. Langner, M. Pinto, H. Rabus, and A. Testa. 'BioQuaRT' project: design of a novel in situ protocol for the simultaneous visualisation of chromosomal aberrations and micronuclei after irradiation at microbeam facilities. *Radiat. Prot. Dosimetry*, 166(1-4):197–199, 2015.

[177] H. Nagasawa and J.B. Little. Bystander effect for chromosomal aberrations induced in wild-type and repair deficient CHO cells by low fluences of alpha particles. *Mutat. Res.*, 508:121–129, 2002.

[178] A.A. Edwards, D.C. Lloyd, and R.J. Purrott. Radiation induced chromosome aberrations and the Poisson distribution. *Rad. and Environm. Biophys.*, 16:89–100, 1979.

[179] E. Gudowska-Nowak, R. Lee, E. Nasonova, S. Ritter, and M. Scholz. Effect of LET and track structure on the statistical distribution of chromosome aberrations. *Advances in Space Research*, 39:1070–1075, 2007.

[180] C.M.S. Lee and F. Famoye. A comparison of generalized Poisson distribution for modeling chromosome aberrations. *Biom. J.*, 2:299–313, 1996.

[181] R.P. Virsik and D. Harder. Statistical interpretation of the overdispersed distribution of radiation-induced dicentric chromosome aberrations at high LET. *Radiat. Res.*, 85:13–23, 1981.

[182] E.A. Ainsbury, A.V. Volodymyr, N.A. Maznyk, and D.C. Lloyd. A comparison of six statistical distributions for analysis of chromosome aberration data for radiation biodosimetry. *Radiat. Prot. Dosim.*, 155(3):253–267, 2013.

Ringraziamenti

This project was partially supported by the Italian Institute of Nuclear Physics (INFN), ETHICS project (pre-clinical Experimental and THeoretical studies to Improve treatment and protection by Charged particleS).

I would like to thank Dr. Kevin Prise and Dr. Marco Durante, who were the referees of my thesis, for their helpfull comments.

Il ringraziamento più grande è senza dubbio per Francesca, che è stata molto più di una *supervisor* e di una guida scientifica, dimostrandomi affetto, fiducia e un'umanità rara in un ambiente di lavoro.

Voglio ringraziare anche tutto il resto del "gruppo": Cla, Sil, Ale, Andre, che mi hanno accolto fin dall'inizio, Nico, con cui condivido bei ricordi, e Alessia, compagna di lavoro, di viaggi, di scherzi.

Un grazie ai miei genitori: a mio padre, prima e dopo, e a mia madre, che mi ha insegnato che si può affrontare la vita con dignità e coraggio, e mi ha mostrato la strada. Grazie a mio fratello, che è stato un padre, un amico, una guida, un punto di riferimento per praticamente qualsiasi cosa. Ringrazio i miei nonni, perché erano fieri di me anche senza bisogno di vedere questo mio risultato. Grazie ai miei zii e mia cugina, a cui voglio bene, e a tutto il resto di questa famiglia matta. Grazie a una ragazza forte e a un uomo buono, che non ci sono più.

Agli amici di sempre: Ale, Anto, Didi, Always, Robi, Michi, Ste. Grazie in particolare a Giagio, *I still love you*, a Grego, compagno di banco e inspiegabile 9 in condotta, a Dibo, Leader gobbo dai grandi ideali, a Anna, con cui dopo tanti anni posso ancora parlare di tutto, e a Teo, che mi ha dimostrato che quando cado è pronto a raccogliermi. Grazie ad Andre e a Giulia, che so sempre dove posso trovare (alla F, per la precisione). Grazie a Giulio, perché una parte della mia infanzia ha la sua forma, a Giugia, per un abbraccio che ancora non dimentico, a Luca, a Ila, a Luca S, a Giulia mora, che a 18 anni mi ha dato un insegnamento maestoso, a Christian, Giovanni, Pino, Pil e in generale a tutte le altre persone importanti che hanno preso una strada diversa dalla mia. A Richard, perché so che ci perderemo mille volte, ma spero che ci ritroveremo sempre. Grazie a Thomas, Dado, Rodi, Mauri, a Irene e Carla, che sono due begli esempi di donne, e a tutti quelli del Borgo, per le centinaia

di serate insieme.

Un ringraziamento speciale va alle persone che mi hanno accompagnato in questi anni di dottorato: a Ian, per quei 18 giorni di fila e molti altri, e a Seta, che stimo, che mi assomiglia, che mi ha permesso di vedere la fragilità dietro la sua corazza (siete il mio "dark side of the bottle"). E poi a Barbara, per quell'affinità iniziale, a Angi, meravigliosa compagna di "plateau", di bananeti e di scrivanie, a Sam, perché è una persona molto poco orribile (discorsetto?) e a Linda, che in poco tempo mi ha regalato tante cose, dalle rime ai pianti, senza smettere mai di stupirmi. A tutti voi ho solo una domanda da fare: macchinette? Grazie, ovviamente, a Planck!

E grazie infine, nonostante tutto, ad Alice, perché davvero senza di lei non sarei qui e perché il nostro, finché è durato, è stato un amore dolcissimo.